Exploring Two-dimensional Superatomic Semiconductors

Xinjue Zhong

Submitted in partial fulfillment of the

requirements for the degree of

Doctor of Philosophy

in the Graduate School of Arts and Sciences

COLUMBIA UNIVERSITY

2019

ABSTRACT

Exploring Two-dimensional Superatomic Semiconductors

Xinjue Zhong

Two-dimensional (2D) van der Waals materials have received widespread attention due to their novel 2D properties that are distinct from their bulk counterparts. These unique properties offer new possibilities for fundamental research and for diverse applications in electronics, optoelectronics, and valleytronics. It is therefore of great interest to design 2D materials from complex, hierarchical and/or tunable building blocks. Atomic and molecular clusters are attractive target due to their atomic precision, structural and compositional diversity and synthetic flexibility. In this thesis, we report two novel quasi-2D superatomic semiconductors: $Re_6Se_8Cl_2$ and $Mo_6S_3Br_6$, whose building blocks are atomic clusters rather than simple atoms. In Chapter 3, we determine the electronic bandgap (1.58 eV), optical bandgap (indirect, 1.48 eV), and exciton binding energy (100 meV) of $Re_6Se_8Cl_2$ crystals by using scanning tunneling spectroscopy, photoluminescence and ultraviolet photoelectron spectroscopy, and first principles calculations. The exciton binding energy is consistent with the partially 2D nature of the exciton. In Chapter 4, the layered van der Waals material $Mo_6S_3Br_6$ possesses a robust 2D character with a direct gap of 1.64 eV, as determined by scanning tunneling spectroscopy. By using polarization dependent Raman spectroscopy and DFT calculations, we determine its strong in-plane electronic anisotropy. The complex, hierarchical structures with 2D characters of these two materials thus suggest an effective strategy to expand the design space for 2D materials research with multi-functionality and novel physical properties.

Table of Contents

List of Figures

Lists of Tables

Acknowledgements

First, I want to thank my advisor Xiaoyang Zhu. He is a very caring, though sometimes strict, mentor, always willing to have scientific discussions and offer guidance on my research. The most precious thing I found is his enthusiasm toward science and his genuine heart to know the nature, which inspired me a lot when I experienced countless experimental failure and questioned myself if it is a right decision to continue my phD studies. Thanks God that I didn't quit and I know I could not make it without his continuous guidance and encouragement 'Try it one more time'.

I also want to give thanks to Prof. Abhay Narayan Pasupathy, who is like my co-advisor. I would run to him when the STM setup had any problems (which often happens). In addition to the hand-on help on the experimental techniques and advice on scientific research, his patience and optimistic attitude inspired me a lot, especially when things didn't work out. Moreover, I'd like to thank Prof. George W. Flynn who assigned the whole lab to Xiaoyang before retirement and gave me the chance to start the unexpected journey with STM. Although we only overlapped for one year, I really enjoyed the sweet group meetings with prepared breakfast.

Meanwhile, I feel so lucky to have people in Zhu group and Pasupathy group as my group mates and collaborators for the past five years, who provides me a friendly environment. Thanks to working alongside Dr. Tyler Evans (we joined the group together), Prakriti Joshi, Jue Wang, Drew Schlaus, Michael Spencer, Felisa Conrad-Burton, Kameron Hansen, Dr. Feifan Wang, Dr. Yusong Bai, Dr. Mark Ziffer, Dr. Sebastian F. Maehrlein, Dr. Daniel Niesner, M. Tuan Trinh, Haiming Zhu, Xiaoxi Wu and Drew Edelberg, Alexander Kerelsky, Minghao Chen. Special thanks to Dr.

Amir Zabet and Dr. Kwang Taeg Rim, who led me into the STM world and tutor me on every detail of STM setups; to Dr. Christopher Gutiérrez, who shared strategies of experimental operations and provided me practical suggestions on my future career; to Kihong Lee, with whom I collaborated on my main projects and has done all optical measurements including photoluminescence and Raman spectroscopy; to Timothy L Atallah, who always gives me encouragement as a friend and pray for me as a brother in Christ; finally to Fang Liu, who is always willing to offer help and guidance when I encounter difficulties on 2PPE experiments and generously feeds our group with her homemade sweets.

In my time at Columbia, I am so impressed on and benefited from the active collaborations among groups within Chemistry Department and beyond that. As an experimental chemical physicist, my work can't continue without my collaborators in chemical synthesis and in theoretical calculations. Thanks to Prof. Colin Nuckolls, who led me into the world of superatomic solids.Thanks to Prof Xavier Roy and his student Bonnie Choi, who provided me single crystal samples when I was struggling with solution-based molecules. I'm so grateful to have Bonnie as my collaborator, who kept improving the quality and size of these samples and always gave me the biggest ones. Thanks to Prof. Guangbin Dong and his postdoc Gang Li at University of Chicago, who introduced me the rich family of graphene nanoribbons. Although the STM work didn't work well, I'm still very grateful for sending me various samples with modified structures to improve the imaging processes. 'Sample is everything', without them, this thesis would not exist. Besides, I want to give thanks to Prof. Filippo De Angelis and his postdoc Daniele Meggiolaro at Computational Laboratory for Hybrid/Organic Photovoltaics (CLHYO) in Italy, who have done excellent work on the DFT calculations and provide us theoretical deep insights.

Besides the struggling but wonderful experiences in science, my life in New York city is so much

enriched by my Bible study group and my Church. Joining the bible study every Friday becomes part of my life since the begining of my first semester at Columbia. I'm deeply thakeful for the life-long friendship I gained here and all the sweet moments we shared and most importantly the Word we seek together. I love this city because of the people in it.

Lastly, I want to give my genuine thanks to my boyfriend Samuel Yin, my lovely parents and my heavenly Father. Samuel, although he knows little about what I'm doing, he always gives me comfort and encouragement. I'm so thankful to have him as a life-long partner, with whom I can share the joyful and difficult moments. My lovely parents, although they are far away from me, they always give me love and support. They are the ones who accept me with no conditions. I really cherich the time they came to U.S. to visit me for half a year. We had never lived together for such a long time since my primary school. My heavenly Father, who loves me so deeply even before I knew Him. He changes my life and fills me with a new heart and a new spirit. I'm so grateful for what He gives me and allows me to experience, either the high mountains or the low valleys. ' In His light we see light'.

Xinjue Zhong

New York City, New York

Chapter 1

Introduction

Two-dimensional materials are materials consisting of single or few layers of atoms. The family of two-dimensional (2D) materials [1] has grown extensively including the semi-metal graphene [2,3], semiconducting transition metal dichalcogenides (TMDCs) [4–6] and insulating hexagonal boron nitride (h-BN) [7,8]. Such materials have received widespread attention due to their novel 2D properties that are distinct from their bulk counterparts. Due to poor dielectric screening in the 2D geometry and quantum confinement, electronic excitations in these materials are excitonic in nature [9–12]. Systems with inversion symmetry broken and spin-orbit coupling, such as monolayer MoS2, exhibit strong spin-valley coupling and valley-/spin-dependent properties [13,14]. A number of other extraordinary physical phenomena have been discovered in 2D materials, such as intrinsic layer-dependent ferromagnetism [15], topological insulating phase with conducting edge states [16,17] and quantum metal state induced from 2D superconductors [18]. These unique properties offer new possibilities for fundamental research and for diverse applications in electronics, optoelectronics, and valleytronics [14,19–21]. Moreover, atomic thickness of 2D materials offers great flexibility to tune these properties by strain, doping, and external electric or magnetic fields as compared to the bulk. For example, the high endurance of strain in monolayer TMDCs allows us to tune the electronic bandgap from direct to indirect when

applying ~ 1% strain [22] and even down to zero (metallic behaviors) with large biaxial strain of ~ 10 % [23] before breaking. It makes strain engineering a viable approach for the fabrications of devices with tunable characteristics. Furthermore, these 2D sheets can be easily integrated by vertical stacking to design systems (homo- or hetero-structures) for low-dimensional physics study and quantum materials with desired functionalities. The rotation angle between layers provides another degree of freedom to tune the properties that is strikingly different from the natural counterparts, as demonstrated in bilayer graphene featuring superconductivity at a 'magic' angle of 1.1º [24,25]. The heterostructures in combination of two different layers offers great opportunities to study and engineer the interlayer excitons, which is longing for a long time in history [26,27].

To achieve these atomically thin layers, both top-down exfoliation [3] and bottom-up synthesis [28] have been rapidly developed in the past few years. In addition to the naturally existing materials, synthetic 2D sheets without bulk analogues [29,30] such as silicene, germanene have been explored as well. However, nearly all 2D materials that have been fabricated to date are atomic solids with relatively simple crystal structures. For example, graphene and h-BN consist of

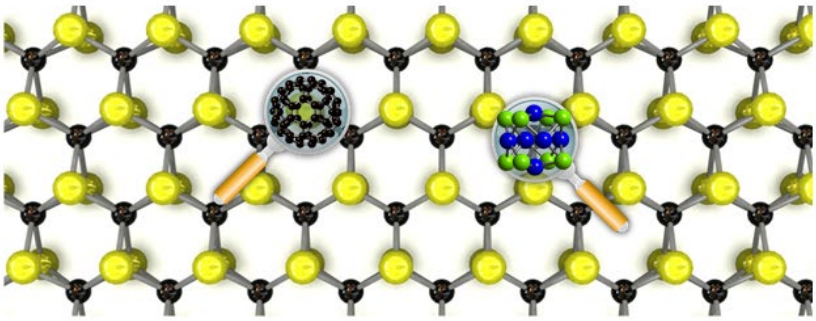

Figure 1.1 Schematic of building 2D materials with molecular clusters. Structure of monolayer TMDCs (MX_2, M = Mo,W, X = S, Se) with atomic building blocks. Color code: M, black; X, yellow. Replacing atomic building blocks with complex clusters opens a door in designing 2D materials with complex, hierarchical and/or tunable structures.

a single layer of atoms, and TMDCs are composed of a monolayer of transition metal atom sandwiched between two insulating layers of chalcogen atoms. Beyond these atomic solids, there is a growing interest in designing 2D materials with complex, hierarchical and/or tunable structures. Nanoparticles, for instant, have been extensively studied as nanoparticle building blocks to form 2D superlattices [31–34]. However, these materials are intrinsically lack of atomic precision. In this context, atomic and molecular clusters are attractive targets as zero-dimensional building blocks due to their atomic precision, synthetic flexibility and unique optical, electronic, magnetic properties derived from the cluster units. The design of clusters with structural complexity has been active in solid state chemistry for a long time. Their assembly into strongly coupled hierarchical lattices has been shown to produce unique material properties. For example, three-dimensional cluster-assembled solids such as Chevrel phases [35] (or derived Chevrel phase $Mo_6S_6Br_2$) and endohedral gallide cluster phase [36] are well-known for their superconducting behaviors. These properties can be flexibly tuned by varying the components of the cluster units. For instant, the critical temperature Tc for superconductivity in $Mo_6S_6Br_2$ (Tc = 13.8 K) is twice larger than that in $Mo_6Se_6Br_2$ (Tc = 7.1 K) by simply replacing sulfur to selenium atoms [37]. Moreover, the inter-cluster assembly plays an important role in rebuilding solids from 3D to 2D or to 1D by changing stoichiometry of the elements in the cluster units. It offers great opportunities to enrich the cluster materials family with desired functionalities.

More recently, a new family of “superatomic crystals” assembled from molecular clusters with analogue structures to the conventional solids has been reported. The idea behind it is to replace atoms in the solids with atomic or molecule clusters called superatomic building blocks [38]. This promising approach can be expanded to the 2D field as demonstrated in Figure 1.1 and some layered van der Waals structures have been successfully synthesized [39,40]. However, the lack

of covalent bonding between these superatoms in the plane prevents their exfoliation down to few layers.

Here we investigate two van der Waals materials derived from the Chevrel phase: $Re_6Se_8Cl_2$ and $Mo_6S_3Br_6$. $Re_6Se_8Cl_2$ cluster is built from isolated Re_6 octahedra enclosed in Se_8 cubes, as shown in Figure 1.2a. Each cluster unit $[Re_6Se_8]$ is linked to four neighbors in the basal plane through strong Re_2Se_2 covalent bonds and is capped by two terminal Cl atoms in the apical positions [41] (details in section 3.2.2). $Mo_6S_3Br_6$ is built from cluster unit $[Mo_6S_4Br_4]Br_4$ (Figure 1.2b) which are covalently linked into layers in different configurations along *b*- and *c*- axes, respectively. Each $[Mo_6S_4Br_4]$ pseudo-octahedron is connected to two neighboring clusters along the *c*-axis via a shared μ_6-S bridge as well as via an additional two bridging Br atoms on the apex. The resulting corner-sharing one-dimensional chains of clusters are linked into layers in the *bc*-plane by means of two interchain Mo–S linkages along the *b*-axis [42] (details in section 4.2.2). The strong inter-cluster bonding in the plane and weak van der Waals interactions between layers in these two crystals allow us to mechanically exfoliate them to thin layers, and their stability under ambient

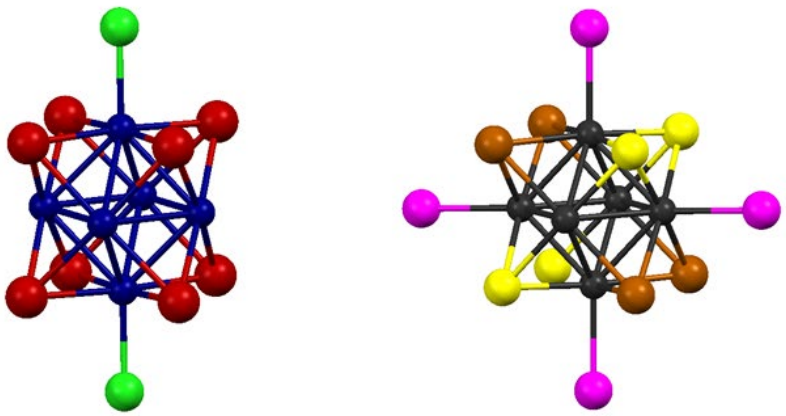

Figure 1.2 Structures of cluster building blocks for a) $Re_6Se_8Cl_2$ and b) $Mo_6S_3Br_6$, respectively. Color code: Re, blue; Se, red; Cl, green; Mo, black; S, yellow; Br, brown (inner-cluster) and pink (inter-cluster bridging).

conditions offers additional benefits for physical studies and device fabrications. $Re_6Se_8Cl_2$ and $Mo_6S_3Br_6$ bulk crystals were first reported in 1983 by Sergent et al. and Perrin et al. respectively, but their physical properties remain essentially unknown. Little connections between these cluster-based layered materials and low-dimensional physics have been made until recent intensive studies on 2D van der Waals materials.

$Re_6Se_8Cl_2$ solid is structurally analogous to bulk MoS_2, a quasi-2D with strong excitonic effects, which makes it interesting to explore the excitonic effects in this bulk material. When the bulk MoS_2 is exfoliated down to monolayer, physical properties (electronic, optical, magnetic and mechanical) change dramatically due to quantum confinement and the different dielectric environment. For instant, the valence band edge at Γ point in momentum space shifts down more than that at K point, modifying it from an indirect to a direct bandgap (E_{BG}) with much larger E_{BG} energy [4,28,43,44]. Therefore, whether the structurally complex 2D $Re_6Se_8Cl_2$ sheets will generate novel physical properties that are different from the 3D counterparts is remarkably interesting while it has never been investigated as a mono- or few-layer materials. Moreover, functionalization of present 2D materials has received remarkable attention due to the ability to tune the physical properties for their potential applications in electronics, optoelectronics, sensing. To achieve it, substitution of host atoms with dopants is required to stabilize the doping within the materials, as demonstrated in traditional semiconductors. Although it has been applied to well-studied graphene [45] and TMDCs [46], functionalizing these atomic solids is difficult and limited in use since it takes much effort to break the covalent bonding in the plane and precise control of the functionalization is still far behind. On the contrast, the complex, hierarchical structure and the presence of substitutional labile Cl atoms on the surface of each $Re_6Se_8Cl_2$ layer open the door to surface functionalization via substitution chemistry, specifically halogen substitution, which could

allow tuning of the electronic structure without destroying the core structures. It has been recently achieved by substituting Cl atoms on the surface with CN ligand in $Re_6Se_8Cl_2$ [47]. Hence, the influence of the surface Cl atoms on the electronic properties needs to be investigated at first.

In Chapter 3, we investigate the electronic properties, particularly excitonic effects in the freshly cleaved $Re_6Se_8Cl_2$ by using scanning tunneling microscopy/spectroscopy (STM/STS) measurement, combined with photoluminescence spectroscopy (PL) and ultraviolet photoelectron spectroscopy (UPS). The experimental findings are supported by density functional theory (DFT) calculations on both bulk and monolayer $Re_6Se_8Cl_2$. We find that bulk $Re_6Se_8Cl_2$ is an indirect bandgap material with the valence band maximum (VBM) located at the Γ (0, 0, 0) point, and the conduction band minimum (CBM) at the T (0, 0.5, 0.5) point in momentum space. STS and PL spectroscopy reveal an electronic bandgap of 1.58 ± 0.03 eV and an optical bandgap of 1.48 eV ± 0.01 eV, respectively. We thus deduce a large exciton binding energy of ~100 meV, which is one order of magnitude larger than the conventional bulk semiconductors [48,49] but comparable to the values of typical van der Waals materials such as bulk MoS_2 [50,51]. This large exciton binding energy is consistent with the partially 2D nature of the exciton confined in layers, which is confirmed by simple Bohr model [52]. Besides, based on STS characterization and DFT calculations of atomic-scale defects, we suggest that Cl vacancies induce mid-gap states and are highly responsible for n-type doping in this material. These results presented in Chapter 3 establish Chevrel-type $Re_6Se_8Cl_2$ as the first member of the 2D hierarchical semiconductor family. Quasi-2D characters besides 2D excitons are expected even in the bulk $Re_6Se_8Cl_2$. This work was published in reference 53.

Similarly, $Mo_6S_3Br_6$, a layered van der Waals materials with superatomic building blocks, is expected to possess strong exitonic effects and 2D characters, which has not yet been investigated.

Moreover, contrast to the nearly isotropic structure of $Re_6Se_8Cl_2$, $Mo_6S_3Br_6$ exhibits strong structural anisotropic in the plane along *b*- and *c*- directions.2D materials with in-plane anisotropy are of great interest for their anisotropic optical, electronic properties and directional transport of carrier and energy, as discovered in black phosphorous [54–57] and α-MO_3 [58]. However, demonstrated examples are very limited even in the atomic solids, is the first layered superatomic van der Waals material combined with in-plane anisotropy. Hence, investigation on the anisotropic properties of $Mo_6S_3Br_6$ is significantly important.

In Chapter 4, we explore the in-plane structural and electronic anisotropy of freshly cleaved $Mo_6S_3Br_6$ surfaces by using scanning tunneling microscopy/spectroscopy (STM/STS) and polarization dependent Raman. The electronic bandgap determined by STS is 1.64 ± 0.05 eV, with the Fermi level (E_F) located at 0.21 eV above the valence band maximum (VBM), indicating intrinsic p-type doping. Density functional theory (DFT) calculations support the pseudo-1D electronic structure of the material and reveal that $Mo_6S_3Br_6$ is a direct bandgap material with the valence band maximum and the conduction band minimum (CBM) located at the S (0, 1/2, 0) point in momentum space. Distinctive anisotropic Raman response of each active mode confirms the strong in-plane electronic anisotropy in $Mo_6S_3Br_6$. Particularly, A_g modes in parallel polarized configuration is separated into two parts: the maximum peak intensity of the A_g modes below 270 cm^{-1} is at 0 º and 180 º while those above 270 cm^{-1} locates at 90 º and 270 º. The paper of this work is submitted.

Both $Re_6Se_8Cl_2$ and $Mo_6S_3Br_6$ belong to the new family of 2D semiconductors whose structures are built from superatomic building blocks instead of simply atoms. Such unique hierarchical structures will expand the design space for 2D van der Waals materials. The weak van der Waals interactions between layers and the strong in-plane bonding contribute to distinctive in-plane and

out-of-plane dielectric environments, which give these layered materials robust 2D character, such as the 2D exciton nature in $Re_6Se_8Cl_2$. Moreover, compared to conventional 2D atomic solids, the complex structures open the door to fabrication of new devices with multiply functions and novel properties. Particularly, the presence of labile Cl atoms on the surface of $Re_6Se_8Cl_2$ and bridging Br atoms on the surface of $Mo_6S_3Br_6$ allows us to tune the electronic properties (e.g. excitonic effects and in-plane anisotropy) by chemical substitution, which is commonly used in solid state chemistry.

Chapter 2

Experimental Techniques

2.1 Scanning Tunneling Microscopy/Spectroscopy

The scanning tunneling microscopy/spectroscopy (STM/STS) is a powerful instrument to detect topological feature and electronic structures at the atomic level. STM was first invented by Greg Binnig and Heinrich Rohrer in 1981 [59], and because of that, they were awarded the Nobel prize in physics in 1986. Over the past decades, STM/STS has been used to study the electronic properties of various systems including metals [60,61], semiconductors [62–64], superconductors [65,66] and topological insulators [67,68]. Moreover, single atoms / molecules manipulation with the STM has been developed to create desired nanostructures and novel quantum phenomenon [69–71], e.g. electron corrals generated by Fe adatoms on Cu (111) surface [69].

2.1.1 Basic principles of STM

STM/STS is based on the phenomenon of quantum mechanical tunneling. An electron with energy E can penetrate through the potential barrier U even in the region E < U, as seen in Figure 2.1a. The wavefunction of the electron decays exponentially along z direction described as

$$\varphi(z) = \varphi(0)e^{-\kappa z} \tag{2.1}$$

where

$$\kappa = \frac{\sqrt{2m(U-E)}}{\hbar} \tag{2.2}$$

is the decay constant. The probability density is proportional to $|\varphi(0)|^2 e^{-2\kappa z}$.

In the model of a metal-vacuum-metal tunneling junction, two metal plates are placed close to each other and the vacuum between them acts as the potential barrier. By definition, work function Φ of a metal is the minimum energy required to remove an electron from a surface into the vacuum. Therefore, if we set the vacuum level as reference energy point $E_{vac} = 0$, the Fermi energy $E_F = -\Phi$ (at T = 0). Assuming the work functions of the tip and sample are the same, no tunneling will happen unless a bias voltage V_B is applied between them. If eV_B is far smaller than Φ, tunneling current can be described as

$$I \propto e^{-2\kappa z} \tag{2.3}$$

where

$$\kappa = \frac{\sqrt{2m\Phi}}{\hbar} \tag{2.4}$$

The typical value of work functions Φ of common metals is ~ 5 eV, which gives $\kappa \sim 10 nm^{-1}$. According to that, the current decays one order of magnitude per 0.1 nm.

Similar to the metal-vacuum-metal tunneling junction, in STM, a shape metallic tip is placed close to the sample surface as shown in Figure 2.1b. When a bias voltage V_B is applied between them, a tunneling current is detected. Electrons tunnel from the occupied states of the tip into the unoccupied states of the sample if positive V_B is applied on the sample with respect to the tip (Figure 2.1c). Electrons flux flows from the sample to the tip if V_B is negative (Figure 2.1d).

The most widely used theory to quantitatively model the tunneling phenomenon in STM is Bardeen's first-order perturbation theory [59,72] proposed by Bardeen and further developed by Tersoff and Hamann [73]. The tunneling current is written as

$$I = \frac{4\pi e}{\hbar}\int_{-\infty}^{\infty}[f(E_F - eV + E) - f(E_F + E)]\rho_t(E_F - eV + E)\rho_s(E_F + E)|M_{\mu\nu}|^2 dE \qquad (2.5)$$

where

$$f(E) = \frac{1}{1+e^{(E-E_F)/k_BT}} \qquad (2.6)$$

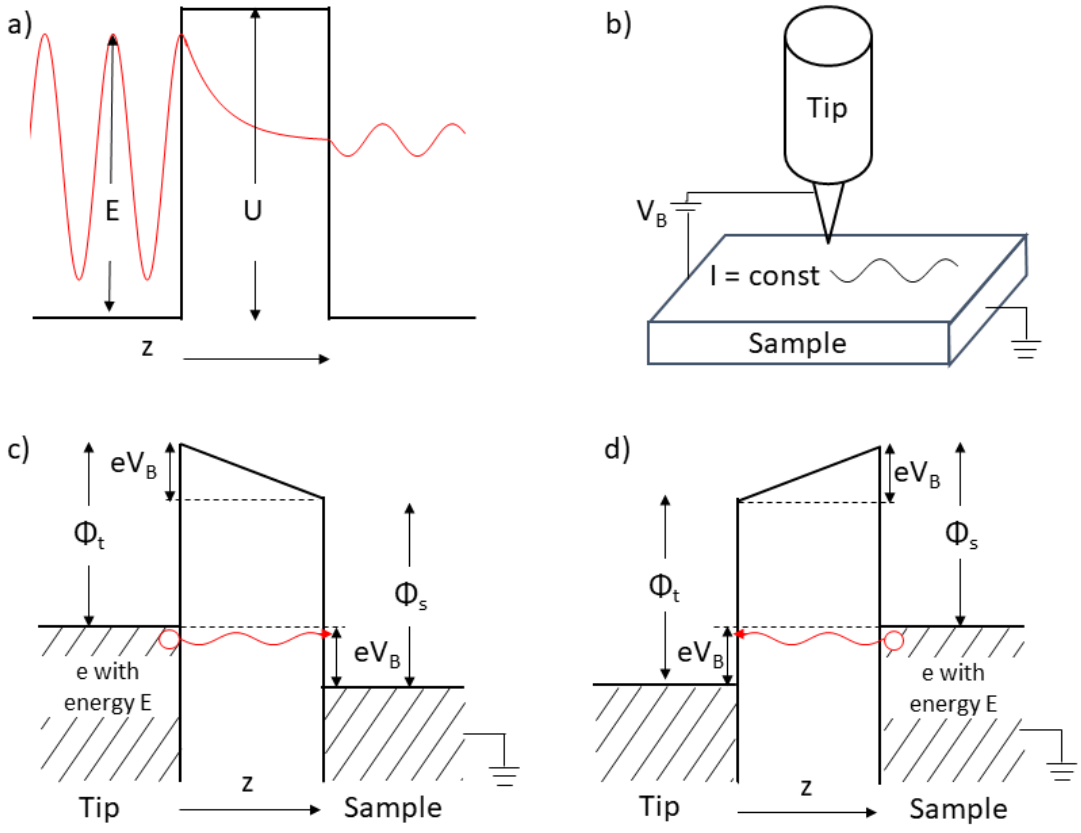

Figure 2.1 Diagrams for electron tunneling. a) A diagram of a simple one-dimensional square potential. An electron with energy E has possibility to tunnel through the potential barrier U. b) A diagram of the constant current imaging mode in STM. c) and d) Tunneling processes with bias voltage V_B applied. Electrons tunnel from the tip to the sample when V_B is positive and vice versa.

is the Fermi-Dirac distribution. $\rho_s(E)$ and $\rho_t(E)$ are the density of states (DOS) at energy E of the sample and the tip, respectively. $M_{\mu\nu}$ is the tunneling matrix element between the sample and the tip and is given by

$$M_{\mu\nu} = -\frac{\hbar^2}{2m}\int(\chi_\nu^*\nabla\psi_\mu - \psi_\mu\nabla\chi_\nu^*)d\boldsymbol{S} \tag{2.7}$$

where ψ_μ and χ_ν are the wavefunctions for state μ of the tip and state ν of the sample and the integral is over the whole tunneling surface. The tunneling matrix element M is proportional to $e^{-\kappa z}$ [72]. Therefore, the resulting tunneling current is a function of applied voltage, local density of states and the tip height. By keeping the tunneling current constant with a feedback loop, the tip height is regulated accordingly at a fixed bias voltage V_B, so that the electronic topography is achieved at the atomic scale.

2.1.2 Basic principles of STS

To simplify the current expression of Eq.2.5, we make three assumptions. 1) the Fermi-Dirac distribution is approximated as a step function if k_BT is smaller than the required energy resolution. It is well fit when STM/STS works in low temperature regime. 2) the tunneling matrix element is treated as a constant in the narrow energy window ($E_F \pm eV$). It is valid when the applied bias potential is far smaller than the work function. Then, the tunneling current is the convolution of the DOS of the tip and the sample. 3) The DOS of the metallic tip is treated as a constant over the energy range. It requires us to characterize the DOS of tip carefully before measurements. Hence, the current can be written as

$$I(V) = \frac{4\pi e}{\hbar}\rho_t|M|^2\int_{E_F}^{E_F+eV}\rho_s(E)dE \tag{2.8}$$

A derivative of I(V) with respect to V gives us the following relation

$$\frac{dI}{dV} \propto \rho_s(E_F + eV) \tag{2.9}$$

The tunneling conductance dI/dV is proportional to the DOS of the sample at energy E = eV. To measure the local density of state (LDOS) experimentally, the tunneling conductance signal is recorded with the help of a lock-in amplifier when a small A.C. modulation $\tilde{V}$ at a random high frequency is applied to the setting bias voltage V_B. The tip position is fixed above the surface with the feedback loop off. Single point spectroscopy is achieved by recording the dI/dV signal over the whole bias voltage V of interest. It produces a one-dimensional curve of LDOS (r,V) at potion r.

2.1.3 Effects of finite temperature

To deduce Eq. 2.9 in section 2.1.2, we assume that the Fermi-Dirac distribution is a step function (in the case of T = 0 K) so that the integral is within the range of [E_F, E_F+eV]. However, it becomes less valid with the increasing temperature, especially when the generated thermal broadening is at the same magnitude as the energy width. To estimate the uncertainty caused by the thermal broadening, we go back to Eq. 2.5, the derivative of current I with respect to bias voltage V becomes

$$\frac{dI}{dV}(V) = \frac{4\pi e}{\hbar}\rho_t|M|^2 \int_{-\infty}^{+\infty} \rho_s(E)\frac{df(E-eV)}{dV}dE \tag{2.10}$$

with the assumption that tunneling matrix element and the density of the tip are constant. Eq. 2.10 can be rewritten as

$$\frac{dI}{dV}(V) = \frac{4\pi e^2}{\hbar}\rho_t|M|^2 \int_{-\infty}^{+\infty} \rho_s(E)\left(-\frac{df(E-eV)}{dE}\right)dE \tag{2.11}$$

At finite temperature, $-\frac{df(E-eV)}{dE}$ has a peak value at E = eV. The full width at the half maximum (FWHM) is

$$\Delta_{FWHM} = 3.53k_BT \tag{2.12}$$

The energy resolution is linearly proportional to the temperature. At 77 K, the energy resolution is 23 meV, and at 298 K (room temperature), the energy resolution increases to 91 meV. In addition,

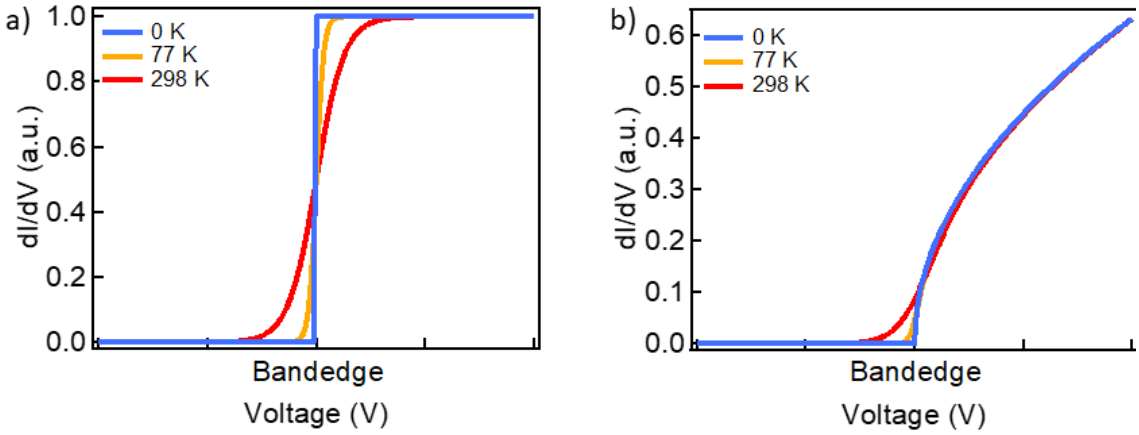

Figure 2.2 Effects of finite temperature on dI/dV-V band edge. Simulation of dI/dV based on Eq. 2.11 at three different temperatures 0 K, 77 K and 298 K respectively. a) is a simple 2D model in which the DOS of the sample is a constant. B) is a simple 3D model in which the DOS of the sample is proportional to $\sqrt{E}$. The band edge becomes more round at room temperature.

from the mathematics point of view, since dI/dV is proportional to the convolution between the LDOS of the sample $\rho_s(E)$ and $-\frac{df(E-eV)}{dE}$, the result can be considered as $\rho_s(E)$ smoothed with the function $-\frac{df(E-eV)}{dE}$. Hence, the band gap edge of a semiconductor is shape at low temperature while it becomes round at room temperature as shown in Figure 2.2. It displays the dI/dV curves at 0 K, 77 K and 298 K respectively in simple 2D (left) and 3D (right) models. The apparent band edge (baseline dI/dV = 0) is smaller than the real value, the offset enlarges with increasing T. Therefore, we need to include the thermal broadening effects in the analysis of the STS spectra.

2.1.4 Effects of tunneling matrix element

In section 2.1.2, the tunneling matrix element M is considered as a constant at a small bias voltage. This assumption is not always valid, especially at higher bias voltages. Matrix element M can be well estimated by the Wentzel-Kramers-Brillouin (WKB) approximation for the transmission probability through a simple planar tunneling model. It can be written as

$$|M|^2 = e^{-2\kappa d} \tag{2.13}$$

with

$$\kappa = \frac{\sqrt{2m}}{\hbar}\sqrt{\frac{\phi_s+\phi_t}{2}+\frac{eV_B}{2}-E} \tag{2.14}$$

Hence, the matrix element is dependent on the energy of the state E and the distance d between the sample and the tip. As mentioned in section 2.1.1, the work function of the sample and tip is ~ 4-5 eV, assuming d = 1 nm and V_B = 1.5 V, then the value of $|M|^2$ at E=eV_B is 5 times larger than that at E = 0. In addition, $|M|^2$ changes by an order of magnitude when d varies by 0.1 nm. Therefore, we need to take into consideration of the matrix element changes while simulating the STS curves as well.

2.2 Time Resolved Two-Photon Photoemission

The time-resolved two-photon photoemission (TR-2PPE) is another powerful tool to study the electronic structure [74] and the dynamics of the electronic excitation on the sample surface and interfaces. This pump-probe photoexcitation was first realized experimentally in the 1970s [75,76], and further developed in the past decades. The invention of the femtosecond and picosecond laser pulses greatly improves the temporal resolution, which allows directly observing the ultrafast dynamic processes, e.g. exotic electron relaxation [77–79], Auger recombination [80,81] and charge transfer dynamics at interfaces [82,83]. Furthermore, the generation of high harmonics extends the pump energy from the visible / near ultraviolet range into the extreme ultraviolet (XUV)

regime [84,85]. Electrons with high parallel momentum can be excited into vacuum with this photon energy. It therefore expands the accessible momentum space, which allows monitoring the electronic dynamics in high k points in the momentum space.

2.2.1 Photoelectron spectroscopy

Photoelectron spectroscopy (PES) is based on photoelectric effects which means electrons emitted from a material with the absorption of photons. To realize it experimentally, it has two main requirements. 1) A photon with enough energy to overcome the ionization potential of the electronic states of interest. In addition, the inelastic mean free path λ_{mp} of these photoexcited

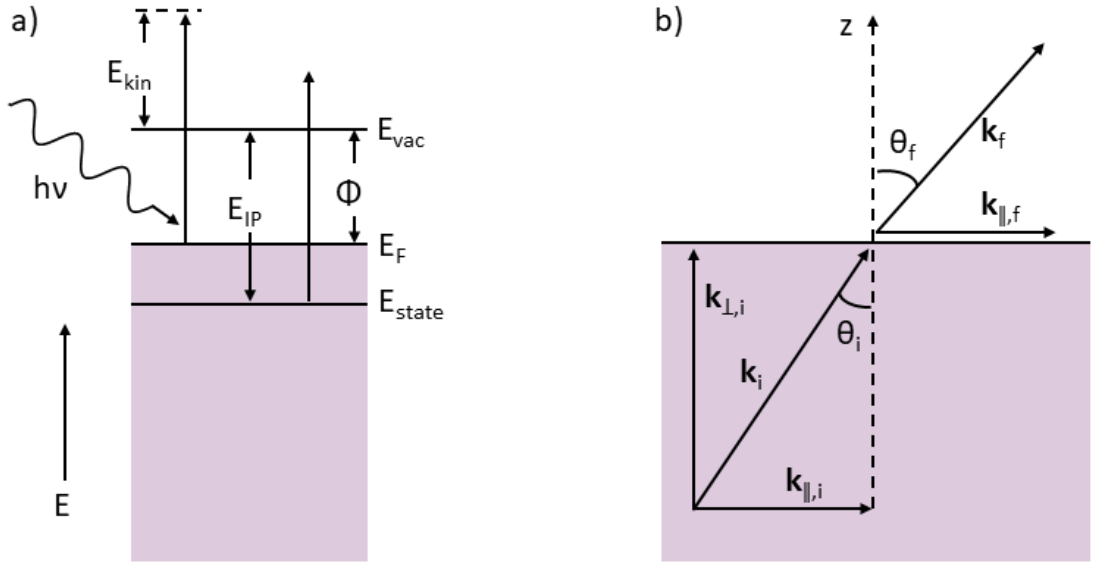

Figure 2.3 Schematic energy diagram for photoemission. a) An electron absorbs a photon with energy hν and escapes into vacuum through overcoming the ionization potential (E_{IP}). The excess energy is converted into the kinetic energy of this ionized electron. b) Schematic momentum diagram for photoemission. The perpendicular component $k_\perp$ gets reduced while the parallel component $k_\parallel$ is conserved during the whole process.

electrons inside the materials is very short ($\lambda_{mp} \leq 10$ Å over a wide energy range), which makes PES highly surface sensitive. 2) Free electrons are not influenced by the environment between the sample and analyzer. Therefore, experiments are carried out in ultrahigh vacuum which allows the mean free path of the electrons are longer than the pathway. Besides, no electric and magnetic fields are inside the chamber to affect the trajectory of the electrons unintentionally.

The obtained spectroscopic signals contain much important information about the sample properties (energetical, spatial, temporal et al.), hence, many techniques based on PES have been emerged. One of the widespread useful techniques is angle-resolved one-photon photoemission spectroscopy (1PPE). The process is described in the scheme of Figure 2.3a. An electron is emitted from an electron state of a material with the absorption of a photon. The photon energy hν is higher than the ionization potential (E_{IP}) of that state and the excess energy is converted to the kinetic energy of the electron (E_{kin}). Due to the energy conversation, the kinetic energy is described as

$$E_{kin} = h\nu - E_{IP} \tag{2.15}$$

Setting E_F as the reference energy, the kinetic energy can be written as

$$E_{kin} = h\nu - \phi - E_B \tag{2.16}$$

where Φ is the work function of the material, and E_B is the binding energy of the electron. The highest kinetic energy an electron can have is $E_{kin,max} = h\nu - \Phi$. The lowest kinetic energy of an electron is $E_{kin,min} = 0$. Hence, by measuring the absorbed photon energy hν and the energy width of the E_{kin}, we can determine the work function Φ of the material and then the occupied states of interest.

In addition, electronic dispersion relation E(**k**) can be obtained in angle-resolved 1PPE. During the photoemission process, electrons loss energy and momentum to overcome the vacuum barrier

in the direction perpendicular to the sample surface while the parallel momentum $k_\parallel$ is conserved, as shown in Figure 2.3b. By measuring the kinetic energy E_{kin} and the final emission angle θ_f (differ from the initial angle θ_i), the parallel momentum $k_\parallel$ can be determined as

$$k_\parallel = \frac{\sqrt{2m_e E_{kin}}}{\hbar} sin\theta_e \tag{2.17}$$

$$k_\parallel = 0.512 \text{Å}^{-1} eV^{-1/2} sin\theta_e \sqrt{E_{kin}} \tag{2.18}$$

2.2.2 Time-resolved two-photon photoemission

Although angle-resolved 1PPE provides information on the energy and momentum of the occupied states of the material (band dispersion of the valence band for solids) at equilibrium, it has two limitations. 1) No unoccupied states e.g. conduction band of a solid are detected. To observe the conduction band, high electron doping e.g. potassium doping, is needed to lower the conduction band minimum (CBM) below E_F [86,87]. 2) It is lack of information of the non-equilibrium states and their dynamics. It is therefore necessary to introduce a second photon into the system with a time delay Δt with respect to the first photon. This technique is called time-resolved two-photon photoemission (TR-2PPE).

The process is described in Figure 2.4: the system is excited from valence band (VB) into a non-equilibrium conduction band (CB) state with the absorption of the first photon $h\nu_1$ (pump). $h\nu_1$ is generally close or larger than the bandgap ($h\nu_1 > E_g$) in a semiconductor or the energy difference between the initial state and the intermediate state of interest. While it needs to be smaller than the work function to avoid the direct 1PPE process. Then electrons in the excited states are ionized to above the vacuum level E_{vac} by absorbing the second photon with energy $h\nu_2$ (probe). The probe should have energy higher than the ionization potential of the excited states. By measuring the

kinetic energy E_{kin} of the electrons, the energy level of the excited state relative to E_F can be determined as

$$E - E_F = E_{kin} + \phi - h\nu_2 \tag{2.19}$$

The kinetic energy shifts by the probe energy difference $\Delta h\nu_2$. In addition to this two-color 2PPE process, single-color 2PPE happens at the same time, which means that electrons at the initial states (VB) are ionized by absorbing the two photons (either pump or probe) simultaneously. The kinetic energy shifts with twice the photon energy difference $2\Delta h\nu$. Therefore, by monitoring the kinetic energy changes with a variation of pump or probe energy, we can determine the origin of the states. Moreover, since single-color 2PPE is independent on the time sequence of the pump and probe, these signals can be treated as a background signal which can be subtracted.

During the pump-probe photoemission process, electrons are excited into the non-equilibrium states with the absorption of the pump photons. There are several decay channels for the system

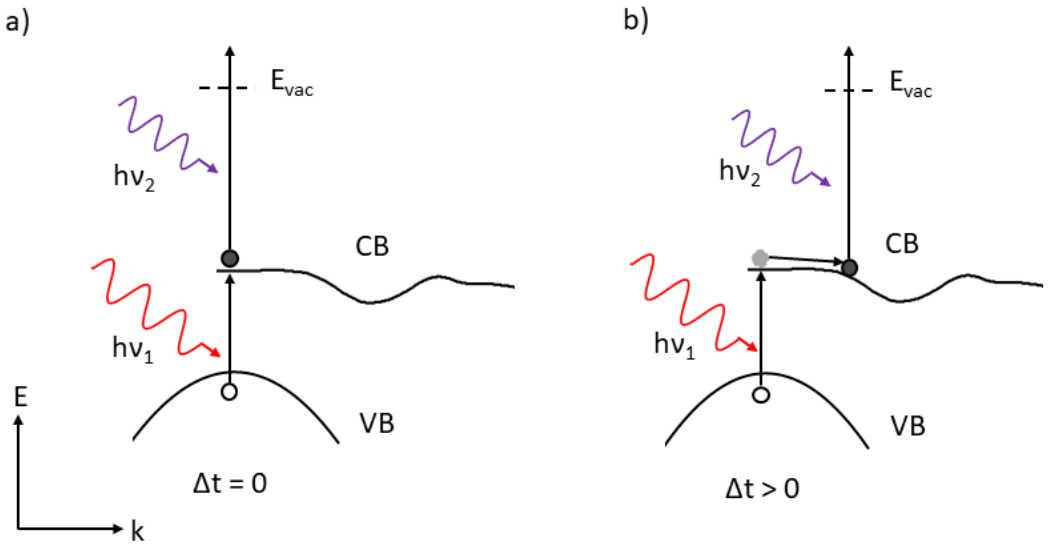

Figure 2.4 Schematic for photoemission process at different time delays. a) pump $h\nu_1$ and probe $h\nu_2$ arrive the sample at the same time with time delay $\Delta t = 0$, generating signals at the corresponding kinetic energy level with the momentum dispersion. b) probe $h\nu_1$ arrives the sample and pumps electrons into the excited CB states. Then, electrons relax to the lower energy level. After time delay Δt, probe arrives the sample, generating a new photoemission spectrum.

to return to equilibrium. Besides, electrons also experience relaxation via electron-electron or electron-phonon interactions. To observe these dynamic processes, time delay Δt between the pump and probe pulse is essential. If $\Delta t < 0$, probe $h\nu_2$ arrives the sample before pump $h\nu_1$, only single-color 2PPE signals may be recorded. At $\Delta t = 0$, pump and probe arrive the sample at the same time, and signals represent the original status of the excited states. While $\Delta t > 0$, electrons could relax into the lower energy level as shown in Figure 2.4b, and the excited states (CB) population changes accordingly. To realize it experimentally, the optical path length of pump or probe pulse is changed with a delay stage to generate a sequence of time delay Δt with a selected delay step size. Photoemission spectra are gained at various time delay Δt and the collection provides the information on the excited state population dynamics. Hence, depending on the pulse duration and the selected time delay, TR-2PPE is a powerful tool to directly observe various ultrafast dynamic processes ranging from nanosecond (10^{-9} s) to femtoseconds (10^{-15} s), even to attosecond (10^{-18} s) timescales.

2.2.3 Ultrafast laser system of TR-2PPE

Ultrafast laser system is used to generate tunable ultrashort light pulses as the pump and probe for TR-2PPE measurements. It is realized by means of nonlinear optical effects, mainly non-collinear optical mixing (NOPA). The schematic of the optical setup is depicted in Figure 2.5.

The source of the pump and probe pulses is the commercial fiber laser system (Clark-MXR, Inc. model IMPULSE) which generates a single, low-bandwidth near infrared (NIR) pulse centered at a wavelength of ~1040 nm. The energy per pulse is ~ 10 μJ with pulse duration of 250 fs. The repetition rate used in experiments is 809 kHz. This low energy and high repetition rate output helps generate high electron counts detected by the analyzer and reduce or avoid the space charge effects during the photoemission process. This fundamental pulse enters the home-built NOPA

system and is split into two components. One (~ 15% of the power) is used to generate white light continuum (WLC) as the seed for the NOPA process. The non-linear medium we chose for WLC is an undoped yttrium aluminum garnet (YAG) crystal since it produces broad spectrum (500 – 920 nm) for use and has low power threshold. This broadband WLC is cut at 650 nm into two parts with different frequency regions. First one with lower wavelength (500 – 650 nm) is used for Visible NOPA generation while the second (650 -920 nm) is used for infrared NOPA generation. The remaining of the fundamental output (~ 85% of the power) is used to generate the pump pulse for the NOPA process. It first produces an second harmonic (SHG) pump centered at 520 nm by mixing itself in a β-barium borate (BBO) crystal, a common nonlinear medium used for frequency mixing ($\omega + \omega = 2\omega$). The SHG pump and the remaining NIR pump then mixed in a second BBO crystal via sum frequency generation (SFG) to generate a third-harmonic (SHG) pump centered at 367 nm ($\omega + 2\omega = 3\omega$). The SHG and THG are used for IR and visible NOPA generation, respectively.

In the NOPA process, the pump pulse (ω_{pump}) decays into two lower energy photons via difference frequency generation (DFG). By mixing it with a seed frequency, a desired frequency signal can be stimulated (ω_{signal}) and the remaining photon is called idler. In the other word, a weak WLC can be amplified into an intense signal with an intense pump pulse in experiments.

Due to the energy and momentum conservation, the pump, signal and idler pumps need to satisfy

$$\omega_{pump} = \omega_{signal} + \omega_{idler} \tag{2.19}$$

$$\boldsymbol{k}_{pump} = \boldsymbol{k}_{signal} + \boldsymbol{k}_{idler} \tag{2.20}$$

where **k** is the wave vector of each photon. To achieve the frequency tunability, there is an angle between the pump and seed. By changing this angle to the right phase matching angle, various frequency can be generated. Besides, it requires that the pump and seed have both spatial and

temporal overlap in the BBO crystal. Since light with higher frequency (blue) travels slower than the lower frequency (red) in the YAG crystal, this broadband WLC is chirped and has a long pulse duration over 1 ps. That means only partial of the WLC spectrum temporally overlaps with the pulse, therefore, only partial of the WLC spectrum is amplified by the pump. By varying the time delay between the pump and WLC, we can selectively amplify the frequency as desired.

After that, the produced NOPA pulses are compressed by a chirp mirror pair (CMP) with negative group velocity dispersion (GVD). By tuning the bounces on the CMP, we reach to the minimum pulse duration and the pulse can't be compressed any more. The visible NOPA is then sent to a 15

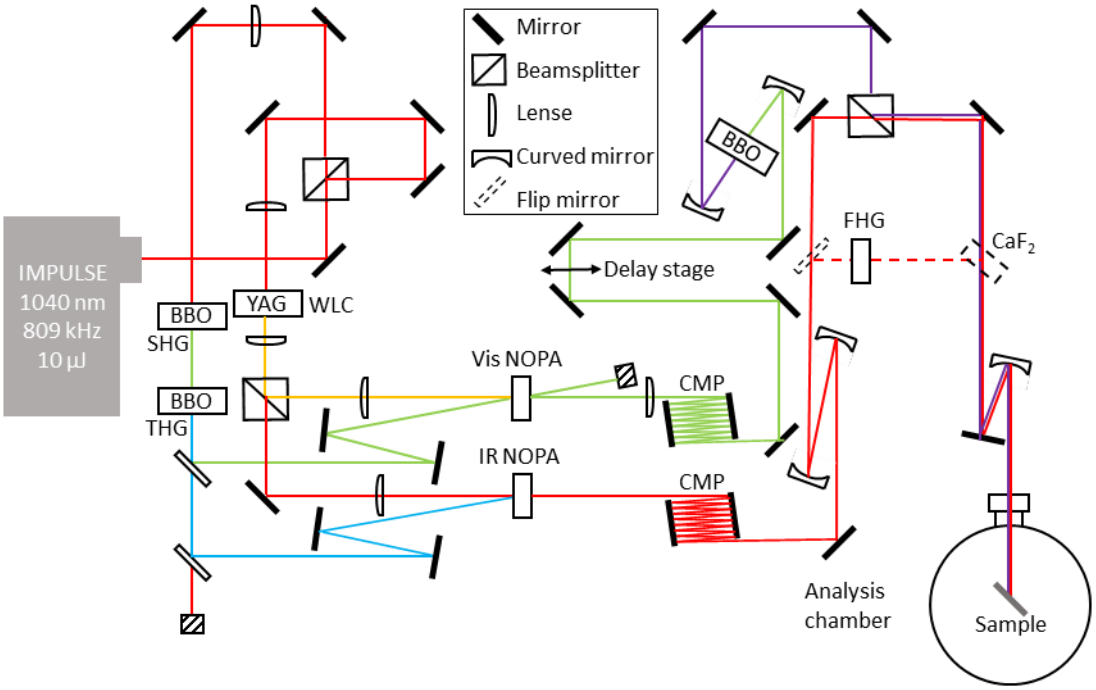

Figure 2.5 Schematic of the NOPA laser system. The fundamental output is split to two components. One is sent to an undoped YAG crystal to generate white light continuum (WLC), acting as the seed for the NOPA. The remaining is used for SHG and THG to produce the pump pulse for the NOPA. CMP represents the chirped mirror pairs which is used to compress the NOPA output. Delay stage is used to control the delay time between the pump and probe for the 2PPE measurements. The visible NOPA is further converted to a UV pulse if necessary. The generated IR and UV pulses are collinearly focused on the sample through a curved concave mirror. An optional deep UV pulse can be generated via FHG.

cm long delay stage. By moving the delay stage, the delay time between the pump and probe is controlled accordingly. It is sufficient for us to study the ultrafast dynamic processes in the timescale of femtoseconds or picoseconds.

To enlarge the energy range of the pump and probe, there is another optional BBO crystal for SHG after the compressed visible and infrared NOPA, respectively. Hence, it can generate a deep ultraviolet (UV) pulse with energy up to 4.8 eV. In addition, an optional high harmonic generation setup (Inrad Optics) is placed after the IR NOPA for fourth harmonic generation (FHG). It is designed for near IR input (700 – 900 nm) and deep UV output with energy as high as 6.0 eV. A BBO and a lithium tri-borate (LBO) are utilized for two successive steps of SHG and generate the final fourth harmonic pulse.

2.2.4 Photoelectron analyzer of TR-2PPE

The hemispherical analyzer (Scienta Omicron) is connected to the analysis chamber, where the prepared sample locates. It has three main components: electrostatic lens system, the concentric hemispheres and the multi-channel plate (MCP) detector with a CCD camera. When the pump and probe pulses arrive on the sample, electrons are emitted at various angles. To detect these electrons properly, the position of the sample is critical. The distance between the sample surface and the analyzer is fixed so that the focus of the lens system locates on the surface. Moreover, the surface normal needs to align with the center axis of the lens system. When electrons enter the electrostatic lens, they are retarded or accelerated to the kinetic energy E_p (pass energy) and focused onto the entrance slit. Electrons are further dispersed in the concentric hemispheres and projected on the multi-channel plate (MCP). The electron trajectory is determined by the kinetic energy (up-down direction in the MCP) and the emission angle (left-right direction). Hence, electron dispersion relation $E(\mathbf{k})$ is obtained by recording the signal of the two-dimensional electron distribution.

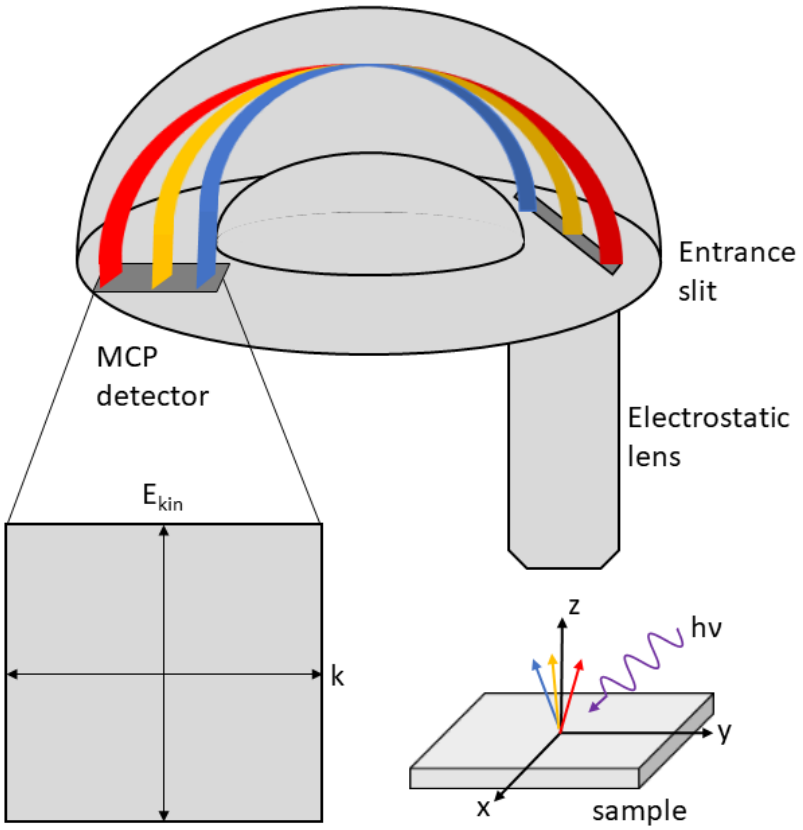

Figure 2.6 Schematic of the analyzer. Electrons are emitted from the sample by the absorption of photons with energy hv. A portion of them enters the electrostatic lens system and is retarded or accelerated to the kinetic energy E_p (pass energy) and focused onto the entrance slit at various angles. The hemisphere disperses the electrons and projects them onto a 2D MCP detector. Electron trajectories are determined by the kinetic energy E_{kin} and the emission angle θ_e.

Chapter 3

Exitonic Effects in Superatomic Semiconducting $Re_6Se_8Cl_2$

3.1 Introduction

$Re_6Se_8Cl_2$ is a van der Waals material derived from the Chevrel phase in which [Re_6Se_8] clusters are covalently linked into layers capped by terminal Cl atoms [41,88]. Layers are stacked together by the van der Waals force. This weak interlayer interactions compared with the strong in-plane inter-cluster bonding allows us to mechanically exfoliate the crystal. Their stability under ambient conditions offers additional benefits. $Re_6Se_8Cl_2$ was first reported in 1983 by Sergent and coworkers but little is known about its physical properties. The widespread studies on the 2D materials bring our attention on this layered semiconductor. $Re_6Se_8Cl_2$ solid is structurally analogous to bulk MoS_2, a quasi-2D with strong excitonic effects, it is intriguing to explore the excitonic effects in this bulk material. When the bulk MoS_2 is exfoliated down to monolayer, the physical properties change dramatically, for example, the bandgap (E_{BG}) changes from indirect to direct with much larger E_{BG} energy [4,28,43,44]. Therefore, whether the structurally complex 2D $Re_6Se_8Cl_2$ sheets will generate novel physical properties that are different from the 3D counterpart

is very interesting while remains unclear. Moreover, the presence of substitutional labile Cl atoms on the surface of each $Re_6Se_8Cl_2$ layer opens the door to surface functionalization via substitution chemistry, which could allow tuning of the electronic structure. Hence, the influence of the surface Cl atoms on the electronic properties needs to be investigated.

To better understand these properties, we carry out scanning tunneling microscopy/spectroscopy (STM/STS) measurement, combined with photoluminescence spectroscopy (PL) and ultraviolet photoelectron spectroscopy (UPS), on freshly cleaved $Re_6Se_8Cl_2$ crystals. The experimental findings are supported by density functional theory (DFT) calculations on both bulk and monolayer $Re_6Se_8Cl_2$.

3.2 Sample preparation and characterizations

Single crystals of $Re_6Se_8Cl_2$ are grown by chemical vapor transport. The material is first synthesized as microcrystalline powder and then grown to millimeter-sized single crystals. The structure of isolated crystals is determined by single crystal x-ray diffraction (SCXRD) and the phase purity of each sample is confirmed by powder x-ray diffraction (PXRD).

3.2.1 Crystal synthesis

A mixture of Re (330 mg, 1.7 mmol), Se (190 mg, 2.4 mmol), and $ReCl_5$ (200 g, 0.5 mmol) was intimately ground in an inert atmosphere, pressed into a pellet, and sealed in a quartz tube under vacuum. The sample was heated to 1100 °C with a ramp of 1 °C/min, and held at 1100 °C for 3 days. The reaction takes place in the presence of $ReCl_5$ vapor that is maintained by the addition of slight excess of Re and $ReCl_5$. Large single crystals of mm scale can be grown by subsequent chemical transport using $ReCl_5$ as the transport reagent with a temperature gradient of 970-920 ºC. Large crystals are deposited at the cooler end of the tube. Before opening the sealed tube, the

excess $ReCl_5$ that are deposited on the crystals is removed by condensing it to the cooler side of the tube by maintaining the tube under a temperature gradient of 300-25 ºC for about 3 h. The chemical reaction can be expressed as

$$5.2\ Re + 7\ Se + 0.8\ ReCl_5 \rightarrow \mathbf{Re_6Se_8Cl_2} + 0.85\ ReCl_3$$

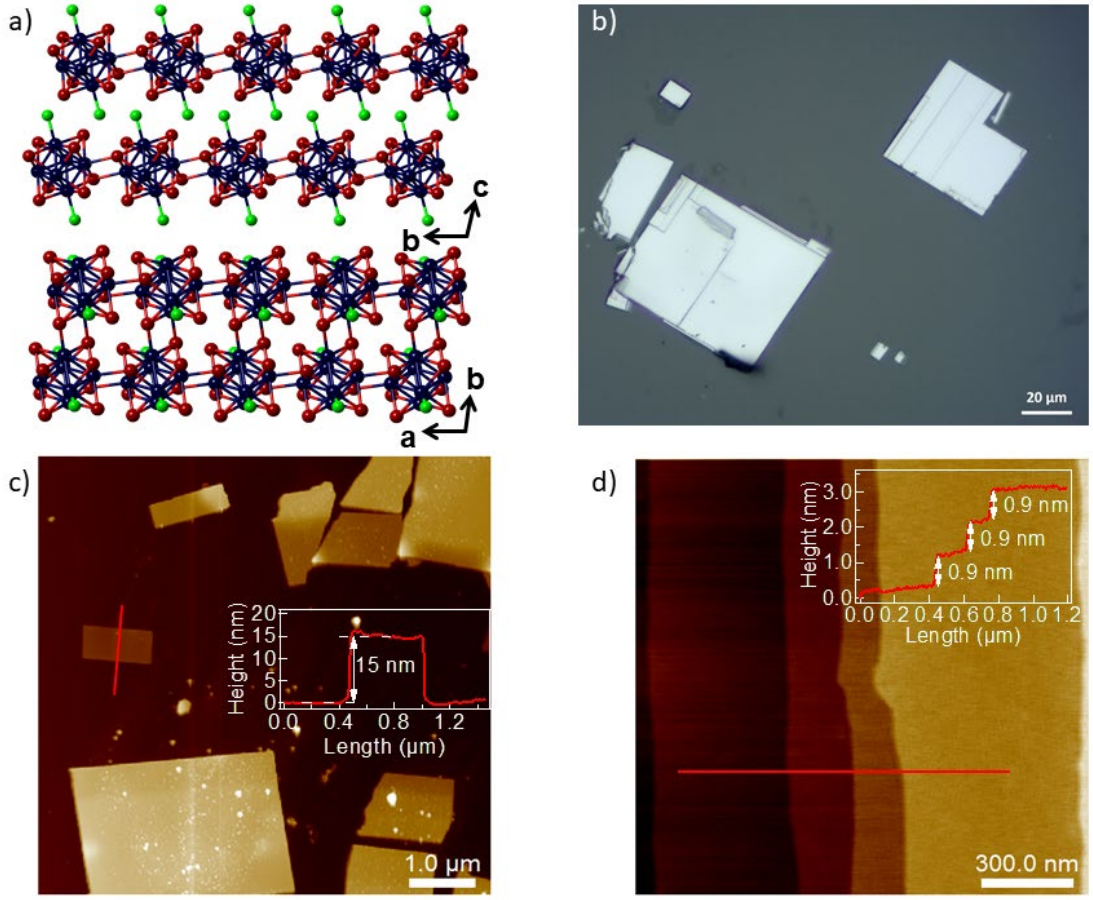

Figure 3.1 Crystal structure of $Re_6Se_8Cl_2$. (a) Side view (top) of the *ab* plane and top view (bottom) of a single layer. Color code: Re, blue; Se, red; Cl, green. b) Optical image of the grown crystals. The rectangular shape agrees well with the crystal structure. c) Exfoliated $Re_6Se_8Cl_2$ flakes on SiO_2/Si. The height profile in red (insert) shows the thickness of a ~15 nm thin flake. d) Zoom-in AFM image with image size: 1500 x 1500 nm. Inset is the line profile across the steps (along the red line), showing the average height of 0.9 nm, agreeing with the monolayer thickness.

$Re_6Se_8Cl_2$ crystalizes in a triclinic lamellar structure with space group $P\bar{1}$ (space group No.2). The $Re_6Se_8Cl_2$ cluster unit is built from isolated Re_6 octahedra enclosed in Se_8 cubes. Each cluster unit

is linked to four neighbors in the basal plane through strong Re_2Se_2 bonds, and is capped by two terminal Cl atoms in the apical positions (Figure 3.1a). The layers are pseudo-square lattices of tilted clusters, with lattice parameters a = 5.58 Å, b = 6.62 Å and γ = 86.4 °. Layers are stacked together by van der Waals force and the lattice parameter normal to the layers is c = 8.80 Å (Figure 3.1b).

The grown crystals have the rectangular shape, which is consistent with the in-plane pseudo-square structure. Our initial attempts at mechanical exfoliation using the Scotch tape method produced rectangular flakes as thin as ~15 nm, as determined by atomic force microscopy (AFM) (Figure 3.1c). The zoom in image (Figure 3.1d) shows an ultra-clean and flat surface with average roughness of 0.4 Å. Each step height along the red line is 0.9 nm (Inset Figure), in good agreement with the monolayer thickness. AFM measurements were carried out with Bruker Dimension FastScan AFM using Peakforce tapping mode. All AFM images were analyzed using NanoScope Analysis.

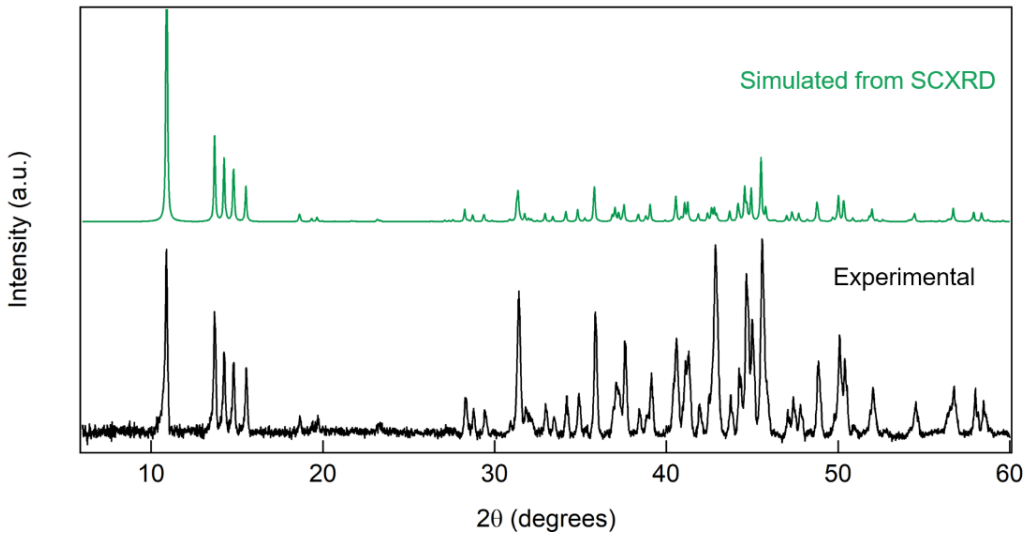

Figure 3.2 PXRD of $Re_6Se_8Cl_2$ simulated from SCXRD data (top) and experimental (bottom).

The structure of the synthesized crystals was characterized by the single crystal X-ray diffraction (SC-XRD). Data were collected on an Agilent SuperNova diffractometer using mirror-monochromated Mo Kα radiation. The crystal was mounted using a MiTeGen MicroMount cooled to 100 K with an Oxford-Diffraction Cryojet system. Data collection, integration, scaling (ABSPACK) and absorption correction (face-indexed Gaussian integration [89] or numeric analytical methods [90]) were performed in CrysAlisPro. Structure solution was performed using ShelXT [91]. Subsequent refinement was performed by full-matrix least-squares on F [90] in ShelXL [92]. Olex2 [93] was used for viewing and to prepare CIF files. Details of crystallographic data and parameters for data collection and refinement are in Table 3.1, which is consistent with previous experimental results [41,94].

Table 3.1. Selected crystallographic data

Formula	$Re_6Se_8Cl_2$
MW	1819.78
Space group	P-1
***a* (Å)**	6.5784(7)
***b* (Å)**	6.6194(8)
***c* (Å)**	8.8010(9)
***α* (°)**	76.708(9)
***β* (°)**	70.204(9)
***γ* (°)**	86.368(9)
V (Å^3)	350.88(6)
Z	1
ρ_{calc} (g cm^{-3})	8.612
T (K)	100
λ (Å)	0.71073
$2\theta_{min}$, $2\theta_{max}$	6.8292, 59.2636
Nref	7041
R(int), R(σ)	0.0470, 0.0445
μ(mm^{-1})	73.093
Size (mm)	.024 x .02 x .013
Data	1757

Restraints	0
Parameters	73
R_1(obs)	0.0311
wR_2(all)	0.0693
S	1.106

Powder X-ray diffraction (PXRD) data were collected on a PANalytical X'Pert Powder diffractometer. Small crystals were evenly dispersed, uncrushed, on a zero-background Si plate. The phase purity of each sample is confirmed by comparing the experimental data with the simulated one from the crystal structure (Figure 3.2).

3.3 Optical properties of thin layer $Re_6Se_8Cl_2$

3.3.1 Optical band gap determination

Optical absorption and emission are two fundamental processes when the system is exposed to the light. Photon absorption in a semiconductor can be described as an energy transfer process. Electrons in the valence band are excited into the conduction band with the absorption of photons when the photon energy is equal or larger than the bandgap energy E_g. It leaves holes in the valence band and generates electron-hole pairs (e-h pairs). During the process, energy and momentum need to be conserved. It can be satisfied in a direct band to band transition in direct bandgap semiconductors (e.g GaAs,InP [49,95]) . While in an indirect semiconductor (e.g. Si,Ge [96]), phonons are commonly involved in the optical absorption and emission, as shown in Figure 3.2a. The absorption coefficient α is used to define the amount of light the system absorbs and 1/α is the penetration depth based on the Lambert- Beer's law:

$$I = I_0 e^{-\alpha(\omega)d} \tag{3.1}$$

where I_0 is the laser intensity and d is the traveling distance in the material. The absorption coefficient α is strong wavelength dependent. It increases rapidly when the phonon energy reaches to the bandgap energy. Hence, by measuring the absorption coefficient as a function of wavelength, we are able to determine the optical bandgap of the material. Optical band gap is different from the electronic band gap, especially in the systems with strong excitonic effects (Details in section 3.4).

Experimentally, transmittance and reflectance measurements were carried out on thin $Re_6Se_8Cl_2$ flakes and converted to absorption spectrum (details see section 3.3.3). Samples were prepared by

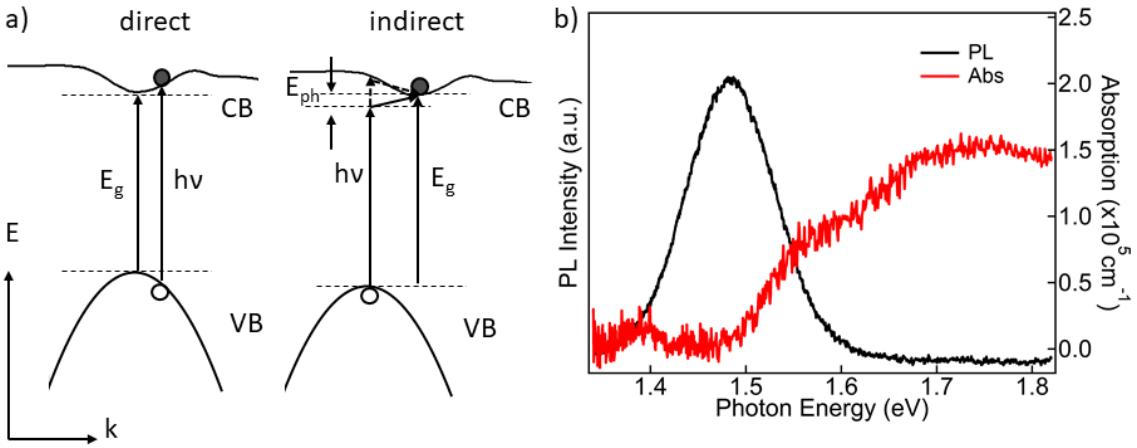

Figure 3.3 Schematic of optical absorption and the spectrum of $Re_6Se_8Cl_2$ a) Electron inter-band transitions in direct (left) and indirect (right) semiconductors. Phonons are involved in the indirect bandgap semiconductors (neglecting excitonic effects). b) Optical absorption (red) and photoluminescence (black) spectra of $Re_6Se_8Cl_2$. The onset of absorption spectrum at 1.49 ± 0.02 eV agrees with the PL peak position at 1.48 ± 0.01 eV.

mechanically exfoliating the single crystals of $Re_6Se_8Cl_2$ and then characterized with AFM. These samples are as thin as ~ 30 nm. Two different white light sources were used to measure these thin samples with 40x objectives. Transmitted and reflected lights were collected at room temperature and spectrally resolved with Princeton Instruments PhotonMAX EMCCD camera. Figure 3.2b

(red) presents the resulting absorption spectrum. The onset of absorption gives an optical gap E_{OG} = 1.49 ± 0.02 eV.

3.3.2 Dielectric function determinations

As described in section 3.3.1, instead of directing measuring the absorption of the sample, transmission and reflection measurements were carried out experimentally on thin $Re_6Se_8Cl_2$ flakes on a transparent substrate (high quality BK7 optical glass). The incident light is normal to the sample surface. By using the classical theory of electromagnetic waves described by Maxwell's equations, the relation between absorption coefficients, complex dielectric constant, refractive index and reflectance (R) and transmittance (T) can be derived [97,98].

Spectra shown in Figure 3.4 were collected on a film with thickness of 43 nm. T and R strongly depend on the wavelength of the incident light (Figure 3.4a).

The relation of complex refractive index n_0+ik_0 (including the air, film and substrate) and T, R can be expressed as:

$$\frac{1+R}{T} = \frac{1}{4n_2(n_1^2+k_1^2)}[(n_1^2+1+k_1^2)\{(n_1^2+n_2^2+k_1^2)cosh2\alpha_1 + 2n_1n_2sinh2\alpha_1\} + (1-n_1^2 - k_1^2)\{(n_1^2-n_2^2+k_1^2)cosh2\gamma_1 - 2n_2k_1sinh2\gamma_1\}] \quad (3.2)$$

$$\frac{1-R}{T} = \frac{1}{2n_2(n_1^2+k_1^2)}[n_1\{(n_1^2+n_2^2+k_1^2)sinh2\alpha_1 + 2n_1cosh2\alpha_1\} + k_1\{(n_1^2-n_2^2+k_1^2)sinh2\gamma_1 + 2n_2k_1cosh2\gamma_1\}] \quad (3.3)$$

where

$$\alpha_1 = \frac{2\pi k_1 d}{\lambda} \quad (3.4)$$

$$\gamma_1 = \frac{2\pi n_1 d}{\lambda} \quad (3.5)$$

where n_0,n_1,n_2 are the refractive index and k_0,k_1,k_2 are the extinction coefficient of the air, film and the substrate, respectively. n_0=1for air or vacuum mediums and k_2=0 for the transparent substrate. Given experimental results of (1±R)/T, sample thickness d, n_2 for the known substrate and the wavelength λ, we are able to solve the equations and get the values of n_1 and k_1 of the $Re_6Se_8Cl_2$ thin film, as plotted in Figure 3.4b.

Since the complex dielectric constant κ is defined as:

$$\sqrt{\kappa} = n_0 + ik_0 \tag{3.6}$$

The real (κ_1) and imaginary (κ_2) parts of the complex dielectric constant are then expressed as:

$$\kappa_1 = n_0^2 - k_0^2 \tag{3.7}$$

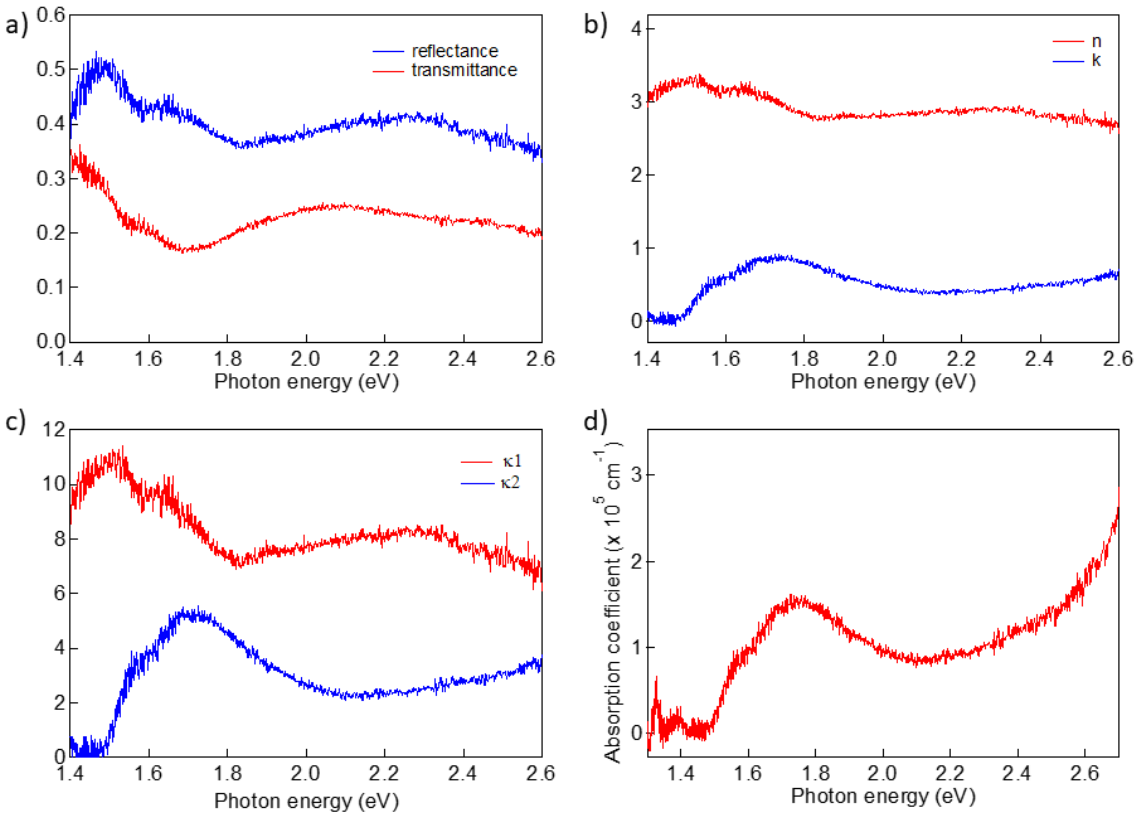

Figure 3.4 Dielectric function determination. Reflectance (R) and transmittance (T) of a 43nm $Re_6Se_8Cl_2$ thin film on a BK7 optical glass. b) index of refraction n and extinction coefficient k. c) Real and imaginary dielectric constants κ_1 and κ_2. d) absorption coefficient converted from reflectance and transmittance.

$$\kappa_2 = 2n_0k_0 \tag{3.8}$$

Intensity of the transmitted light is proportional to the quadratic of electromagnetic waves E_t, hence, the absorption coefficient can be derived as

$$\alpha = \frac{\omega\kappa_2}{n_0c} \tag{3.8}$$

where ω is the angular frequency of the incident.

Therefore, the optical bandgap can be determined as the onset of the absorption coefficient (Figure 3.4d), as mentioned in section 3.3.1. The dielectric constant at the band edge (1.49 eV) is ~ 10.5 (Figure 3.4c).

3.3.3 Temperature dependent PL measurements

In a semiconductor system, e-h pairs are generated with the absorption of phonons. These e-h pairs undergo energy and momentum relaxation mainly through Coulomb scattering or the interaction with phonons. Electrons then recombine with holes through different decay channels (non-radiative or radiative). Photoluminescence (PL) is one of the most important recombination processes, in which photons are emitted as electrons recombine with holes in the valence band.

Temperature-dependent PL measurements was performed on $Re_6Se_8Cl_2$ with the excitation of a 532nm CW laser at power of 100 W/cm^2. $Re_6Se_8Cl_2$ crystal was cleaved before mounting onto a cryostat to achieve clean surface. Emission from the sample was collected with Princeton Instruments PyLoN-IR InGaAs camera. The sample was first cooled with liquid nitrogen, and spectra were acquired at temperature from 80 K to 300 K (room temperature) in increments of 20 K.

Figure 3.2b displays the PL spectrum at room temperature and the peak centers at E_{OG} = 1.48 ± 0.01 eV, in good agreement with the optical band gap measured in the absorption spectrum.

Figure 3.5a displays a series of temperature-dependent PL spectra in the range of 80-300 K. At temperature below 240 K, the main PL peak splits. Three Gaussian peaks are used to fit the PL

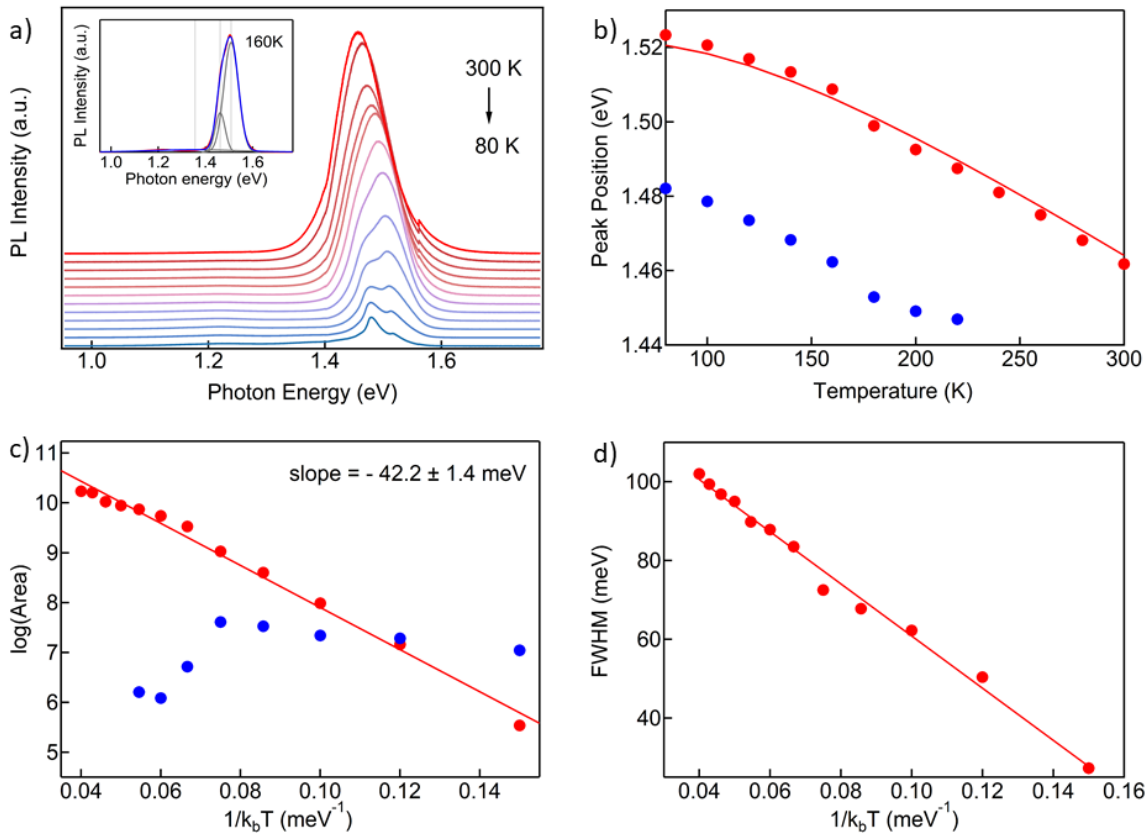

Figure 3.5 Temperature-dependent PL of $Re_6Se_8Cl_2$ in a) showing an increase in PL intensity with increasing temperature, suggesting an indirect bandgap. (Inset is the PL spectrum at 160 K fitted by three Gaussian peaks) b) Peak center position for primary and secondary peaks. c) Arrhenius plot for PL intensity and temperature. Red is for primary peak at higher energy, and blue is for secondary peak at lower energy. d) FWHM of primary peak versus temperature.

spectrum at each temperature. Among the three peaks, two peaks centered at 1.52 eV and 1.48 eV at 80 K are for primary and secondary PL emissions, and the other broad peak centered at 1.35 eV could be trap state emission (Inset in Figure 3.5a). At temperature 240 K and above, primary and secondary peaks are not separately resolvable due to peak broadening, and broad band emission is negligible, hence only one Gaussian peak is used to fit spectra.

Figure 3.5b shows that the primary and secondary peaks blue shift towards lower temperature, which is typical in semiconductors [99–101]. It mainly results from two mechanisms: lattice expansion and electron-phonon interactions. The temperature dependent band gap change can be described by Varshni empirical expression [99]:

$$E_g(\mathrm{T}) = E_0 - \frac{\alpha T^2}{T+\beta} \tag{3.8}$$

Where α and β are characteristic parameters of a material. The fitting curve (red) in Figure 3.5b gives α=6.83 x 10^{-4} eV/K, β= 674.4 K and E_0 =1.527 eV at zero temperature. Primary and secondary peaks have 40 meV difference which is consistent throughout the entire temperature range. We suspect that the secondary PL peak might be from bound excitons or trions, but additional experiments are required to verify the nature of the secondary peak.

In addition, the temperature-dependent PL spectra indicates that the bandgap of $Re_6Se_8Cl_2$ is indirect, which is confirmed by density functional theory (DFT) calculations. The PL intensity increases with increasing temperature over the broad temperature range of 80-300 K. The plot of PL intensity as a function of temperature confirms that PL emission is thermally activated with an activation energy of 42.2 ± 1.4 meV (Figure 3.5c). Full width at half maximum (FWHM) of the PL peaks is inversely proportional to the temperatures as well. This is consistent with a radiative recombination mechanism in an indirect-bandgap semiconductor where phonons provide the necessary momentum conservation. As temperature decreases PL intensity of primary peak decrease drastically. This trend indicates that $Re_6Se_8Cl_2$ is an indirect gap semiconductor.

In a semiconductor, photoexcited electrons in conduction band can recombine with holes in either radiative or nonradiative recombination process. For direct gap semiconductors, band-to-band transitions of electrons do not require phonon scattering and are temperature independent, while trap-mediated radiative recombination and nonradiative recombination process are slower at lower

temperature. As a result, PL intensity grows towards lower temperature. On the other hand, in indirect semiconductors, band-to-band transitions require phonon emission or absorption to conserve momentum, and their rates are proportional to phonon population hence heavily dependent on temperature. Since the decrease in radiation recombination rate is greater than that of non-radiative channels, PL intensity drops towards lower temperature. Quantitative analysis on recombination rates would require time-resolved photoluminescence spectroscopy with pump fluence dependence.

3.4 Electronic properties of thin layer $Re_6Se_8Cl_2$

3.4.1 STM on topological features

We characterize the structure of the 2D plane of $Re_6Se_8Cl_2$ using the Omicron scanning tunneling microscopy (STM) in an ultrahigh vacuum (base pressure < 4.0 x 10^{-10} mtorr). To prepare clean surfaces, samples were freshly cleaved in-situ by knocking off the Titanium post onto of the sample. Figure 3.6d shows the optical image of the cleaved surface and the inset is the prepared sample with post on it. Images were obtained in the constant-current mode with an electrochemically etched tungsten tip. To avoid tip artifacts, the STM tip was calibrated on a clean Au (111) surface before all measurements. Figure 3a shows an STM image at room temperature. The surface is ultra-flat with average roughness of only 0.4 Å; see also Figure 3.1d for a large area AFM image. The inset in Figure 3a shows a step height of 8.9 Å along the red line, in agreement with the monolayer thickness determined by SCXRD. A high-resolution STM image, Figure 3.6b, reveals that the topmost Cl atoms arrange in a rhombic lattice structure with lattice parameters of a = 6.5 ± 0.2 Å, b = 6.6 ± 0.2 Å and α =89°, respectively (Figure 3.6c), in good agreement with previous reports [94,102]. The tilt of the clusters is also noticeable in the STM image, as suggested

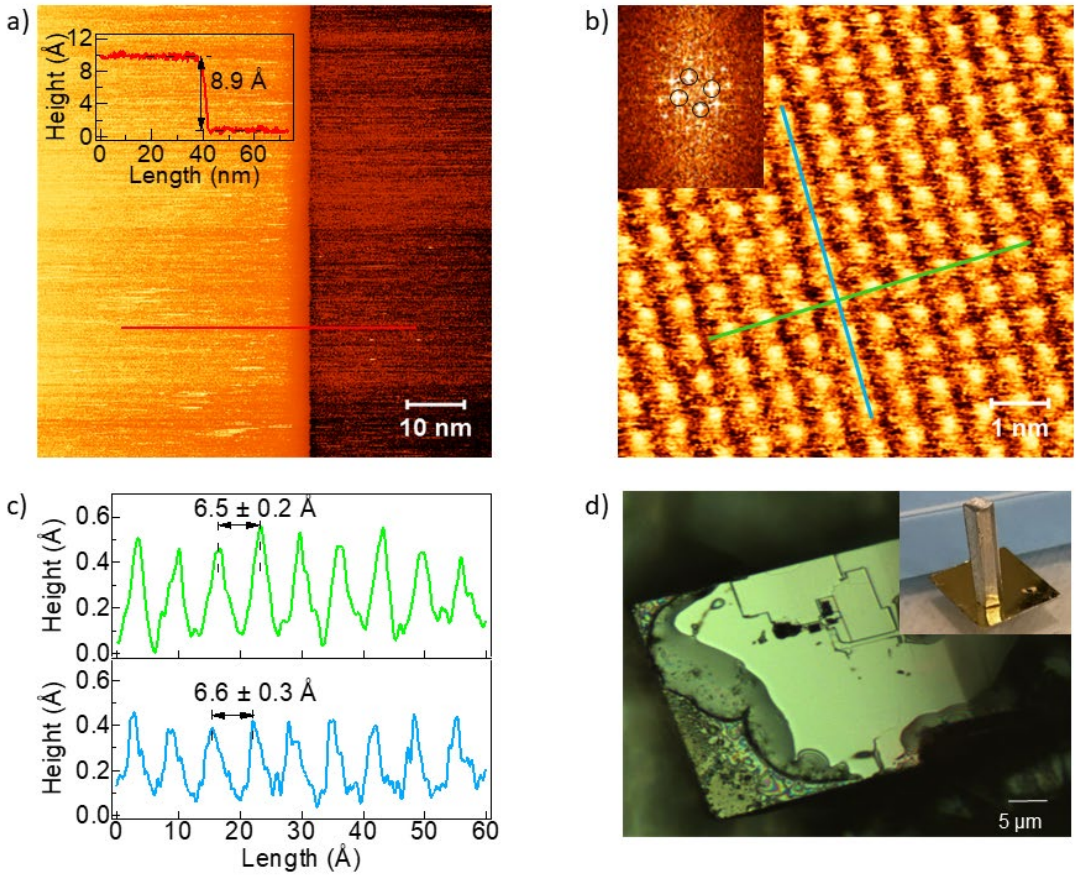

Figure 3.6 STM image on the in-plane structure of $Re_6Se_8Cl_2$. a) STM image at 292 K (80 x 80 nm, U = 1.0 V, I = 50 pA). The line profile in the insert shows a step height of 8.9 Å, consistent with the thickness of a monolayer. b) High-resolution STM image of $Re_6Se_8Cl_2$ at 292 K (8 x 8 nm, U = 0.6 V, I = 100 pA). The inset is the fast Fourier transform of the image. c) Line profiles along the green and blue cuts in (b). The average periodicity along the two directions is 6.5 ± 0.2 Å or 6.6 ± 0.3 Å, respectively. d) Optical image of the freshly cleaved sample surface. Inset is the prepared sample with a Titanium post on it.

by the apparent off-centered position of the Cl atoms. A Fourier transform of the image (inset in Figure 3.6b) identifies the pseudo-four-fold symmetry of the 2D lattice plane.

3.4.2 Electronic band gap determination

We determine the single-particle band structure by current-voltage (I-V) measurement in STS. The differential conductance (dI/dV) spectra were performed using a lock-in amplifier at an A.C modulation of 10 mV and at a frequency of 891.1 Hz. The corresponding current change was

acquired by keeping the tip fixed above the surface with the feedback loop off. Each I-V or dI/dV-V curve is an average over 100 curves under the same tunneling conditions.

Figure 3.7a displays I-V (blue) and dI/dV-V (red) curves acquired on a cleaved $Re_6Se_8Cl_2$ surface.

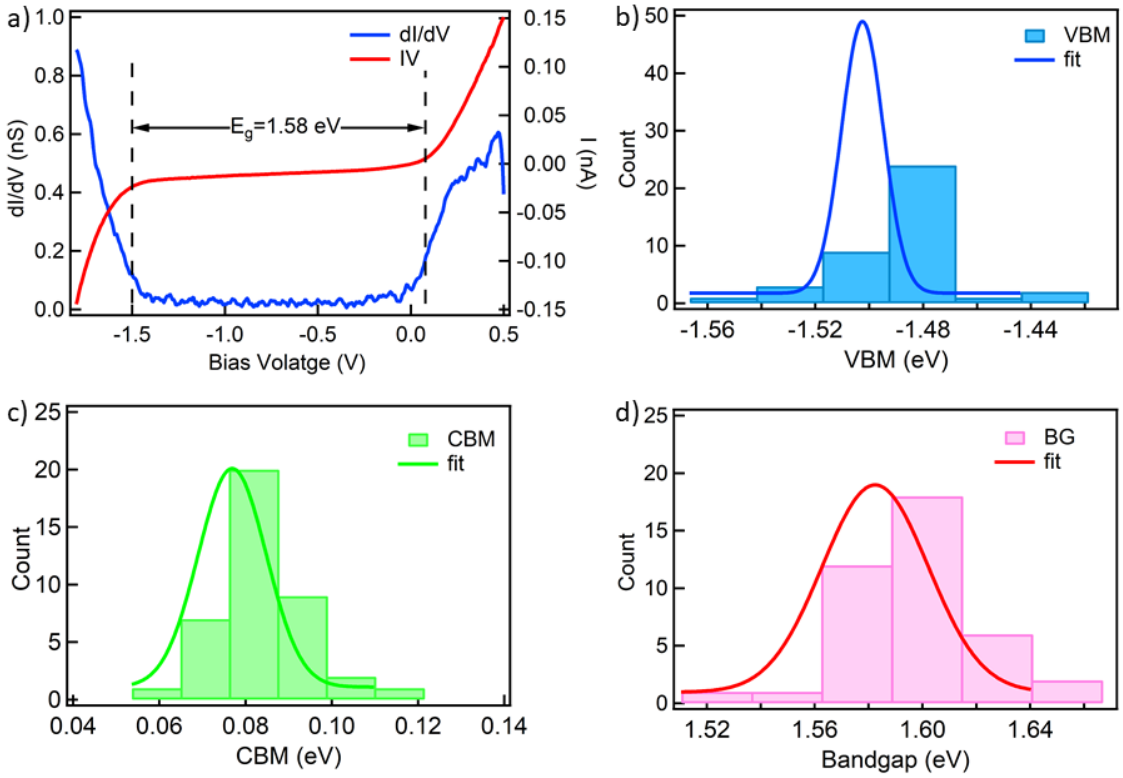

Figure 3.7 bandgap of $Re_6Se_8Cl_2$ from STS. a) STS spectrum with I-V curve in blue and the dI/dV-V curve in red. The VBM and CBM are designated by the black dashed lines, giving a bandgap of 1.58 eV. b-d) Statistics of VBM, CBM and Bandgap, respectively. Histogram of VBM, CBM, bandgap based on 40 averaged spectra at different spots. Solid curves represent the normal distribution fittings. It gives VBM = -1.50 ± 0.03 eV; CBM = 0.08 ± 0.01 eV; Bandgap =1.58 ± 0.03 eV (thermal broadening effect is not included).

The band edges are round due to thermal broadening effects at room temperature. Therefore, we determine the positions of the valence band maximum (VBM) and conduction band minimum (CBM) by taking the logarithm of dI/dV. The VBM is located at –1.50 V ± 0.03 V and the CBM at + 0.08 ± 0.01 V. We acquired 40 STS tunneling spectra on multiple samples and multiple spots with different tips. dI/dV spectra are consistent at the same tunneling conditions. Figure 3.7b-d

gives the statistical distributions of VBM, CBM and bandgap, respectively. These give the electronic bandgap $E_G = E_{CBM} - E_{VBM} = 1.58 \pm 0.03$ eV. This places E_F close to the CBM, implying that $Re_6Se_8Cl_2$ is an n-type semiconductor, in agreement with an early report based on electrochemistry [88].

We also performed the UPS measurement to study the valence band structure of the synthesized $Re_6Se_8Cl_2$. The conventional UPS with hν = 21.2 eV generated from the helium discharge lamp is

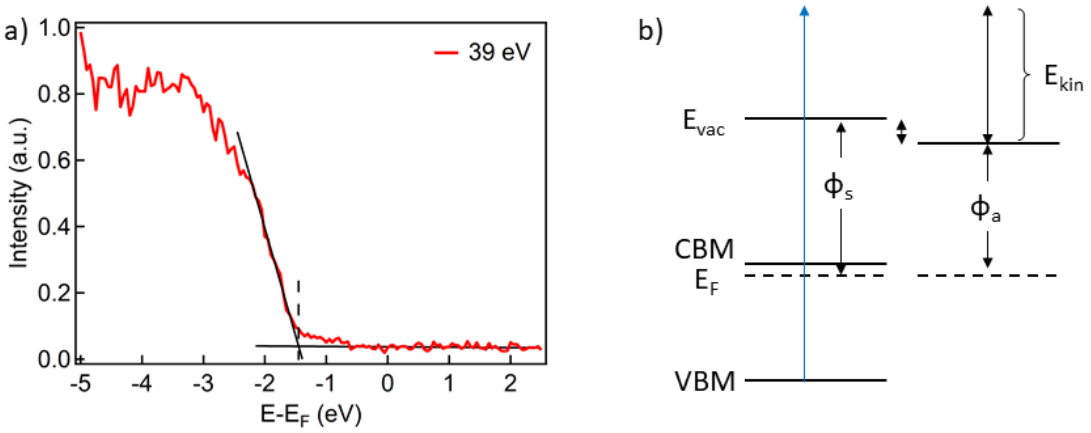

Figure 3.8 Photoelectron spectroscopy on $Re_6Se_8Cl_2$. a) Extreme ultraviolet photoemission spectrum (39 eV) of $Re_6Se_8Cl_2$ indicates the VBM at 1.45 eV below E_F. b) Band alignment of CBM, VBM referenced to E_F. The EUV pulse photoexcites electrons into vacuum. The measured kinetic energy is offset by the work function difference between the sample and the analyzer.

not suitable for this sample since the crystal size is smaller than the beam spot size. Therefore, extreme UV (39 eV) radiation were used as the pump pulses to photoexcite the crystals at room temperature. Freshly cleaved samples were transferred into an ultrahigh vacuum chamber (~10−10 Torr) where it was further annealed at 200 °C for 4 h.

The XUV radiation (39 eV) for photoemission was obtained from high harmonic generation in Ar, with a commercial ultrafast extreme UV source (KMLabs, XUUS) pumped by the fundamental laser output from a Ti:Sapphire amplifier (KMLabs, Wyvern, 5W, 40 fs, 10 kHz). The 25th

harmonic output at 39 eV was selected with a grating downstream and applied for UPS measurements. The XUV radiation was focused to a spot size of ~150 μm with a spectral width of approximately 500 meV. The kinetic energy of the photoemitted electrons were measured using a hemispherical electron energy analyzer equipped with a 2D delay line detector (SPECS Phoibos-100), as described in section 2.2.4. The work function of the analyzer is calibrated on the well-known single crystal Ag (111) surface. Hence, the measured kinetic energy can be converted to energy referenced to the Fermi level, and the schematic is shown in Figure 3.8b.

The valence band structure is mapped out in Figure 3.8a, the onset of which gives a valence band maximum (VBM) at $E_{VBM} = 1.45 \pm 0.01$ eV below the E_F. This places E_F close to the conduction band minimum (CBM), implying that $Re_6Se_8Cl_2$ is an n-type semiconductor as well, in agreement with our STS measurements discussed above.

3.4.3 DFT Band structure calculations

As discussed in section 3.3.3, the temperature dependent PL measurements indicate that $Re_6Se_8Cl_2$ is an indirect bandgap semiconductor, which can be confirmed by density functional theory (DFT) calculations. We calculate the band structure of $Re_6Se_8Cl_2$ on the experimental geometry by using the Perdew-Burke-Ernzherof (PBE) functional [103], and refine the calculation with the hybrid Heyd-Scuseria-Ernzerhof (HSE06) exchange correlation functional [104], both including spin-orbit coupling (SOC). Figure 3.9a shows the band structure of the bulk crystal with PBE-SOC (black curves) and HSE06-SOC refinements at selected high-symmetry k points (blue dots). The HSE06-SOC band structure gives an indirect bandgap of $E_G = 1.49$ eV between the VBM at Γ (0, 0, 0) and the CBM at T (0, 0.5, 0.5). Compared to the results at the PBE-SOC level, HSE06-SOC mainly affects the valence band, down-shifting the VBM energy by ~0.4 eV with respect to that calculated with PBE-SOC. It has limited effects on the conduction band. The computational results

support the observed indirect bandgap and are in nearly quantitative agreement with the measured bandgap of 1.58 eV from STS. Moreover, the bandwidths of VB and CB are pretty narrow (≤ 0.5 eV in Figure 3.8a) mainly due to the limited inter-cluster electronic coupling within each layer. It is expected to be highly sensitive to phonon modes arising from the collective motions of the "superatomic" units. Strong coherent phonon vibrations have been detected in the $Re_6Se_8Cl_2$ system with below bandgap and near bandgap excitations, as seen in other semiconductors [105–108].

Figure 3.9b shows DFT band structure calculations on monolayer $Re_6Se_8Cl_2$ as comparison. The monolayer $Re_6Se_8Cl_2$ keeps the indirect bandgap property with the VBM located at the Γ (0,0,0) point, and CBM at the Y (0,0.5,0) point in the momentum space. In addition, down to the monolayer limits, quantum confinement leads to an increase of the band gap to a value of 1.72 eV

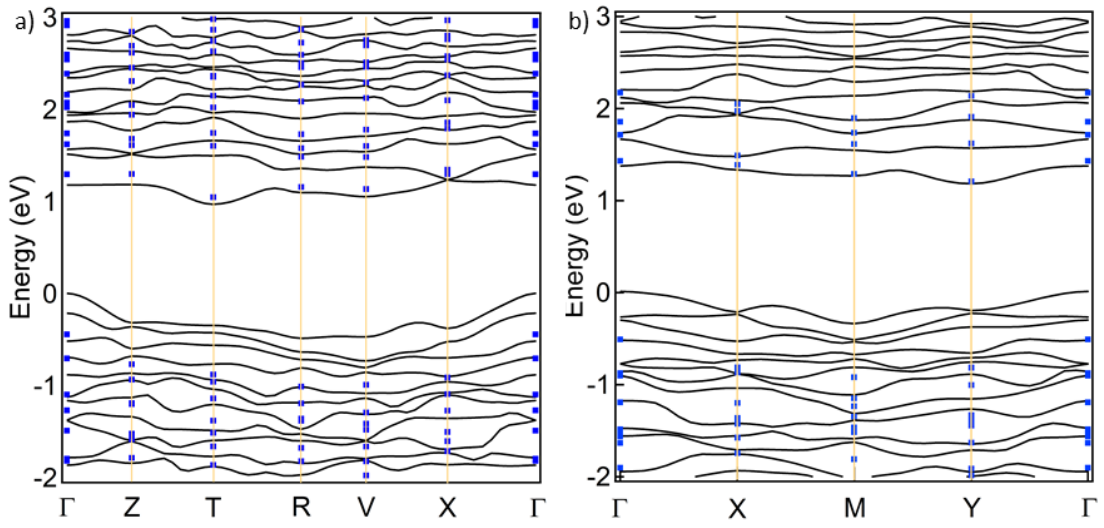

Figure 3.9 DFT calculated band structure with PBE-SOC (solid black line) and HSE06-SOC (blue dots). a) band structure of 3D bulk crystal. b) band structure of 2D sheets.

at the HSE06-SOC level, higher than the 1.49 eV band gap of the 3D bulk. The hybrid exchange correlation has similar effects on the CB and VB compared to that on the bulk band structure.

3.4.4 2PPE measurements

The TR-2PPE experiments were carried out by using pump ($h\nu_1$= 1.85 eV) and probe ($h\nu_2$= 4.45 eV) laser pulses from the home-built NOPA system described in section 2.2.3. The pump and probe pulses with a time delay (Δt) were colinearly aligned and focused on the sample surface at 45° to normal. Both pump and probe are p-polarized. Electrons are photoexcited into the conduction band by the IR pump $h\nu_1$ and subsequently ionized by the UV probe at various time delays (Δt).

Figure 3.10a displays a 2D pseudo color plot of the TR-2PPE spectra as a function of electron energy referenced to E_F and pump–probe delay Δt for $Re_6Se_8Cl_2$. We observe two main features in the spectra. 1) electrons distribute in a broad energetic range (1.2 – 2.0 eV) and the energy range is higher than expected. 2) electron energy decreases with the loss of high energy tail within $\Delta t <$ 0.5 ps. With the absorption of one pump photon $h\nu_1$, electrons are excited into the conduction band with excess energies of $h\nu_1$-E_g = 0.37 eV, where E_g is the indirect bandgap measured in STS. These electrons have energy of ~ 0.5 eV above the Fermi level, which are indistinguishable in the spectra due to the signals from the secondary scattering electrons. Instead, we observe a broad peak at high energy range. Figure 3.10c displays electron energy distribution curves at various pump–probe delay time (Δt = 0– 600 fs). The broad peak can be explained by the many phonon-assisted indirect band-to-band transitions since $Re_6Se_8Cl_2$ is an indirect band gap material, as shown in section 3.3.1. Peak position is centered at 1.59 eV at Δt =0, which is much higher than the conduction band minimum. The origin of this peak is still unclear. One reason could be the coherent two-photo absorption through some intermediate states. To prove it, pump energy dependent measurements and power dependent measurements are needed. The second observation of the electron energy decrease with delay time is demonstrated in Figure 3.10c. After

photoexcitation, electrons equilibrate through electron–electron scattering and give a quasi-thermal distribution of hot electrons. This process happens on the ultrashort time scale within 100 fs, which is not resolved with our experiment time resolution. After 100 fs, the photoexcitation

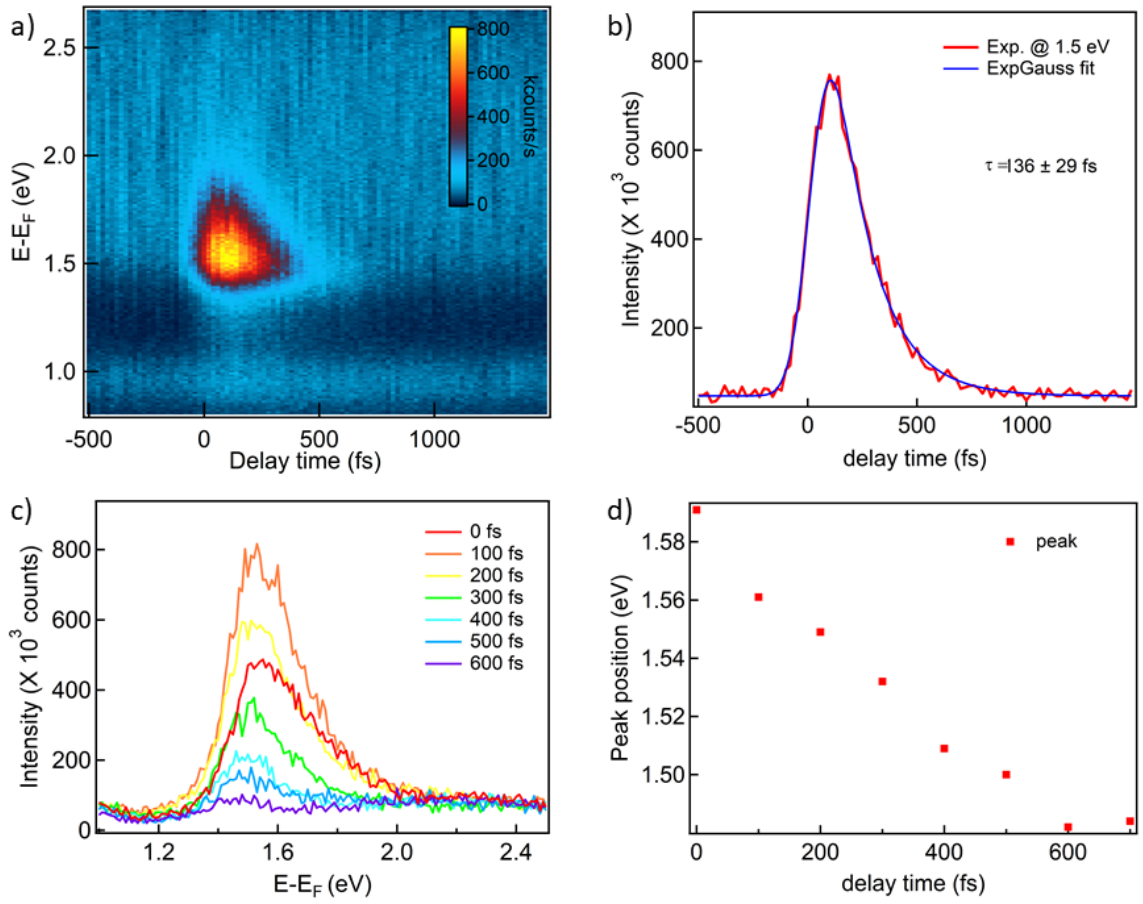

Figure 3.10 2PPE spectra on $Re_6Se_8Cl_2$. a) 2D plot of TR-2PPE spectra as a function of electron energy reference to E_F and pump–probe delay for $Re_6Se_8Cl_2$. Color bar represents the intensity of electron counts. b) a horizontal cut of Figure 3.10a at E = 1.5 eV, representing the photoemission intensity change as a function of delay time(red). It is fitted well with the convolution of Gaussian function and exponential decay function (blue). c) electron energy distribution curves at various pump–probe delay time (Δt = 0– 600 fs) d) Peak position of each energy distribution curve obtained by simple Gauss fittings as a function of delay time.

intensity decreases with a downward shift of the energy peak position (Figure 3.8a) and a high energy tail shown in Figure 3.10a. This can be explained by hot electron cooling through electron phonon scattering. Figure 3.10b shows a horizontal cut of Figure 3.10a at E = 1.5 eV, which

represents the temporal change of the photoemission intensity (red curve). It can be described as the convolution of the cross-correlation of the pump and probe pulses (Gaussian function) and the single exponential decay of hot electrons, which gives the decay time $\tau = 136 \pm 29$ fs. Since the conduction band minimum locates at T (0, 0.5, 0.5), electrons will relax into bands with large parallel momentums that extend the maximum parallel momentum the probe energy $h\nu_2$ can reach to. Hence, signals drop back to zero after 700 fs. To study the electron relaxation dynamics in a longer timescale or in a wider momentum space, high harmonic generated pulses are demanded.

3.5 Excitonic effects in thin layer $Re_6Se_8Cl_2$

In semiconductors, an electron is excited into the conduction band with photon absorption and leaves a hole in the valence band. The electron (e) and hole (h) are usually bound together by the Coulomb interaction, forming a quasiparticle. The bound state of this quasiparticle is called an exciton [98]. Excitons can transport energy in the materials without transporting net electric charge. There are two main limiting types of excitons: Mott–Wannier excitons and Frenkel excitons. Mott-Wannier excitons are typically found in semiconductors with large dielectric constants, such as

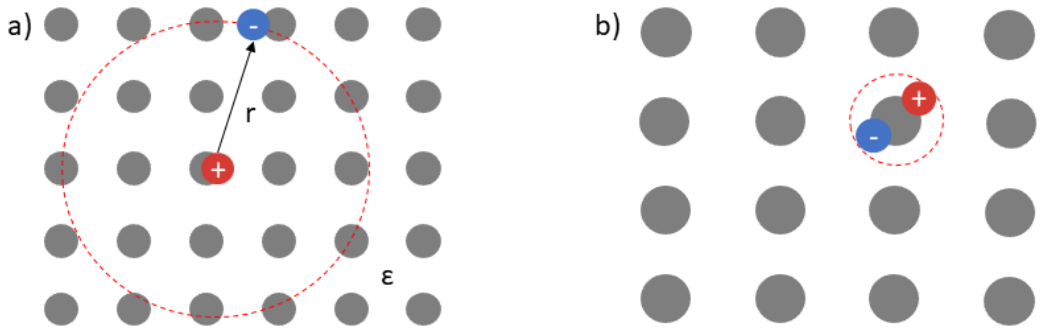

Figure 3.11 Mott–Wannier excitons and Frenkel excitons a) Mott–Wannier excitons which can be treated as hydrogen-like quasiparticles with radius r in a dielectric medium (b) Frenkel exciton which is localized at a single lattice site.

inorganic semiconducting Si and GaAs. The large dielectric constants result in relatively strong screening and reduce the Coulomb interactions between an electron and a hole. Mott-Wannier exciton can be treated as a hydrogen-like particle, the energy states of which can be derived by solving the Schrödinger equation using the effective mass approximations. The exciton binding energy is on the order of 10 meV, which is comparably small. The relative motion of the electron and hole pairs, namely the exciton Bohr radius, is much larger than the lattice spacing. Frenkel excitons are typically found in solids with a relatively small dielectric constant, such as alkali halide crystals (NaCl) and organic molecules. The Coulomb interactions between an electron and a hole are strong so that the electron and hole are confined within the unit cell or even on the same lattice site. The exciton binding energy is on the order of 0.1 to 1.0 eV. Frenkel exciton cannot be derived using the effective mass approximation described below due to the strong localization of the electron on the lattice, similarly to a bound electron to an ion. Since $Re_6Se_8Cl_2$ is an inorganic semiconductor, we expect to see Mott-Wannier excitons in this system. Therefore, we focus more on this type of exciton in the following.

This two-body system can be treated as a hydrogen-like particle and gives the exciton dispersion relation described as:

$$E_{ex}(n_B, \boldsymbol{K}) = E_g - \frac{R_y^*}{n_B^2} + \frac{\hbar^2 \boldsymbol{K}^2}{2M} \tag{3.9}$$

where E_g is the band gap energy. The second term $-\frac{R_y^*}{n_B^2}$ is the energy due to the relative motion of the e-h pair. It gives a series of states determined by the principal quantum number n_B, the value of which is 1,2,3…. The exciton Rydberg energy R_y^* is modified from the ionization energy of the hydrogen atom by the dielectric constant of the medium (ε) and the effective mass of the electron (m_e) and hole (m_h) and described as:

$$R_y^* = \frac{\mu e^4}{2(4\pi\epsilon)^2\hbar^2} = 13.6eV\frac{\mu}{m_0}\frac{1}{\varepsilon^2} \tag{3.10}$$

with reduced mass

$$\mu = \frac{m_e m_h}{m_e + m_h} \tag{3.11}$$

Similarly, we can derive the excitonic Bohr radius as

$$a_B^{ex} = \frac{4\pi\epsilon\hbar^2}{\mu e^2} = 0.53\text{Å}\frac{\varepsilon m_0}{\mu} \tag{3.12}$$

The radius of the exciton is also modified by the dielectric constant and reduced exciton mass.

The third term $\frac{\hbar^2 \boldsymbol{K}^2}{2M}$ is the energy due to the center-of-mass motion, which involves the total wave vector of the exciton **K** and the translational mass M. It implies that the curvature of the exciton dispersion is determined by the translational mass rather than the electron mass. Hence, the exciton dispersion is not necessary to follow the electronic band structure dispersion, as seen in Figure 3.11. The energy difference between the electronic bandgap and the lowest exciton energy is called exciton binding energy E_B, which ideally equals to R_y^*.

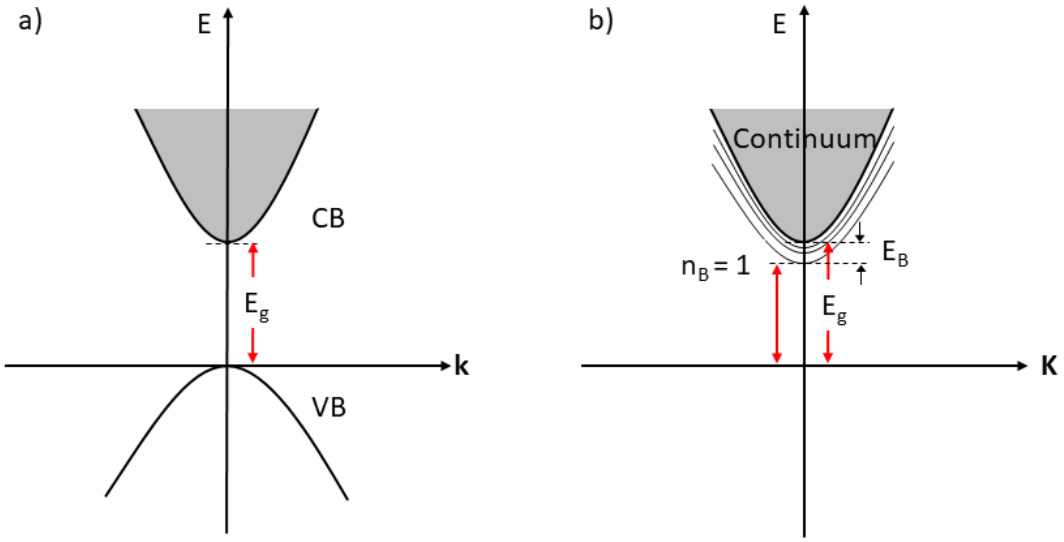

Figure 3.11 Exciton energy states in K space. a) Energy states of valence band and conduction band as a function of wave vector k. b) Exciton energy states as a function of wave vector K for the center-of-mass motion.

In direct bandgap semiconductors, optical band-to-band transition gives the electron and hole the same wave vector **k**, hence, we can assume **K** = 0. The energy states of exciton are a series of discrete states centered at **K** = 0. Exciton peaks at low quantum numbers typically n_B=1 or 2 are observable in the optical absorption or reflectance spectra in many direct semiconductors e.g. GaAs [49], Cu2O [109], monolayer TMDCs [11]. Features are more distinct at low temperatures due to less phonon scatterings. In indirect bandgap semiconductors, the electron and hole locate at different k points, excitons are generated in a phonon-assisted process. **K** wave vector can take any arbitrary values due to the momentum exchange between the indirect exciton and the phonon. Therefore, the optical absorption (or absorption coefficient α) as a function of photon energy does not exhibit discrete peaks or lines but a continuum spectrum.

Moreover, the dimensionality plays an important role in the exciton binding energy. By taking both quantum effects and screening effects into account, the exciton energy dispersion Eq. 3.9 can be rewritten as:

$$E_{ex}^{2D}(n_B, \boldsymbol{K}) = E_g + E_Q - \frac{R_y^*}{(n_B - \frac{1}{2})^2} + \frac{\hbar^2 \boldsymbol{K}^2}{2M} \tag{3.13}$$

where E_Q is the quantization energies of electrons and holes. n_B is replaced by (n_B-1/2) from 3D to 2D and thus the binding energy in 2D systems is four times larger than that in 3D. Although the motion of electrons and holes is quantized in one direction i.e. z direction in 2D systems, the width l_z has a non-zero value. The value of the 2D exciton binding energy E_{ex}^{2D} varies with the width l_z and the variations depends on the material parameters. For example, in AlGaAs/GaAs quantum wells, E_{ex}^{2D} can reach to $4R_y^*$ with an infinite barrier at width $l_z = 0$, while E_B is about 2-3 times R_y^* with a finite barrier even at the maximum point [110].

3.5.1 Experimental exciton binding energy

Let us recall that the absorption spectra and photoluminescence give the optical bandgap E_{OG} = 1.48 ± 0.01 eV and STS gives the electronic bandgap E_G = 1.58 ± 0.03 eV, as described in section 3.3.1 and section 3.4.1, respectively. The deviation is mainly due to the energy resolution limit as well as the thermal broadening effects at room temperature. Based on these results, we calculate an exciton binding energy of $E_B = E_G - E_{OG}$ = 100 ± 40 meV, which is one order of magnitude larger than typical values in conventional 3D semiconductors (e.g., 10 meV for Si, 2.7 meV for Ge) [48,49] but comparable to that in a typical van der Waals layered semiconductor such as MoS_2. The weak interlayer coupling in the bulk MoS_2 suggests it a quasi-2D material, in which the electronic density of states and the exciton exhibit quasi 2D characters [50,111].

3.5.2 3D and 2D E_B calculation using simple Bohr model

To put the measured E_B = 100 ± 40 meV value in perspective, we calculate the exciton binding energies based on a 3D or a 2D Bohr model [52]. We use the effective electron and hole masses (m_e^* and m_h^*, respectively) from the PBE-SOC band structure (Figure 3.9a) in high symmetry directions: $m_h^* = 0.66\, m_e$ (in the Γ-V or Γ-X direction) and $m_e^* = 1.15\, m_e$ (in the T-V or T-X direction); m_e is the free electron mass. It gives the exciton reduced mass $\mu = 1/(m_h^{*-1} + m_e^{*-1})$ = 0.42 m_e. The dielectric constant ε_r^* has parallel ($\varepsilon_\parallel^*$) and perpendicular ($\varepsilon_\perp^*$) components, the values of which depend on the light polarization relative to **c** axis of $Re_6Se_8Cl_2$ crystal. The reflectance measurement gives $\varepsilon_\perp^* \sim 10.5$ at ~ 1.5 eV, as described in section 3.3.2. $\varepsilon_\parallel^*$ is not obtained from experiments but a theoretical result, which equals to 10.6. we thus deduce the effective dielectric constant

$$\varepsilon_r^* = \sqrt{\varepsilon_\parallel^* \varepsilon_\perp^*} = 10.5 \tag{3.14}$$

We calculate exciton binding energies $E_B^{3D} = \frac{R_y^*}{n_B^2} = 50$ meV in 3D and $E_B^{2D} = \frac{R_y^*}{(n_B - \frac{1}{2})^2} = 200$ meV in 2D according to Eq. 3.10 and Eq. 3.13 respectively, where $n_B = 1$ for the ground excitonic state. The experimental binding energy $E_B = 100 \pm 40$ meV is between these two limiting values and suggests a partial 2D nature of excitons in $Re_6Se_8Cl_2$, as expected from a 2D layered van der Waals structure with weak interlayer electronic coupling. The effective Bohr radius is approximately 13.3 Å according to Eq. 3.12, which is twice of the lattice constant in the ab plane of the crystal.

Although the excitons in bulk $Re_6Se_8Cl_2$ behaves as 2D excitons, the monolayer case would still be different due to the changes of the dielectric environment and the effective masses. In the real 2D, the monolayer can be treated as sandwiched between the vacuum or air layers with dielectric constant of 1.0 rather than the $Re_6Se_8Cl_2$ layer with $\varepsilon_r^* = 10.5$. It results in reduced $\varepsilon_\parallel^*$ and lower dielectric constant ε_r^{2D}. The effective mass of electrons and holes is heavier than those in the bulk. Thus, the exciton binding energy in monolayer $Re_6Se_8Cl_2$ is expected to be much higher than that in the bulk.

3.6 Structural defects characterizations

Structural defects, including point defects, edges and grain boundaries, are induced in the sample during the crystal growth or mechanical exfoliation processes. It is found that these defects have significant influence on the optical, electronic, mechanical and electrical transport properties of the materials. For example, the charge carrier mobility in electrical transport measurements is much lower in MoS_2 single layers with a high defects concentration [112]. Grain boundaries in graphene can either strengthen or weaken the mechanical strength due to different arrangements [113]. On the other hand, structural defects modified the local properties which opens a door for studies on novel physical phenomenon. For example, ferromagnetism has been observed at defect

structures in highly oriented pyrolytic graphite (HOPG), which is originated from the localized electron states at grain boundaries [114]. Therefore, experimentally characterizing the atomic and electronic properties of the defects combined with theoretical understanding the impacts of these defects are significantly important.

3.6.1 STM/STS on surface point defects

We characterize the atomic structures of defects on the surface of $Re_6Se_8Cl_2$ by STM at room temperature. Figure 3.13a shows a STM image with defects appearing as dark spots at positive

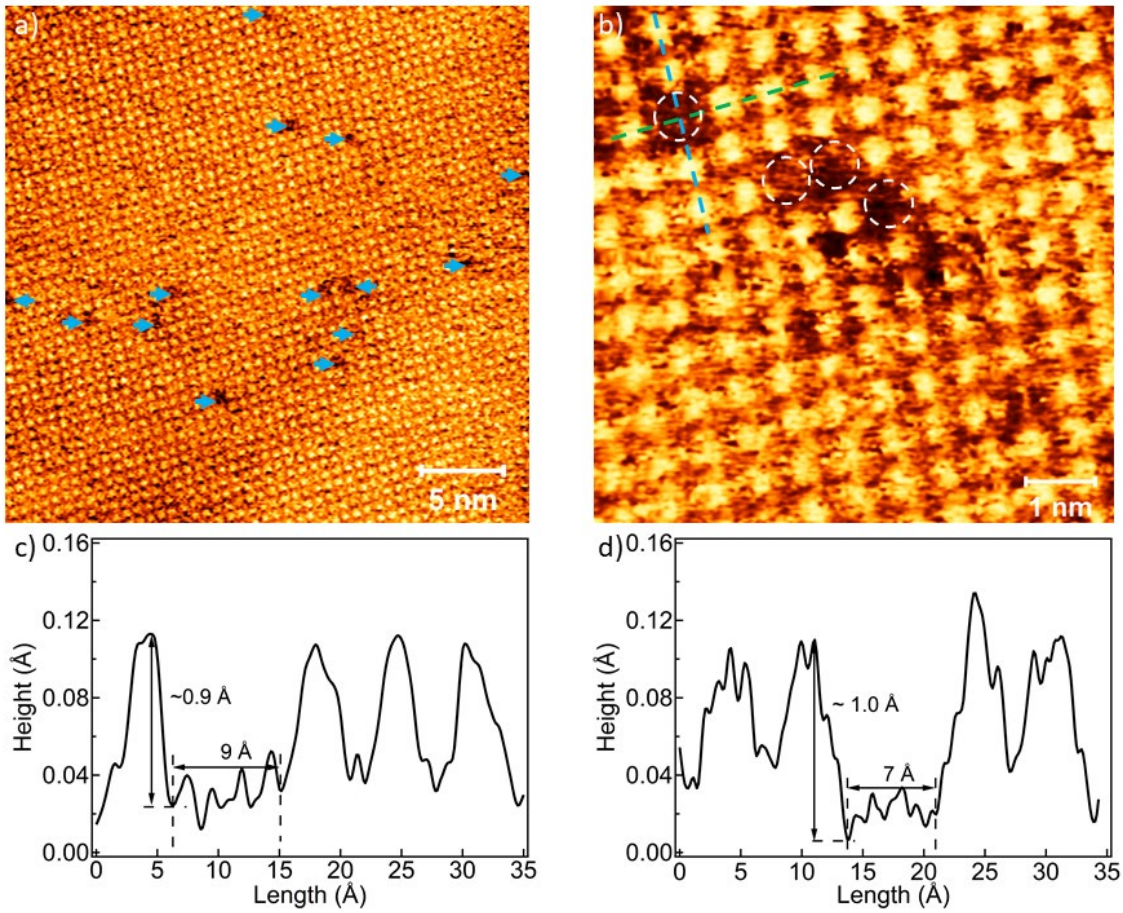

Figure 3.13 Defects on the $Re_6Se_8Cl_2$ surface. a) STM image of a $Re_6Se_8Cl_2$ surface showing point defects marked by the blue arrows (32 x 32 nm, U = 0.6 V, I = 100 pA). b) a high-resolution image containing point defects marked by white circles (7.5 x 7.5 nm, U=0.6 V, I= 100 pA). c) d) line profiles across the individual defect along the green and blue dashed lines in a), respectively.

bias voltage (marked by blue arrows). The density of surface defects is ~1.5%, as determined by STM. An atomic resolution image is shown in Figure 3.13b. The line profiles along the lattice directions (green and blue dashed lines) give the apparent depth and width about 1.0 Å and 8 Å, respectively, consistent with surface Cl vacancies (Figure 3.13cd). The loss of an electronegative atom from a polar semiconductor is expected to result in n-doping, as is also known for S vacancies in MoS_2 [115–117].

To characterize the effects of these surface defects on the electronic structures, STS spectra were collected on top of the defects. It reveals a mid-gap peak at ~0.67 eV below E_F (~ 0.83 eV above VBM), as shown in Figure 3.14b. DFT calculations on the Cl defective system in a $2 \times 2 \times 2$ supercell (bulk system) and in a 2×2 supercell (2D sheet) were performed to investigate the nature of the defects. In the DFT calculations, geometry relaxations were performed by using the Perdew-Burke-Ernzherof (PBE) exchange correlation functional [103], plane waves basis set and ultrasoft pseudopotentials. The electronic structures were then refined by using the hybrid HSE06 exchange correlation functional [118] including the spin-orbit interactions. It is the same as the procedure we used for the intrinsic band structures of $Re_6Se_8Cl_2$ crystals. The calculated projected density of states (PDOS) shows a distinct localized Kohn-Sham (KS) state in the middle of the bandgap in both bulk and 2D systems(Figure3.14cd). In the 3D bulk, this KS states locates at 0.88 eV above the valance band in a calculated bandgap of 1.49 eV. While in 2D sheets, this KS states locates at 0.94 eV above valance band in a larger bandgap of 1.72 eV, as mentioned in section 3.4.3. The peak positions in both 3D bulk and 2D sheets are consistent with mid-gap states appeared in the STS spectra, confirming that these defects are Cl vacancies. This mid-gap defect state is associated

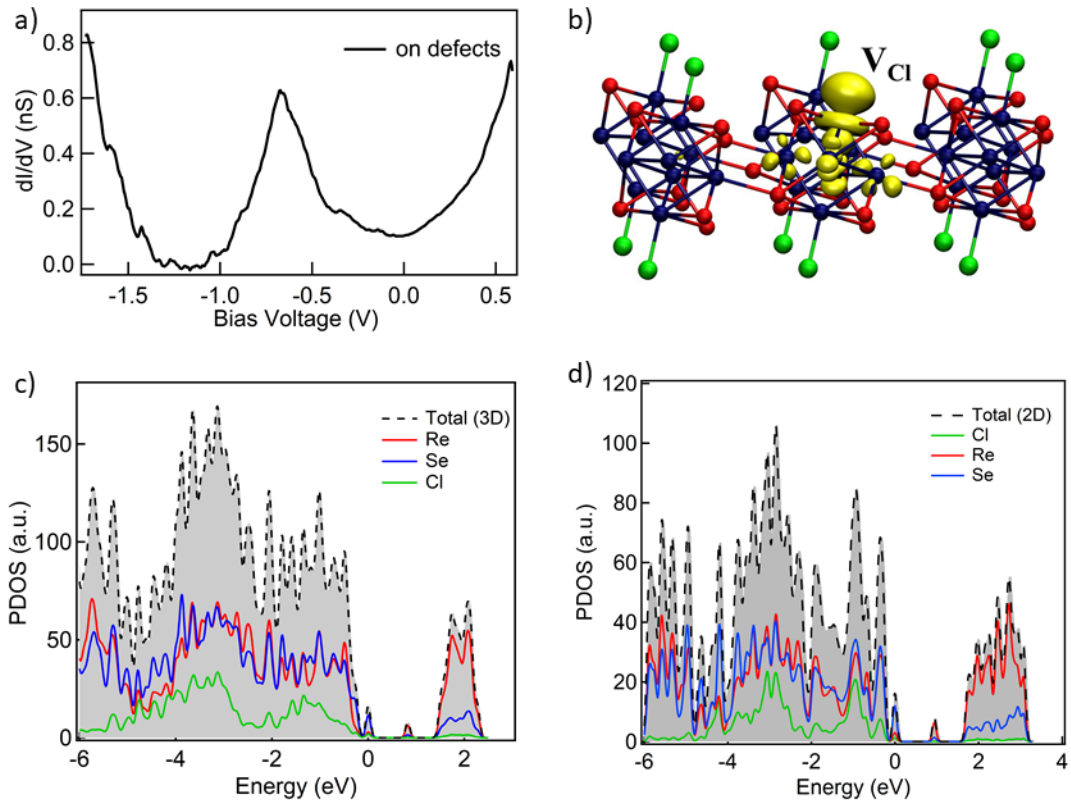

Figure 3.14 Defect induced mid-gap states. a) dI/dV spectrum collected on top of the defects showing a mid-gap state at –0.67 V. b) Real space plot of the HOMO of a single neutral on the 2D sheet, indicating the localization of unpaired electron on the Re site. c) d) PDOS of the bulk $Re_6Se_8Cl_2$ and 2D sheet with neutral Cl vacancies, respectively, as calculated using HSE06-SOC.

with the unpaired electron on the Re atom, as illustrated in the real space plot of the highest molecular orbital (HOMO) of the neutral Cl vacancy on the 2D sheet in Figure 3.14b.

3.6.2 STM/STS on step edges

To characterize the influence of the interfaces on the electronic structures, STM/STS were carried out on the freshly cleaved $Re_6Se_8Cl_2$ crystals at room temperature. Multiply layers are introduced in the system due to the mechanical exfoliation and visualized in the STM images, as shown in Figure 3.15a (large scale image in Figure 3.6a in section 3.4.1). The height difference in the line

profile across two layers in Figure 3.15b indicates a single layer step edge. The width of the step edge is ~ 2.2 nm with starting point at X = 5.4 nm on the bottom layer and ending point at X = 7.6 nm on the top layer. STS map was performed along the solid line in Figure 3.15a with total length of 12.8 nm. Spectra were taken at every 0.2 nm interval. Figure 3.15c is a color rendering of the real space imaging of the band profile across the step edge and Figure 3.15d shows the selected individual spectra at various locations.

The numbers on the spectra represent the distance between the spot site and the left edge of the image, with 6.4 nm at the center of the step edge (marked in Figure 3.15a).

Apparently, band bending for conduction band and valence band appears on both sides of the step edge. The traces marked by the dashed curves seem to have mirror symmetry, indicating the same effects on the top and bottom layers. The bands bend upward above 200 meV over 2 nm on each side toward the step edge (depletion length). As we can see, band structures are the same at spots far from the step edge on both layers (spectra at 3.8 nm, 4.8 nm, 8.0 nm, 8.8 nm), which gives VBM = 1.50 eV and CBM =0.08 eV, as shown in section 3.4.2. While the spot gets closer to the step edge, both VBM and CBM move upward. Spectral line shape for the conduction band remains almost the same and the variation in spectra at 5.8 nm, 6.8 nm and 7.0 nm happens randomly which are not seen in other STS maps. While the spectra on the valence band shift dramatically. LDOS (dI/dV intensity) increases at the same bias when the spectrum spot moves toward the center of the step edge. Moreover, new features appear in the valence band and are observable in spectra at 5.8 nm, 6.2 nm, 6.4 nm and 6.6 nm. A shape peak centered at 1.56 eV dominates the valence band in spectrum at 6.4 nm and a shape peak centered at 1.70 eV also shows up in spectrum at 6.6 nm. In other spectra, the new features may be merged with the bulk states and become invisible.

One possible reason for the band bending is Fermi level pinning by the edge states or called interface states. The dangling bonds at the step edge (termination of the top layer) introduce the edge states within the bandgap, which is common in semiconductor interfaces such as TMDCs heterostructures [119] and monolayer TMDCs/graphene systems [120,121]. The edge states generally depends on the step structure or termination configurations [122] which is not yet

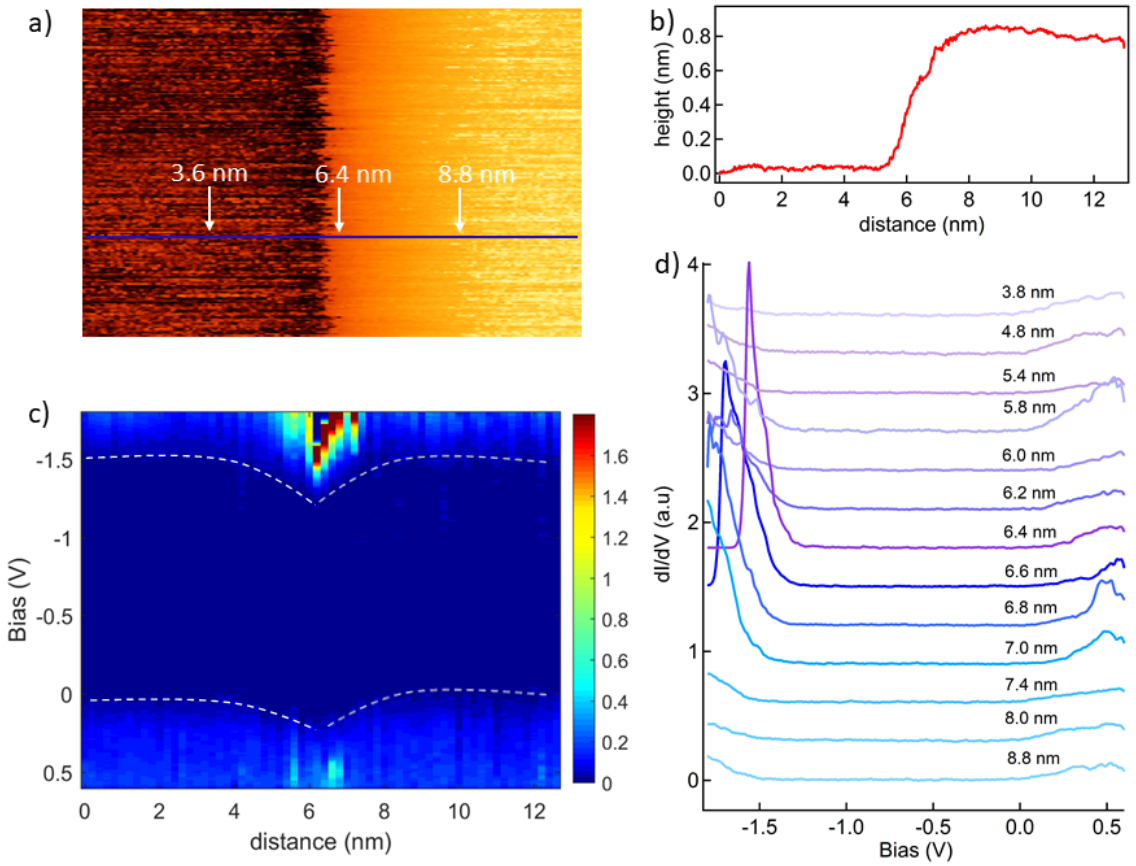

Figure 3.15 Edge states determined by STS. a) STM image containing a single layer step edge. (length is 12.8 nm, U =0.6 V, I=100 nA). b) line profile along the blue line in a), showing the width the step is ~ 2.0 nm. c) a color rendering of the real space imaging of the band profile in terms of dI/dV. d) selected individual spectra at various locations.

resolved in our experiments.

3.7 Conclusions

The results presented above establish Chevrel-type $Re_6Se_8Cl_2$ as the first member of the 2D hierarchical semiconductor family. The strong in-plane covalent bonding and the weak interlayer van der Waals interactions favor the formation of quasi-2D characters in the bulk crystal, the exciton of which exhibits partially 2D nature with exciton binding energy as large as 100 meV. An obvious research direction is to optimize the exfoliation method to reach the monolayer limit. It is realized in a chemical intercalation followed by liquid exfoliation process and produces micrometer-sized nanosheets [47]. It is intriguing to study the excitonic effects in this real 2D hierarchical system. Moreover, compared to other 2D materials, the unique complex structure of $Re_6Se_8Cl_2$, whose structure is built from superatomic building blocks instead of simply atoms, offers stimulating prospects for designing multiple functions and novel properties.

Chapter 4

In-plane Isotropy in Superatomic Semiconducting $Mo_6S_3Br_6$

4.1 Introduction

Two-dimensional (2D) van der Waals materials with in-plane anisotropy are of interest for directional transport of charge and energy. One prominent example is black phosphorus, which has been shown to host highly anisotropic excitons and theoretically predicted to exhibit elliptic and hyperbolic dispersions for plasmon polaritons [54–56]. Likewise, in-plane anisotropy has been demonstrated to yield ultra-low-loss phonon polaritons in α-MoO_3 [58] and has been explored to fabricate unique photodetectors and field-effect transistors [123] in rhenium dichalcogenides [124,125]. When compared to traditional 2D materials, there are very few examples of layered cluster-based structures [126–128] that can be exfoliated, and the existing ones typically have isotropic in-plane structures (e.g., $Re_6Se_8Cl_2$). The structural diversity of 2D materials with in-plane anisotropy is limited, which has restricted their use.

Here, we investigate $Mo_6S_3Br_6$, a quasi-2D material with strong in-plane structural anisotropy derived from the Chevrel phase in which [Mo_6] octahedral cluster subunits are covalently linked into layers. Bulk $Mo_6S_3Br_6$ was first reported in 1983 by Perrin and coworkers [42], but its physical properties are essentially unknown, especially how the structural anisotropy affects the electronic and optical properties in the plane. Moreover, it has never been investigated as a mono- or few-layer materials either experimentally or theoretically.

4.2 Sample preparation and characterizations

4.2.1 Crystal synthesis

$Mo_6S_3Br_6$ was prepared in the following procedure, modified from Perrin et. al [42]. A stoichiometric mixture of Mo_6Br_{12} [129] (200 mg, 0.13 mmol), S (25 mg, 0.78 mmol), Mo (70 mg, 0.73 mmol) and Nb (6 mg, 0.06 mmol) was ground with a mortar and pestle in an inert atmosphere, pressed into a pellet and sealed in a quartz tube under vacuum. The tube was then heated to 1175 ℃ in a box furnace with a ramp rate of 1 ℃/min, held for 72 hours at the reaction temperature, and finally cooled to room temperature at a ramp of 0.5 ℃/min. Millimeter size crystals of $Mo_6S_3Br_6$ are deposited in the cooler region of the tube. Remarkably, millimeter-size single crystals (shown in Figure 4.1b) are obtained when a mixture of Mo and Nb (in a molar ratio of 92.5:7.5) is used instead of the pure Mo metal. In addition to microcrystalline $Mo_6S_3Br_6$ powder and macroscopic crystals, the tube contains a few crystals of $NbBr_5$, which form in-situ and presumably acts as a chemical vapor transport agent that allow large $Mo_6S_3Br_6$ crystals to grow. The flattened needle

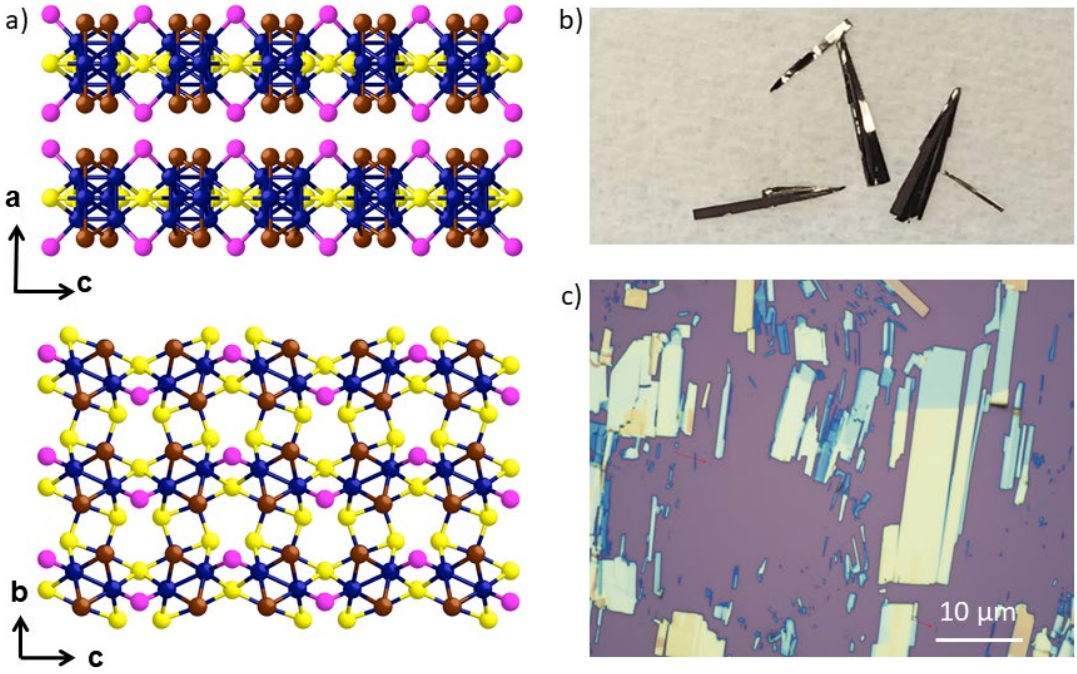

Figure 4.1 Crystal structure of $Mo_6S_3Br_6$. a) Top: side view of the crystal (looking down along *b*-axis) and bottom: top view of the crystal (looking along *a*-axis). Color code: Mo: blue; S: yellow; Br: brown (inner-cluster) and pink (inter-cluster bridging). b) optical image of the macroscopic $Mo_6S_3Br_6$ crystals with millimeter-sizes. c) optical image of the mechanical exfoliated $Mo_6S_3Br_6$ flakes on a Si/SiO_2 substrate.

morphology of these crystals (Figure 4.1b) indicates different growth rates along the *b*- and *c*-axes, consistent with the anisotropic in-plane structure described in the following section.

4.2.2 Crystal structure characterizations

$Mo_6S_3Br_6$ crystalizes in an orthorhombic structure with space group *Cmcm* (space group No.63). It derives from the Chevrel phase in which [Mo_6] octahedral cluster subunits are covalently linked into layers. Each [Mo_6] octahedron is tilted, enclosed in a pseudo-cube of S and Br, and connected to two neighboring clusters along the *c*-axis via a shared S atom located at the apical positions by forming six Mo-S bonds as well as via an additional two bridging Br atoms by Mo-Br-Mo linkages

(Figure 4.1a). The resulting corner-sharing one-dimensional chains of clusters are linked into layers in the *bc*-plane by means of two interchain Mo–S linkages along the *b*-axis. It thus can be described by the formula $[Mo_6S_{2/2}S_{2/2}Br_4]Br_{4/2}S_{2/2}$.The clusters form in such a way that the S atoms are inside the layers and the Br atoms are at the surface, establishing the van der Waals planes. These planes are stacked via van der Waals interactions along *a* direction, forming a layered crystal. The weak van der Waals contacts between the layers along the a-axis and strong in-plane bonding

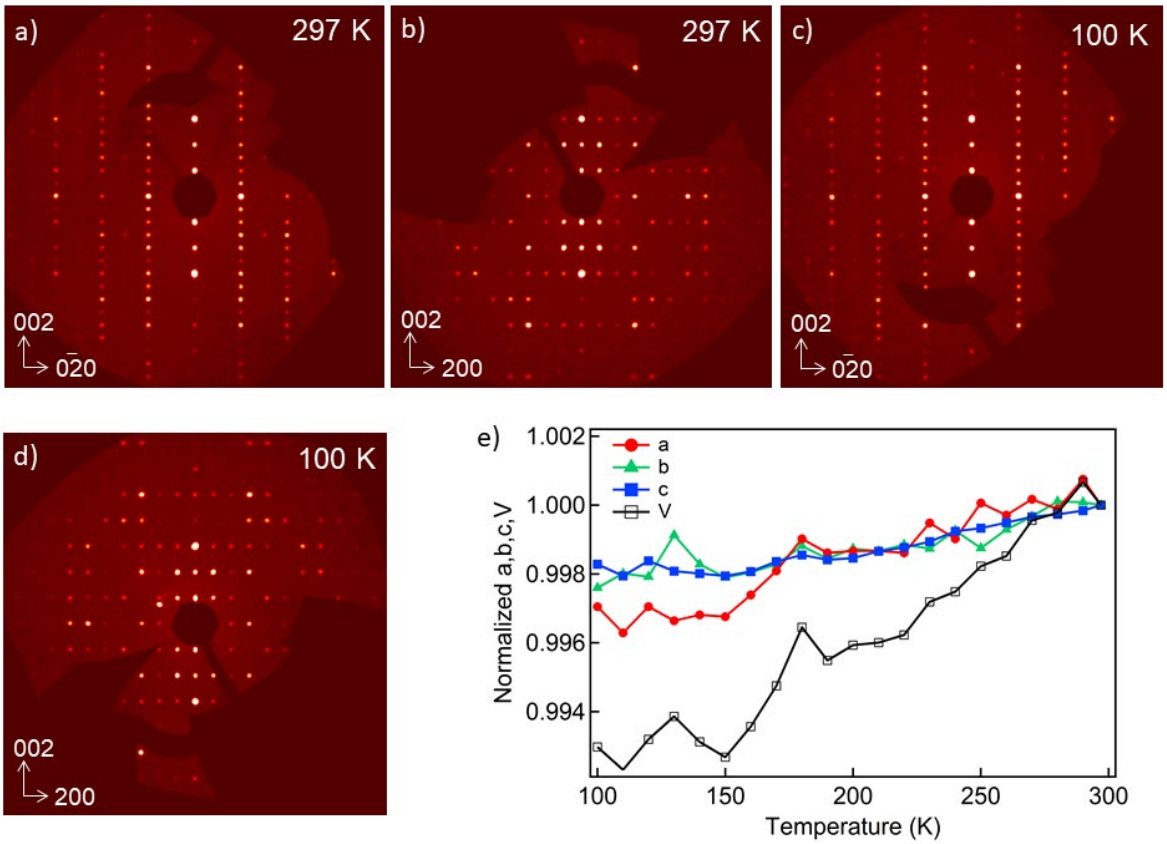

Figure 4.2 single crystal X-ray diffraction patterns of $Mo_6S_3Br_6$ crystal. a) b) Room temperature (297 K) patterns on the (100) plane and (010) plane, respectively. It confirms the orthorhombic structure with space group *Cmcm* of this crystal, in consistent with previous results. c) d) Low temperature (100 K) patterns on the (100) plane and (010) plane, respectively. It indicates that the crystal maintains the orthorhombic phase in the temperature range of 100 – 297 K. e) Temperature-dependent lattice parameters (normalized a, b, c and unit volume) of the orthorhombic $Mo_6S_3Br_6$. Lattice shrinking (~ 0.4%) at lower temperature is due to thermal effects.

give this material a robust 2D character with stronger coupling along the c-axis. Moreover, it allows for mechanical exfoliation of the crystals even down to mono- or few layers.

The structure of the synthesized crystals was determined by single crystal X-ray diffraction (SC-XRD).

Data was collected on an Agilent SuperNova instrument using a MiTeGen Micromount and an Oxford-Diffraction Cryojet system to cool the sample to 100 K. Data collection was performed using CrysAlis Pro while solution and subsequent refinement was done using ShelXT [91] and ShelXL [92], respectively, as mentioned in section 3.2.2. In agreement with previous reports [42], the structure is orthorhombic (*Cmcm* space group) with lattice parameters a =17.27 Å, b = 6.58 Å, c = 11.90 Å. The room-temperature diffraction patterns along the principal directions are shown in Figure 4.2a & b.

Temperature dependent measurements were carried out in temperature range of 100-300 K with every 10 K interval. To reduce the thermal fluctuations, the sample was stabilized for 15 min after reaching each target temperature. $Mo_6S_3Br_6$ shows monotonic increase of the lattice between 100 K and 297 K due to thermal expansion (Figure 4.2e) while it has no structural phase transition, as illustrated by SC-XRD patterns at 100 K (Figure 4.2c & d). Previous experiments revealed that $Mo_6S_3Br_6$ has semiconducting properties with activation energy of 0.037 eV for $100 < T < 297$ K and 0.020 eV for $T < 100$ K [126,130]. Due to the instrumental limit, we couldn't measure SC-XRD at lower temperatures. Therefore, further investigations of the crystal structure at temperature lower than 100 K is needed to study the phase transition in this material.

Experimentally, we mechanically exfoliated the bulk crystal using the Scotch tape method, which is commonly used for graphene and TMDCs. Figure 4.1d shows an optical image of $Mo_6S_3Br_6$ flakes with various sizes on a Si/SiO_2 substrate. Most flakes remain the rectangular shape similarly

to the original crystals. Reflected color represents the thickness of these flakes: the thinner the flake is, the lighter the color is. Quantitatively, the thicknesses of the resulting rectangular flakes are determined by atomic force microscopy (AFM) under ambient conditions. The thinnest flakes obtained using this approach are bilayers (Figure 4.3a) with thickness of ~ 2.5 nm (marked by red arrows in Figure 4.3b) and each step along the line profile is 2.1 nm on average (marked by blue arrows in Figure 4.3b), corresponding to the height of two monolayers based on the SC-XRD data (~1.8 nm). The apparent difference between the height measured by AFM and the SC-XRD data

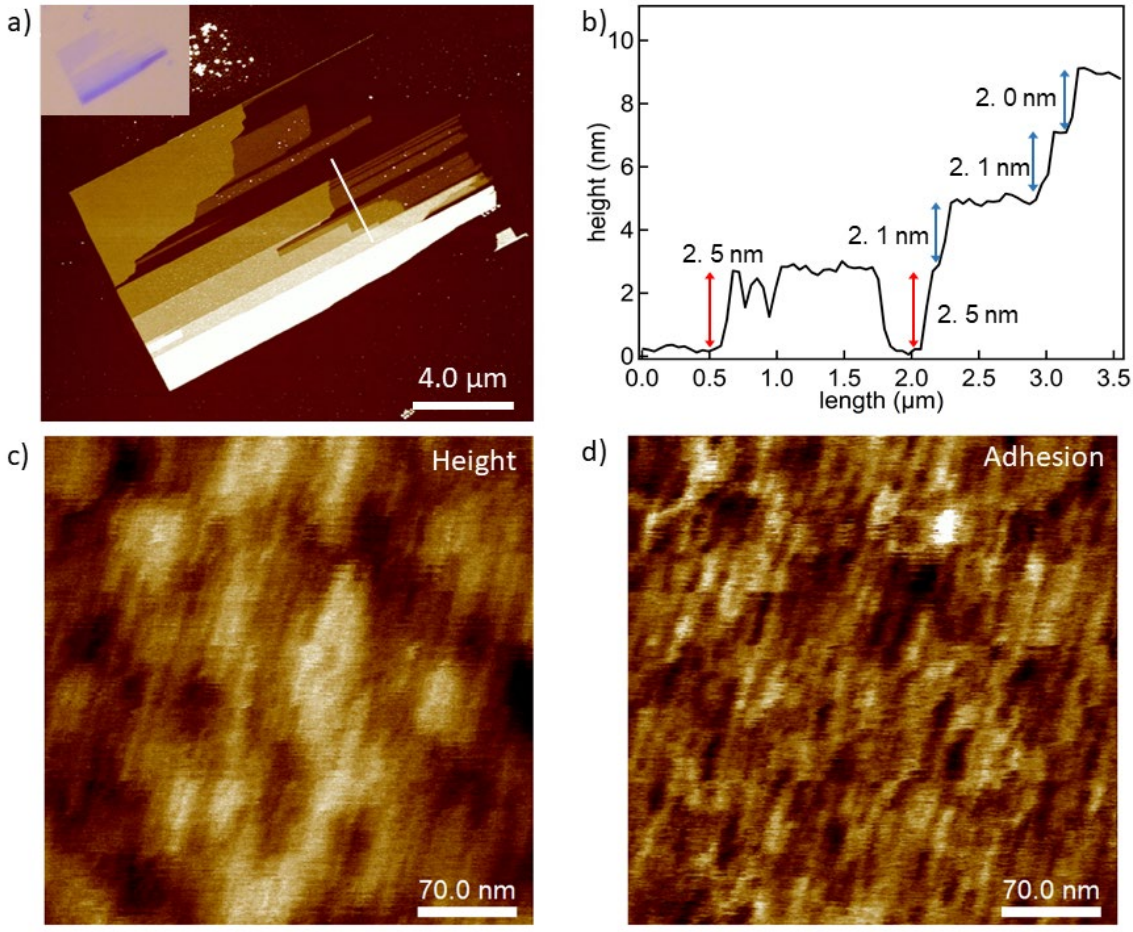

Figure 4.3 AFM characterizations on exfoliated thin films. a) AFM image on an exfoliated $Mo_6S_3Br_6$ flake on Si/SiO_2. Top inset: an optical image of exfoliated $Mo_6S_3Br_6$ flakes. b) Height profile along the white line in a). c) d) AFM image on freshly cleaved sample surface in height mode and adhesion mode, respectively, indicating the in-plane structural anisotropy.

is mainly due to the AFM tip - surface interactions, which overestimate the step height. The variation between the first layer and consequent layers can be attributed to the different interactions between the tip - SiO_2 and between the tip - $Mo_6S_3Br_6$ as well as the spacing between flakes and the Si/SiO_2 substrate. Moreover, AFM images on freshly cleaved sample surface are illustrated in Figure 4.3c and d in height mode and adhesion mode, respectively. Adhesion mode is obtained by adjusting the height of the tip to keep the adhesion force between the tip and the surface constant. Apparently, many stripes line up along the same direction with average spacing of ~ 12.5 nm. Each individual stripe has the needle-like morphology, in agreement with the in-plane structural anisotropy. The discontinuity among stripes in the same lines and the large surface roughness (~ 5.5 Å, one order of magnitude larger than that of $Re_6Se_8Cl_2$) indicate a high density of the intrinsic defects.

4.3 Anisotropic electronic properties of thin layer $Mo_6S_3Br_6$

4.3.1 STM on topological features

We carry out real-space imaging of the (100) surface structure of $Mo_6S_3Br_6$ using STM. $Mo_6S_3Br_6$ crystals are freshly cleaved in situ to prepare a clean surface. The high-resolution STM image in Figure 4.4a features the bright spots arranged in a triangular pattern with average periodicity of 6.6 ± 0.2 Å, 6.7 ± 0.3 Å, and 6.7 ± 0.4 Å. These bright spots with their associated distances correspond to the inter-cluster bridging Br atoms, which are protruding from the plane of the layer (represented as pink spheres in Figure 4.1a and 4.4a). The Br atoms located at the vertex of the $[Mo_6S_4Br_4]$ clusters are topographically lower than the bridging Br atoms, and thus are not clearly resolved in the STM at room temperature (represented as brown spheres in Figure 4.1a and 4.4a). Similar results are reported in other layered materials with non-identical topmost atoms [131]. The

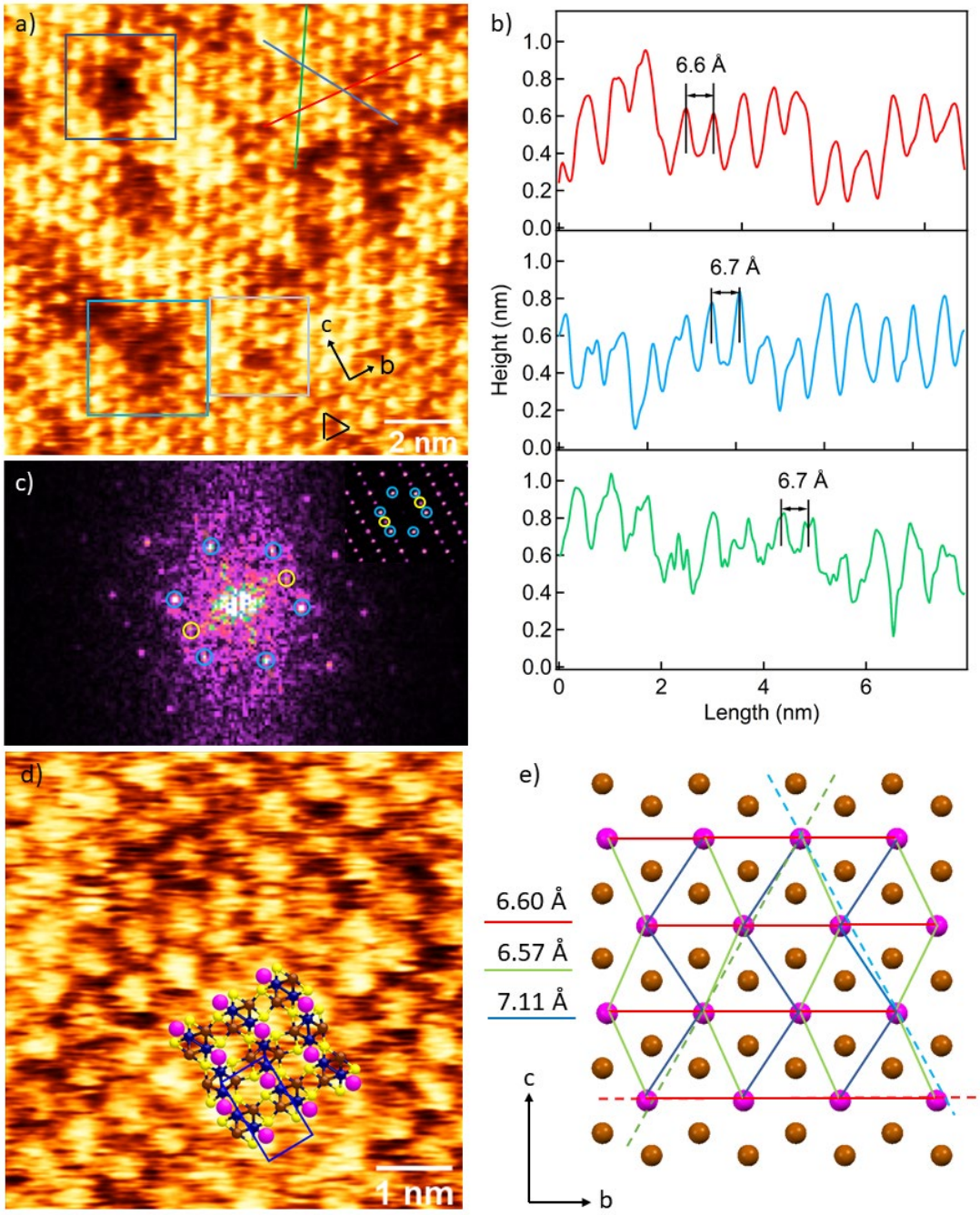

Figure 4.4 STM images on freshly cleaved $Mo_6S_3Br_6$ a) High-resolution STM image of $Mo_6S_3Br_6$ at 298 K (12 x 12 nm, U = 1.6 V, I = 60 pA). Three types of defects are marked with rectangular boxes. b) Line profiles along the red, blue and green lines in a) gives periodicities of 6.6 Å, 6.7 Å and 6.7 Å. c) Fast Fourier transform (FFT) of a). Inset is the simulated FFT of the top layer of Br atoms. (d) Zoom in STM image with $Mo_6S_3Br_6$ sitting on top of it. The bridging Br atoms (pink) match well with the bright spots. The unit cell is marked by the rectangular box. e) Schematic of the top layer of Br atoms arranged in a tilted triangular geometry. The red, blue and green dash lines correspond to the measured periodicity in the STM image.

bridging Br atoms arrange in a tilted triangular geometry with lengths of 6.60 Å, 6.57 Å and 7.11 Å from SC-XRD. The tilting is not obvious due to the thermal lattice vibrations at room temperature. Therefore, the measured periodicities along two directions are a combination of two sides of the triangular, as illustrated in Figure 4.4e (represented by the blue and green dash lines). By carefully analyzing the line profiles from the raw data and the filtered image (from fast Fourier transform), we determine the lengths of the Br atoms arranged tilted triangular to be 6.5 Å ,6.6 Å and 7.0 Å on average.

A Fourier transform (FFT) of the image (Figure 4.4c) identifies the pseudo six-fold symmetry of the bridging Br atoms. Two more points (identified as yellow circles in Figure 4.4c) indicates a periodicity of 5.9 Å along one direction, in excellent agreement with the *c* lattice parameter determined from SC-XRD (*c*/2 ~ 5.97 Å). By comparing the simulated FFT calculated from the bridging Br atom lattice (inset in Figure 4.4c) with the experimental data, we determine the *b* [010] and *c* [001] directions (represented as black arrows in Figure 4.4a and as a box in Figure 4.4d).

In addition to the crystal surface structure, we identify several types of defects in Figure 4.4a, including missing Br atoms or incomplete clusters. Three typical defects are highlighted with rectangular boxes in different colors in Figure 4.5a. The most obvious ones are missing clusters, appeared as dark holes with lateral dimension comparable to the clusters in the STM image (marked by the dark blue box and in Figure 4.5a). The striking height drop (~ 1.5 nm) is demonstrated in the line profile (Figure 4.5c) along the white line in Figure 4.5a. We also found several Br atoms sitting on the right positions with apparent height lower than their neighboring atoms (marked in the sky-blue box and in Figure 4.5d), as illustrated in the line profile (Figure 4.5f) along the white line in Figure 4.5d. It may result from electronic density of state change or the topological change induced by the defects underneath the top layer as well as the incomplete

cluster linked to the Br atoms. Besides, a shadow dark hole highlighted in the STM image (marked by the light blue box in Figure 4.5a) corresponds to incomplete clusters with breaking Mo-S linkages or missing Br atoms at the vertex of the $[Mo_6S_4Br_4]$ by comparing to the atomic structure of $Mo_6S_3Br_6$, shown in Figure 4.5e. Point defects of missing Br atoms are found as well in other

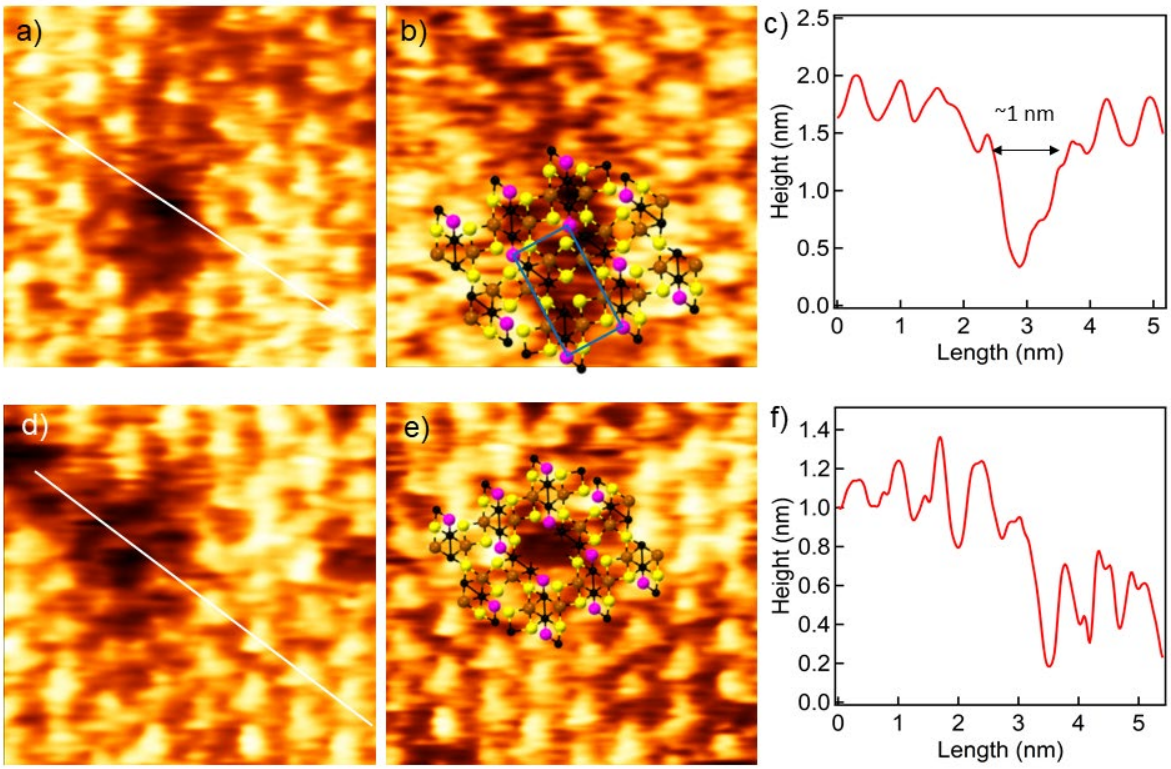

Figure 4.5 surface defects characterized by STM. a) missing entire clusters on the top layer. b) missing bridging Br atoms on the top layer with the atomic structure sitting on top of it. c) the line profile along the white line in a) showing a striking height drop. d) defects underneath the bridging Br atoms with lower apparent height compared to their neighboring atoms. e) defects with incomplete clusters with breaking Mo-S linkages or missing Br atoms at the at the vertex of the $[Mo_6S_4Br_4]$. f) line profile along the white line in d).

STM images shown in Figure 4.5b (not in Figure 4.5a) with the structure model laying on top of it. These defects could be bulk defects introduced into the crystals during the growth process or the surface defects induced by the stress during exfoliation. Defects types could be even more

complex and their effects on the electronic structure are reflected on the broad peak appeared in the band gap (see section 4.3.2).

4.3.2 STS on electronic band structures

We determine the single-particle electronic structure by current-voltage (I-V) measurement in STS. Figure 4.6 displays I-V (blue) and dI/dV-V (red) curves acquired on a cleaved $Mo_6S_3Br_6$ surface. Each I-V or dI/dV-V curve is an average of over 80 curves under the same tunneling conditions at multiple positions on the surface. Due to the thermal broadening effect at room temperature, the gap between the apparent edges (marked by the blue dash lines) is smaller than the real band gap (see section 2.1.3). The positions of the band edges relative to E_F indicates p-doping. A weak and broad mid-gap feature near E_F attributed to surface defects.

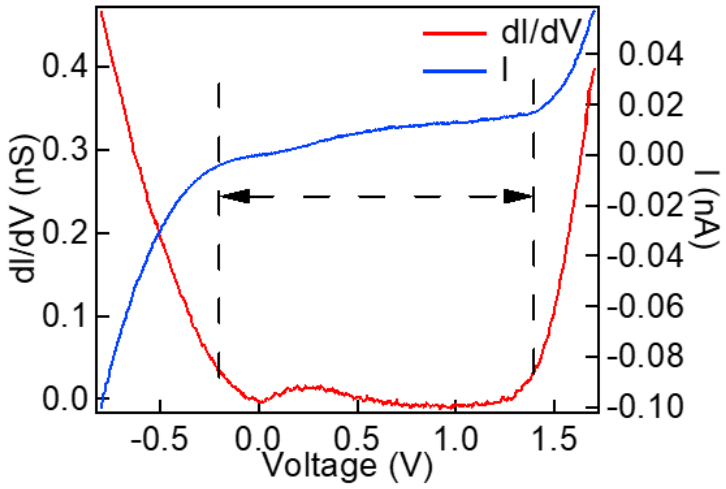

Figure 4.6 electronic band gap determined by STS. STS spectrum with I-V curve in blue and the dI/dV-V curve in red. The VBM and CBM are marked by the black dashed lines, giving a bandgap of 1.64 ± 0.05 eV.

To accurately determine the band edges, we model the conduction band in the positive voltage range of the I-V spectra by using the tunneling current expression:

$$I \propto \int_{-\infty}^{\infty} \left[\frac{1}{1+e^{(\varepsilon-V)/k_BT}} - \frac{1}{1+e^{\varepsilon/k_BT}}\right] \rho_s(\varepsilon) e^{-2d\frac{\sqrt{2m}}{\hbar}\sqrt{\frac{\phi_s+\phi_t}{2}+\frac{eV_B}{2}-\varepsilon}} d\varepsilon \quad (4.1)$$

derived from Eq.2.5 and Eq.2.3 in section 2.1.2. Assuming the density of states (DOS) of the sample has a constant value above CBM and below VBM, respectively and becomes zero in the gap, the integral is narrowed to a finite range. It gives the CBM located at 1.44 ± 0.03 V. Measured current does not reach to zero in the bandgap region due to the mid-gap states, which makes it difficult to simulate in the valence band range. Therefore, we determine the VBM by using the dI/dV – V spectra, which gives the value of –0.20 V ± 0.03 V and thus the electronic bandgap $E_G = E_{CBM} – E_{VBM}$ = 1.64 ± 0.05 eV.

4.3.3 DFT calculations on band structures

To support our experimental observations, we carry out DFT calculation of the electronic band structure of $Mo_6S_3Br_6$ using the Perdew-Burke-Ernzherof (PBE) functional [103] and refine the calculation with the hybrid Heyd-Scuseria-Ernzerhof (HSE06) functional [104]. Figure 4.7a displays the PBE bulk electronic band structure (black curves) and HSE06 refinements at selected high-symmetry points in the Brillouin zone (blue dots). A direct bandgap of 0.90 eV is obtained from PBE functional, which typically underestimates the bandgap. The HSE06 band structure, which typically overestimates bandgaps, indicates a direct bandgap of 1.69 eV, slightly above the experimentally-determined value. Both VBM and CBM locate at (0,0.5,0) k-point. To understand the properties of $Mo_6S_3Br_6$ in the 2D limit, we performed similar calculations on the 2D monolayer, as shown Figure 4.7b. Monolayer $Mo_6S_3Br_6$ possesses a nearly identical band structure to the bulk, indicating weak inter-layer electronic interactions. The direct band gap calculated from PBE and HSE06 functional has the same value at Y (0,0.5,0) k-point as that of the bulk.

Strong anisotropy appears in the band structure along the principal direction S (0, 0.5, 0) - Γ compared to S-Y (-0.5, 0.5, 0) in the bulk and Y (0, 0.5, 0) - Γ compared to Y – M (0.5, 0.5, 0) in the 2D. The electronic structure produces two free electron-like bands with starkly different effective masses for electrons and holes, respectively. Similar band structures have been observed in other anisotropic 2D materials, e.g. black phosphorus [55,132].

The strong in-plane anisotropy is also reflected in the Fermi surface of $Mo_6S_3Br_6$, both in the intrinsic and doped states. Figure 4.7c displays the Fermi surface for an undoped 2D monolayer.

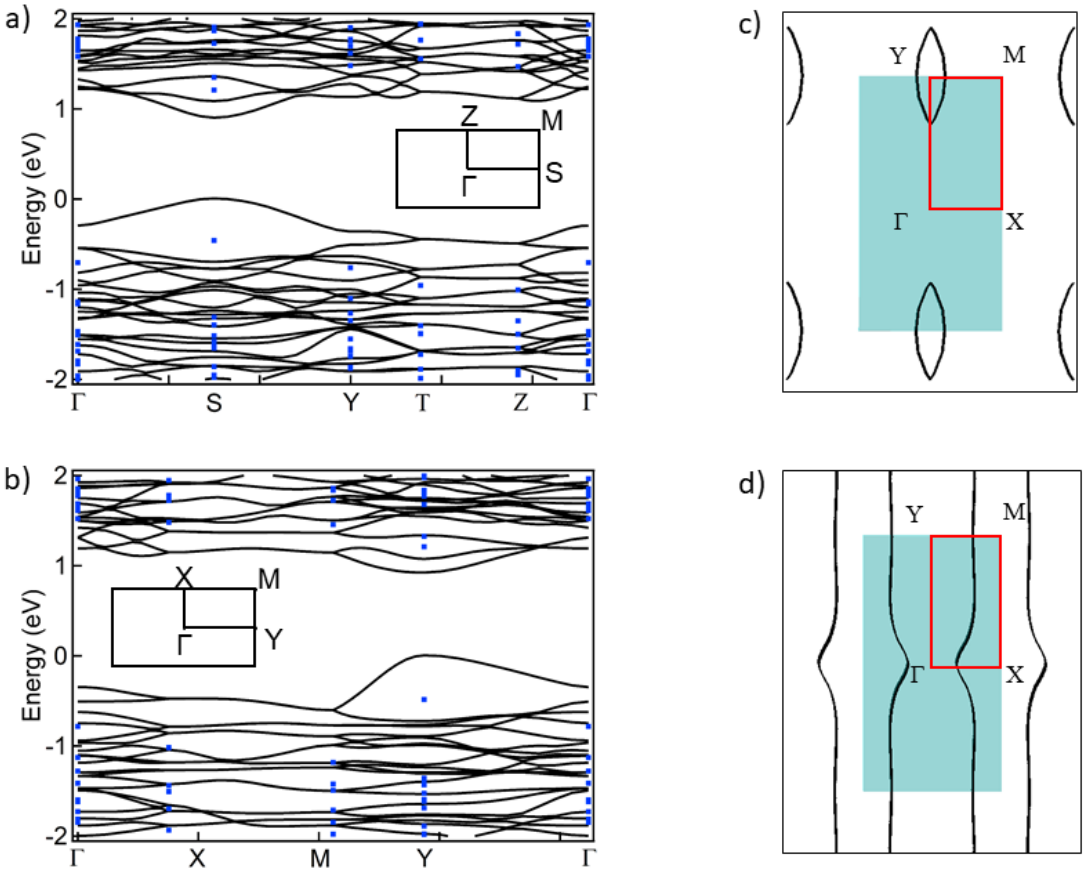

Figure 4.7 DFT calculated band structure in PBE-SOC (solid black line) and HSE06-SOC (blue dots). Inset is the 2D Brillouin zone projected on (100) plane. a) is for 3D bulk and b) is the 2D monolayer. c) Fermi surface of an undoped 2D monolayer. d) Fermi surface of p-doped 2D monolayer with doping level of 0.5 holes/cluster.

By increasing the doping level to 0.5 hole per cluster, the band along the Γ−Y direction generates pseudo-1D electronic chains (Figure 4.7d), revealing highly anisotropic electronic properties.

4.4 Anisotropy resolved in Raman spectroscopy

Raman spectroscopy has been in widespread use to characterize the structural and electronic properties of 2D materials, ever since the discovery of graphene [133–135]. The obtained Raman spectrum provides information on peak position, intensity, line-shape and full width at half maxima (FWHM), which determines the number of layers [125,135,136], crystalline orientation [137], defects, edges [138] and is strongly related to the effects from doping, strain [139] and magnetic fields.

Particularly, polarization dependent Raman spectroscopy is a powerful tool to study the in-plane anisotropic properties of the materials. Each Raman active mode displays distinctive polarization-dependent intensity according to the structural symmetry and vibrational symmetry. Therefore, we use the polarization dependent Raman spectroscopy to detect the anisotropic properties of $Mo_6S_3Br_6$.

4.4.1 Polarization dependent Raman

Polarization dependent Raman spectroscopy was performed with a Renishaw microscopic Raman spectrometer (Figure 4.8a). Spectra were taken in a backscattering geometry, where the incident and scattered light are both perpendicular to the sample. A 1mW 633 nm He-Ne laser was focused on the $Mo_6S_3Br_6$ surface with ~1 μm spot size. A linear polarizing filter was used in the laser path before the sample to purify polarization, and an additional polarizer was placed between sample and detector to reject cross-polarized light at parallel polarizing configuration. After the polarizing filter within the incident path, a removable half waveplate was placed at a 45˚ angle between the

fast axis and laser polarization, so that the parallel and cross polarized configurations could be switched with ease. The polarization angle is defined as the angle between the incident polarization and the crystal *c*-axis. The sample was manually rotated by 15˚ for each measurement (Figure 4.8b).

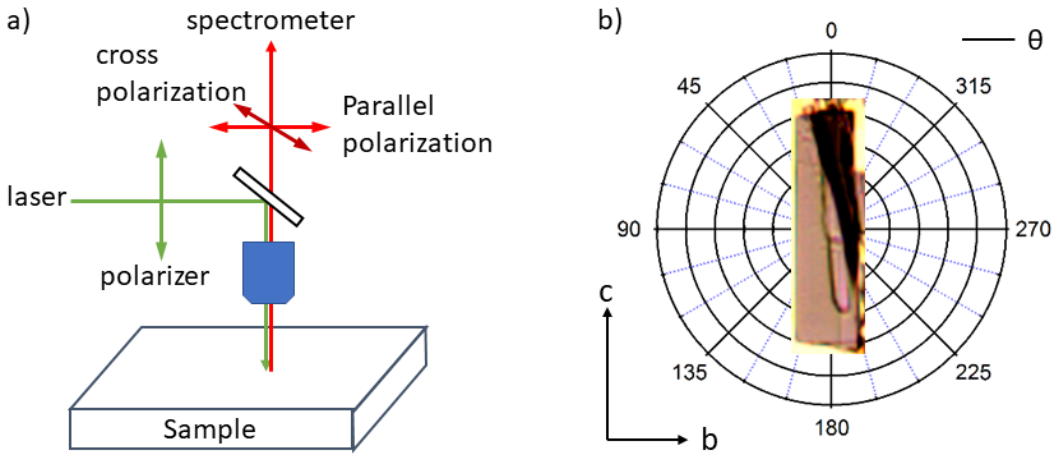

Figure 4.8 Schematic of the polarization dependent Raman spectroscopy a) in a backscattering geometry. Spectra were taken in both parallel polarization and cross polarization configurations. b) The polarization angle θ is the angle between the incident polarization and the crystal *c*-axis. θ changes by rotating the sample clockwise.

Figure 4.9a shows angular dependent Raman spectra for parallel polarization (PP) (top) and cross polarization (CP) (bottom) configurations. Each Raman active mode has either two- or four- fold symmetry governed by the crystal symmetry. Since $Mo_6S_3Br_6$ has an orthorhombic structure with space group *Cmcm*, there are 45 Raman active modes ($13A_g + 11\ B_g + 9\ B_{2g} + 12\ B_{3g}$) [140], among which 25 modes ($13A_g + 12\ B_{3g}$) are detectable in the backscattering geometry we used experimentally. Raman selection rules dictate that A_g mode has two-fold symmetry for parallel polarization and four-fold symmetry for cross polarization, while B_{3g} mode has four-fold symmetry in either parallel polarizing or cross polarizing configuration (also see calculations on Raman tensor in section 4.4.2). Figure 4.9b presents parallel-polarized Raman spectra at 0º, 30º,

60º, 90º: 15 of 25 Raman modes are resolved and assigned to A_g or B_{3g} mode according to DFT calculations.

To clearly resolve the anisotropic Raman responses evolving with angles, figure 4.10 displays normalized parallel-polarized (top) and cross-polarized (bottom) Raman polar plots of three

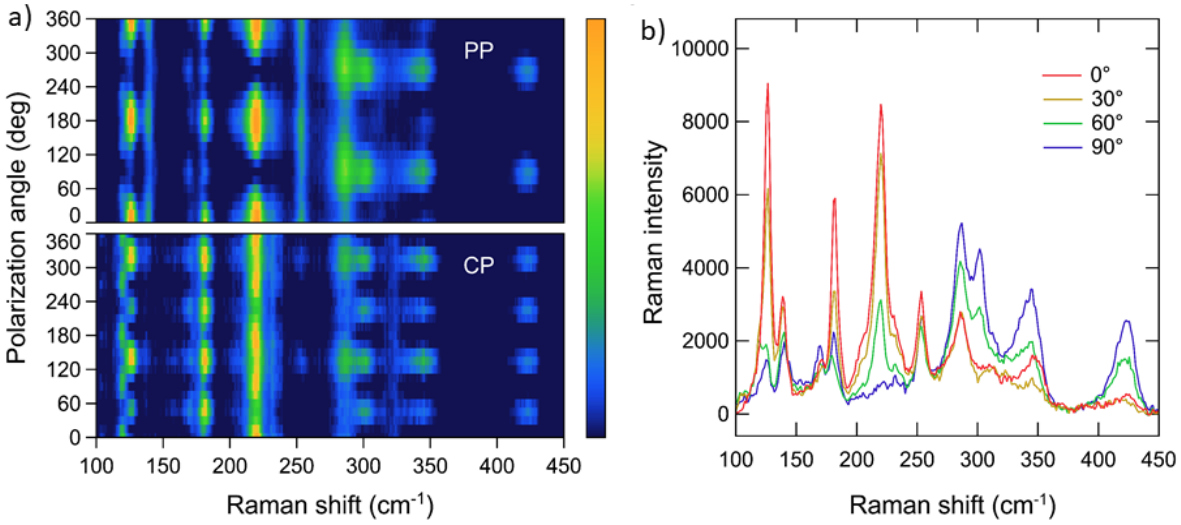

Figure 4.9 Polarization dependent Raman spectra. a) Image plots of polarization dependent Raman for parallel polarization (PP) (top) and cross polarization (CP) (bottom). 0˚ angle denotes the c axis of the crystal. b) Representative parallel-polarized Raman spectra at 0º, 30º, 60º, 90º.

representative Raman peaks with the corresponding phonon modes.

We first focus on the Raman responses in the parallel polarized configuration. The Raman intensity of the B_{3g} (119.7 cm^{-1}) mode shows four-fold symmetry and reach to the minimum along *b*- and *c*- axes and maximum along off-diagonal position at 45º (225º) and 135º (315º). The Raman intensity of A_g modes shows two-fold symmetry and reach maximum along *c*-axis or *b*-axis. The strong in-plane anisotropy of $Mo_6S_3Br_6$ is also reflected in the separation of the A_g modes: the maximum peak intensity of the A_g modes below 270 cm^{-1} is at 0 º and 180 º (along *c*-axis) while those above 270 cm^{-1} is at 90 º and 270 º (along *b*-axis). This anisotropy is evident when comparing

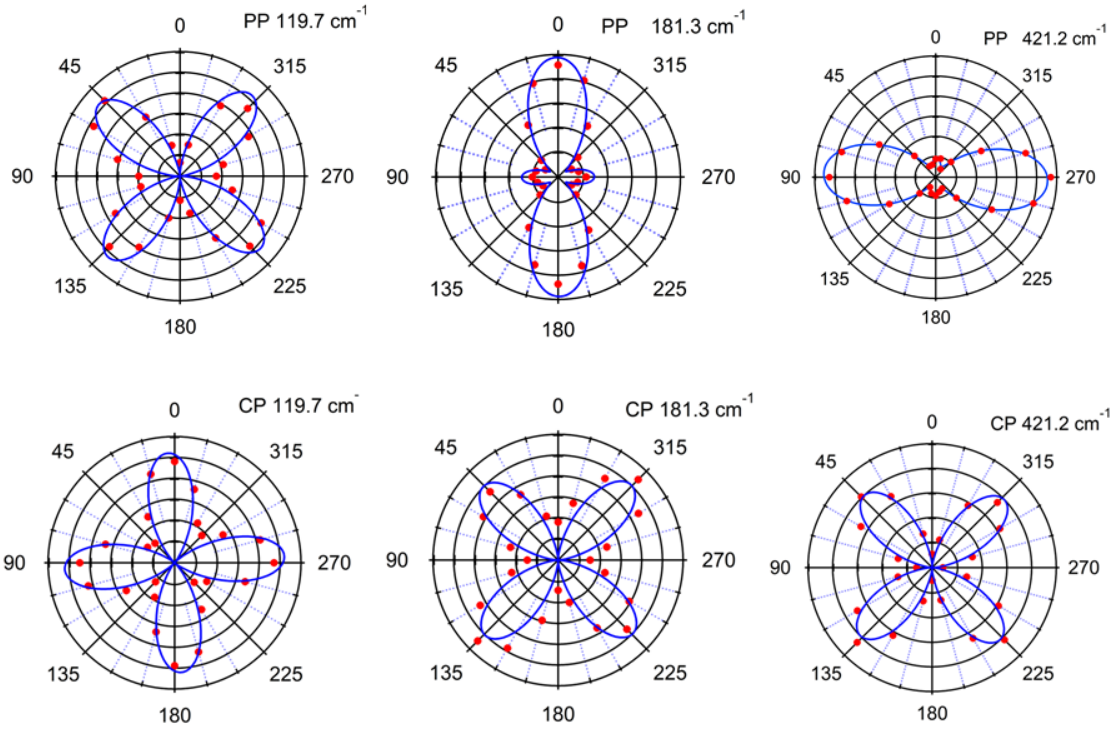

Figure 4.10 Polar plots of Raman intensity of eight representative Raman active modes in a) parallel-polarized configuration and b) cross-polarized configuration, respectively. c) DFT calculated phonon modes corresponded to each mode. Red dotted curves represent experimental data and blue curves represent the fitting curves.

the polar plots of A_g modes 181.3 cm^{-1} and 421.2 cm^{-1} shown in Figure 4.10. Moreover, the intensity of A_g (181.3 cm^{-1}) along the *b*-axis is a secondary maximum instead of a minimum, as seen in other 2D materials [141–143].

We then concentrate on the cross polarized Raman spectra in Figure 4.10. The Raman intensity of the B_{3g} (119.7 cm^{-1}) mode shows four-fold symmetry and reach to the maximum along *b*- and *c*-axes and minimum along off-diagonal position at 45° (225°) and 135° (315°), which is opposite to the parallel polarized configuration. Since B_{3g} mode only has non-zero elements in the off-diagonal positions in the Raman tensor, the polarization of the incident will shift 90° while scattering from the sample. It results in the maximum intensity along *b* and *c* axes in the cross polarized

configuration. The cases of A_g modes 181.3 cm^{-1}, 421.2 cm^{-1} show minimum intensity along *b*- and *c*- axes, which can be ascribed to the zero elements in non-diagonal positions in the Raman tensor.

4.4.2 Quantitative analysis of Raman tensors

We performed a quantitative analysis of the phonon anisotropy by extracting Raman tensors for A_g and B_{3g} modes from the polarization dependent Raman spectra in parallel and cross polarizing configurations. The Raman intensity [98] can be expressed as

$$I \propto |\boldsymbol{e}_i \boldsymbol{R} \boldsymbol{e}_s|^2 \tag{4.2}$$

where $\boldsymbol{e}_i$ and $\boldsymbol{e}_s$ are the incident and scattered light vectors and **R** is the Raman tensor for a specific phonon mode. For incident light perpendicular to the sample (i.e. parallel to the *a*-axis), the incident light vector $\boldsymbol{e}_i = (0, sin\theta, cos\theta)$ and the scattered light vector is $\boldsymbol{e}_s = (0, sin\theta, cos\theta)$ for parallel-polarized configuration and $\boldsymbol{e}_s = (0, -cos\theta, sin\theta)$ for cross-polarized configuration. The Raman tensors of A_g and B_{3g} are given by:

$$\vec{R}_{A_g} = \begin{bmatrix} ae^{i\varphi_a} & 0 & 0 \\ 0 & be^{i\varphi_b} & 0 \\ 0 & 0 & ce^{i\varphi_c} \end{bmatrix}, \qquad \vec{R}_{B_g} = \begin{bmatrix} 0 & de^{i\varphi_d} & 0 \\ de^{i\varphi_d} & 0 & 0 \\ 0 & 0 & 0 \end{bmatrix},$$

$$\vec{R}_{B_{2g}} = \begin{bmatrix} 0 & 0 & ee^{i\varphi_e} \\ 0 & 0 & 0 \\ ee^{i\varphi_e} & 0 & 0 \end{bmatrix}, \qquad \vec{R}_{B_{3g}} = \begin{bmatrix} 0 & 0 & 0 \\ 0 & 0 & fe^{i\varphi_f} \\ 0 & fe^{i\varphi_f} & 0 \end{bmatrix}, \tag{4.3}$$

where a,b,c,d,e,f are the amplitudes and $\varphi_a, \varphi_b, \varphi_c, \varphi_d, \varphi_e, \varphi_f$ are the phase factors of the complex Raman tensors, respectively. The phase factor (imaginary part) in the Raman tensor elements are attributed to photon absorption with excitation photon energy above the band gap, and purely real Raman tensor fails to properly fit angular dependence of Raman spectra. we determine that

$|\boldsymbol{e}_i\vec{R}_{B_g}\boldsymbol{e}_s|^2$ and $|\boldsymbol{e}_i\vec{R}_{B_{2g}}\boldsymbol{e}_s|^2$ are zero, indicating that $\vec{R}_{B_g}$ and $\vec{R}_{B_{2g}}$ modes are not detectable in our experiments, as mentioned in section 4.4.1. The Raman intensity for A_g and B_{3g} modes in parallel and cross polarized configuration can be expressed as:

$$\mathrm{I}(A_g, \parallel) \propto b^2 sin^4\theta + c^2 cos^4\theta + 2bccos^2\theta sin^2\theta cos\varphi_{BC} \tag{4.4}$$

$$\mathrm{I}(A_g, \perp) \propto (b^2 + c^2 - 2bccos\varphi_{BC}) sin^2\theta cos^2\theta \tag{4.5}$$

$$\mathrm{I}(B_{3g}, \parallel) \propto f^2 sin^2 2\theta \tag{4.6}$$

$$\mathrm{I}(B_{3g}, \perp) \propto f^2 cos^2 2\theta \tag{4.7}$$

By fitting both parallel and cross polarized Raman spectra simultaneously, we obtain the tensor elements of each mode. The fits, included in the polar plots in Figure 4.10 as blue solid lines demonstrate an excellent agreement between experimental and theoretical data.

4.5 Conclusions

In summary, we have demonstrated that the layered van der Waals cluster solid $Mo_6S_3Br_6$ can be used to create a novel 2D semiconductor with strong in-plane anisotropy. This structural and electronic anisotropy allows the generation of psedu-1D electronic chain by tuning the doping level in this system, as predicted by the DFT calculations. It is therefore anticipated to produce directional transport of charge and energy, such as carriers, excitons and polaritons, which has great potential for the fabrication of angle-resolved electronics. Moreover, the unique hierarchical structure of $Mo_6S_3Br_6$ opens the door to next-generation optoelectronic devices that combine multifunctionality and in-plane anisotropy and expands the design space for 2D materials.

Chapter 5

Conclusions

Here, we have explored two materials in the family of 2D superatomic semiconductors: $Re_6Se_8Cl_2$ and $Mo_6S_3Br_6$, whose building blocks are atomic clusters rather than simple atoms. The combination of functionalized hierarchical cluster units featuring atomic precision and the layered van der Waals structures bridges the gap between conventional solid-state chemistry and newly developed 2D materials.

In Chapter 3, we have determined the electronic bandgap (1.58 eV), optical bandgap (indirect, 1.48 eV), and exciton binding energy (100 meV) of the $Re_6Se_8Cl_2$ crystals. The latter is consistent with the partially 2D excitonic effects, indicating quasi-2D characters in this layered van der Waals materials.

An obvious research direction is to optimize the exfoliation method to reach the monolayer limit. It is recently realized in a lithium intercalation followed by liquid exfoliation process and produces micrometer-sized nanosheets [47]. Our calculations at the HSE06-SOC level predict that the bandgap of $Re_6Se_8Cl_2$ increases from 1.49 eV in the bulk to 1.72 eV at the monolayer limit and remains indirect. It is therefore intriguing to study the distinctive electronic properties especially

the excitonic effects in this real 2D hierarchical system. Moreover, the limited inter-cluster electronic coupling within each layer produces an electronic structure with narrow bandwidth (≤ 0.5 eV) which is expected to be highly sensitive to phonon modes arising from the collective motions of the "superatomic" units. The 2D hierarchical structure of $Re_6Se_8Cl_2$ is thus an intriguing model system for investigating strong electron-phonon coupling and related electronic phase transitions. Strong coherent phonon vibrations have been detected in $Re_6Se_8Cl_2$ and this work is undergoing in our lab. Furthermore, as mentioned in Chapter 1, the presence of substitutional labile Cl atoms on the surface of each $Re_6Se_8Cl_2$ layer opens the door to surface functionalization via halogen substitution, which could allow tuning of the electronic structure and fabricating functional devices.

In Chapter 4, we have demonstrated the strong in-plane electronic anisotropy in the layered van der Waals semiconducting $Mo_6S_3Br_6$. This structural and electronic anisotropies allow generating a pseudo-1D electronic chain by tuning the doping level in this system, as predicted by the DFT calculations. It can be used for directional transport of charge and energy, such as carriers, excitons and polaritons. One obvious direction is to investigate the in-plane conductivity by transport measurements. In the scientific perspective, $Mo_6S_3Br_6$ provides us a new system for anisotropic exciton and polariton studies, which has been investigated in simple systems such as black phosphorous. Although the bulk $Mo_6S_3Br_6$ possesses 2D characters as indicated by the DFT calculations on the band structures of the bulk and the monolayer, it is of interest to produce real 2D sheets in combination of the complex, hierarchical structures and the in-plane anisotropy. This work is undergoing in our lab as well. Resembling the Cl atoms on the surface of $Re_6Se_8Cl_2$ layers, the presence of labile Br atoms (bridging Br atoms) at the surface of 2D $Mo_6S_3Br_6$ may allow us to tune the anisotropic properties of this material by functionalizing their surface via halogen

substitution. Moreover, the activation energy of $Mo_6S_3Br_6$ crystals above 100 K is 37 meV while it decreases to 20 meV below 100 K, as shown in the literatures. It is important to understand the origin of this transition and the possible structural or electrical phase transitions in this system.

In summary, the exploration of these two superatomic van der Waals semiconductors demonstrates the 2D characters in the bulk. Such unique structures with 2D characters will stimulate the design of 2D materials with multiply functions and allow us to explore novel properties in low-dimensional physics.

References

1. Novoselov, K. S., Mishchenko, A., Carvalho, A. & Neto, A. H. C. 2D materials and van der Waals heterostructures. *Science (80-.).* **353,** aac9439 (2016).
2. Novoselov, K. S. *et al.* A roadmap for graphene. *Nature* **490,** 192–200 (2013).
3. Novoselov, K. S. *et al.* Two-dimensional atomic crystals. *Proc. Natl. Acad. Sci.* **102,** 10451–10453 (2005).
4. Mak, K. F., Lee, C., Hone, J., Shan, J. & Heinz, T. F. Atomically thin MoS2: A new direct-gap semiconductor. *Phys. Rev. Lett.* **105,** 2–5 (2010).
5. Splendiani, A. *et al.* Emerging photoluminescence in monolayer MoS2. *Nano* (2010).
6. Xu, X., Yao, W., Xiao, D. & Heinz, T. F. Spin and pseudospins in layered transition metal dichalcogenides. *Nat. Phys.* **10,** 343–350 (2014).
7. Song, L. *et al.* Large scale growth and characterization of atomic hexagonal boron nitride layers. *Nano Lett.* **10,** 3209–3215 (2010).
8. Watanabe, K., Taniguchi, T. & Kanda, H. Direct-bandgap properties and evidence for ultraviolet lasing of hexagonal boron nitride single crystal. *Nat. Mater.* **3,** (2004).
9. Ramasubramaniam, A. Large excitonic effects in monolayers of molybdenum and tungsten dichalcogenides. *Phys. Rev. B - Condens. Matter Mater. Phys.* **86,** 1–6 (2012).
10. Berkelbach, T. C., Hybertsen, M. S. & Reichman, D. R. Theory of neutral and charged excitons in monolayer transition metal dichalcogenides. *Phys. Rev. B* **88,** 045318 (2013).

11. Chernikov, A. *et al.* Exciton Binding Energy and Nonhydrogenic Rydberg Series in Monolayer WS 2. *Phys. Rev. Lett.* **113,** 076802 (2014).

12. Ugeda, M. M. *et al.* Observation of giant bandgap renormalization and excitonic effects in a monolayer transition metal dichalcogenide semiconductor. *Nat. Mater.* **13,** 1091–1095 (2014).

13. Xu, X., Yao, W., Xiao, D. & Heinz, T. Spin and pseudospins in layered transition metal dichalcogenides. *Nat. Phys.* (2014).

14. Xiao, D., Liu, G. Bin, Feng, W., Xu, X. & Yao, W. Coupled spin and valley physics in monolayers of MoS 2 and other group-VI dichalcogenides. *Phys. Rev. Lett.* **108,** 1–5 (2012).

15. Huang, B. *et al.* Layer-dependent ferromagnetism in a van der Waals crystal down to the monolayer limit. *Nature* **546,** 270–273 (2017).

16. Qian, X., Liu, J., Fu, L. & Li, J. Quantum spin hall effect in two - Dimensional transition metal dichalcogenides. *Science (80-.).* **346,** 1344–1347 (2014).

17. Fei, Z. *et al.* Topological insulator behavior in monolayer WTe 2. *ArXiv CondMat* 1610.07924 (2016). doi:10.1038/nphys4091

18. Tsen, A. W. *et al.* Nature of the quantum metal in a two-dimensional crystalline superconductor. *Nat. Phys.* **12,** 208–212 (2016).

19. Koppens, F., Mueller, T., Avouris, P. & Ferrari, A. Photodetectors based on graphene, other two-dimensional materials and hybrid systems. *Nat. Nanotechnol.* **9,** 780–793 (2014).

20. Wang, Q. H., Kalantar-Zadeh, K., Kis, A., Coleman, J. N. & Strano, M. S. Electronics and optoelectronics of two-dimensional transition metal dichalcogenides. *Nat. Nanotechnol.* **7,** 699–712 (2012).

21. Mak, K. F. & Shan, J. Photonics and optoelectronics of 2D semiconductor transition metal dichalcogenides. *Nat. Photonics* **10,** 216–226 (2016).

22. He, K., Poole, C., Mak, K. F. & Shan, J. Experimental demonstration of continuous electronic structure tuning via strain in atomically thin MoS2. *Nano Lett.* **13,** 2931–2936 (2013).

23. Scalise, E., Houssa, M., Pourtois, G., Afanas'ev, V. & Stesmans, A. Strain-induced semiconductor to metal transition in the two-dimensional honeycomb structure of MoS 2. *Nano Res.* **5,** 43–48 (2012).

24. Cao, Y. *et al.* Unconventional superconductivity in magic-angle graphene superlattices. *Nature* **556,** 43–50 (2018).

25. Cao, Y. *et al.* Correlated insulator behaviour at half-filling in magic-angle graphene superlattices. *Nature* **556,** 80–84 (2018).

26. Jin, C. *et al.* Ultrafast dynamics in van der Waals heterostructures. *Nat. Nanotechnol.* **13,** 994–1003 (2018).

27. Mak, K. F. & Shan, J. Opportunities and challenges of interlayer exciton control and manipulation. *Nat. Nanotechnol.* **13,** 974–976 (2018).

28. Butler, S., Hollen, S., Cao, L., Cui, Y. & Gupta, J. Progress, challenges, and opportunities in two-dimensional materials beyond graphene. *ACS Nano* **7,** 2898–2926 (2013).

29. Mannix, A., Kiraly, B. & Hersam, M. Synthesis and chemistry of elemental 2D materials. *Nat. Rev.* **1,** 0014 (2017).

30. Molle, A., Goldberger, J., Houssa, M., Xu, Y. & Zhang, S. Buckled two-dimensional Xene sheets. *Nat. Mater.* **16,** 163–169 (2017).

31. Andres, R. P. *et al.* Self-assembly of a two-dimensional superlattice of molecularly linked metal clusters. *Science* **273,** 1690–1693 (1996).

32. Medeiros-Ribeiro, G., Ohlberg, D. A. A., Williams, R. S. & Heath, J. R. Rehybridization of electronic structure in compressed two-dimensional quantum dot superlattices. *Phys. Rev. B* **59,** 1633 (1999).

33. Boneschanscher, M. P. *et al.* Long-range orientation and atomic attachment of nanocrystals in 2D honeycomb superlattices. *Science* **344,** 1377–1380 (2014).

34. Shevchenko, E. V, Talapin, D. V, Kotov, N. A., Brien, S. O. & Murray, C. B. Structural diversity in binary nanoparticle superlattices. *Nature* **439,** 55–59 (2006).

35. Peña, O. Chevrel phases: Past, present and future. *Phys. C Supercond. its Appl.* **514,** 95–112 (2015).

36. Xie, W. *et al.* Endohedral gallide cluster superconductors and superconductivity in $ReGa_5$. *Proc. Natl. Acad. Sci.* 201522191 (2015). doi:10.1073/pnas.1522191112

37. Perrin, A. & Perrin, C. The molybdenum and rhenium octahedral cluster chalcohalides in solid state chemistry: From condensed to discrete cluster units. *Comptes Rendus Chim.* **15,** 815–836 (2012).

38. Roy, X. *et al.* Nanoscale atoms in solid-state chemistry. *Science.* **341,** 157–60 (2013).

39. Choi, B. *et al.* van der Waals Solids from Self-Assembled Nanoscale Building Blocks. *Nano Lett.* **16,** 1445–1449 (2016).

40. Brien, E. S. O. *et al.* Single-crystal-to-single-crystal intercalation of a low-bandgap superatomic crystal. *Nat. Chem.* **9,** 1170–1174 (2017).

41. Leduc, L., Perrin, A. & Sergent, M. Structure du dichlorure et octaséléniure d'hexarhénium, Re6Se8Cl2: composé bidimensionnel à clusters octaédriques Re6. *Acta Crystallogr. Sect. C* (1983).

42. Perrin, C., M., P. & Sergent, M. Nouveau Compos6 Bidimensionnel ~ Clusters Oeta6driques. *Acta Crystallogr. Sect. C* 1–4 (1983).

43. Cheiwchanchamnangij, T. & Lambrecht, W. R. L. Quasiparticle band structure calculation of monolayer, bilayer, and bulk MoS2. *Phys. Rev. B* **85,** 1–4 (2012).

44. Kadantsev, E. S. & Hawrylak, P. Electronic structure of a single MoS 2 monolayer. *Solid State Commun.* **152,** 909–913 (2012).

45. Georgakilas, V. *et al.* Functionalization of graphene: Covalent and non-covalent approaches, derivatives and applications. *Chem. Rev.* **112,** 6156–6214 (2012).

46. Suh, J. *et al.* Doping against the native propensity of MoS2: Degenerate hole doping by cation substitution. *Nano Lett.* **14,** 6976–6982 (2014).

47. Choi, B. *et al.* Two-Dimensional Hierarchical Semiconductor with Addressable Surfaces. *J. Am. Chem. Soc.* **140,** 9369–9373 (2018).

48. McLean, T. P. & Loudon, R. Exciton energy levels in germanium and silicon. *J. Phys. Chem. Solids* **13,** 1–9 (1960).

49. Sturge, M. D. Optical Absorption of Gallium Arsenide between 0.6 and 2.75 eV. *Phys. Rev.* **127,** 768–773 (1962).

50. Saigal, N., Sugunakar, V. & Ghosh, S. Exciton binding energy in bulk MoS_2: A reassessment. *Appl. Phys. Lett.* **108,** 132105 (2016).

51. Komsa, H.-P. & Krasheninnikov, A. V. Effects of confinement and environment on the electronic structure and exciton binding energy of MoS 2 from first principles. *Phys. Rev. B* **86,** 241201 (2012).

52. Klingshirn, C. F. *Semiconductor Optics*. (Springer Berlin Heidelberg, 2012). doi:10.1007/978-3-642-28362-8

53. Zhong, X. *et al.* Superatomic Two-Dimensional Semiconductor. *Nano Lett.* **18,** 1483–1488 (2018).

54. Low, T. *et al.* Plasmons and screening in monolayer and multilayer black phosphorus. *Phys. Rev. Lett.* **113,** 106802 (2014).

55. Xia, F., Wang, H. & Jia, Y. Rediscovering black phosphorus as an anisotropic layered material for optoelectronics and electronics. *Nat. Commun.* **5,** 4458 (2014).

56. Wang, X., Jones, A., Seyler, K., Tran, V. & Jia, Y. Highly anisotropic and robust excitons in monolayer black phosphorus. *Nat. Nanotechnol.* **10,** (2015).

57. Liu, H. *et al.* Phosphorene: an unexplored 2D semiconductor with a high hole mobility. *ACS Nano* **8,** 4033–41 (2014).

58. Ma, W. *et al.* In-plane anisotropic and ultra-low-loss polaritons in a natural van der Waals crystal. *Nature* **562,** 557–562 (2018).

59. Bardeen, J. Tunnelling from a Many-Particle Point of View. *Phys. Rev. Lett.* **6,** 57–59 (1961).

60. Crommie, M. F., Lutz, C. P. & Eigler, D. M. Imaging standing waves in a two-dimensional electron gas. *Nature* **363,** 524–527 (1993).

61. Chen, W., Madhavan, V., Jamneala, T. & Crommie, M. F. Scanning tunneling microscopy observation of an electronic superlattice at the surface of clean gold. *Phys. Rev. Lett.* **80,** 1469–1472 (1998).

62. Feenstra, R. & Stroscio, J. Tunneling spectroscopy of the GaAs (110) surface. *Vac. Sci. Technol. B …* (1987).

63. Kitchen, D., Richardella, A., Tang, J. M., Flatté, M. E. & Yazdani, A. Atom-by-atom substitution of Mn in GaAs and visualization of their hole-mediated interactions. *Nature* **442,** 436–439 (2006).

64. Feenstra, R. M., Lee, J. Y., Kang, M. H., Meyer, G. & Rieder, K. H. Band gap of the Ge(111)-c2X8 surface by scanning tunneling spectroscopy. *Phys. Rev. B* **73,** 035310 (2006).

65. Gomes, K. K. *et al.* Visualizing pair formation on the atomic scale in the high-Tcsuperconductor Bi2Sr2CaCu2O8+δ. *Nature* **447,** 569–572 (2007).

66. T.-M. Chuang, M. P. Allan, Jinho Lee, Yang Xie, Ni Ni, S. L. Bud'ko, G. S. Boebinger, P. C. Canfield, J. C. D. Nematic Electronic Structure in the 'Parent' State of the Iron-Based Superconductor Ca(Fe1-xCox)2As2. *Science (80-.).* **181,** 181–185 (2011).

67. Hor, Y. S. *et al.* p-type Bi2Se3 for topological insulator and low-temperature thermoelectric applications. *Phys. Rev. B* **79,** 195208 (2009).

68. Seo, J. *et al.* Transmission of topological surface states through surface barriers. *Nature* **466,** 343–346 (2010).

69. Crommie, M. F., Lutz, C. P. & Eigler, D. M. Confinement of electrons to quantum corrals on a metal surface. *Science (80-.).* **262,** 218–220 (1993).

70. Moresco, F. Manipulation of large molecules by low-temperature STM: Model systems for molecular electronics. *Phys. Rep.* **399,** 175–225 (2004).

71. Swart, I., Sonnleitner, T., Niedenführ, J. & Repp, J. Controlled lateral manipulation of molecules on insulating films by STM. *Nano Lett.* **12,** 1070–1074 (2012).

72. Chen, C. J. Introduction to Scanning Tunneling Microscopy. (2008). doi:10.1002/jemt.1070280110

73. Tersoff, J. & Hamann, D. R. Theory and Application for the Scanning Tunneling Microscope. *Phys. Rev. Lett.* **50,** 1998–2001 (1983).

74. Giesen, K., Hage, F., Himpsel, F. J., Riess, H. J. & Steinmann, W. Two-photon photoemission via image-potential states. *Phys. Rev. Lett.* **55,** 300–303 (1985).

75. Laude, L. D. & Wautelet, M. Double-beam photoemission and the electronic structure of tellurium. *Nuovo Cim. B Ser. 11* **39,** 734–738 (1977).

76. Wautelet, M. & Laude, L. D. Laser-modulated photoemission in semiconductors. *Phys. Rev. Lett.* **38,** 40–43 (1977).

77. Knoesel, E., Hotzel, A., Hertel, T., Wolf, M. & Ertl, G. Dynamics of photoexcited electrons in metals studied with time-resolved two-photon photoemission. *Surf. Sci.* **368,** 76–81 (1996).

78. Bovensiepen, U. & Kirchmann, P. S. Elementary relaxation processes investigated by femtosecond photoelectron spectroscopy of two-dimensional materials. *Laser Photonics Rev.* **6,** 589–606 (2012).

79. Ichibayashi, T. & Tanimura, K. Ultrafast carrier relaxation in Si studied by time-resolved two-photon photoemission spectroscopy: Intravalley scattering and energy relaxation of hot electrons. *Phys. Rev. Lett.* **102,** 1–4 (2009).

80. Williams, K. W., Monahan, N. R., Koleske, D. D., Crawford, M. H. & Zhu, X. Y. Ultrafast and band-selective Auger recombination in InGaN quantum wells. *Appl. Phys. Lett.* **108,** (2016).

81. Williams, K. W., Monahan, N. R., Evans, T. J. S. & Zhu, X. Y. Direct Time-Domain View of Auger Recombination in a Semiconductor. *Phys. Rev. Lett.* **118,** 1–5 (2017).

82. F. Vallee and F. Bogani. Coherent time-resolved investigation of LO-phonon dynamics in GaAs. *Phys. Rev. B* **43,** (1991).

83. Chan, W. L. *et al.* Observing the multiexciton state in singlet fission and ensuing ultrafast multielectron transfer. *Science (80-.).* **334,** 1541–1545 (2011).

84. Bauer, M. Femtosecond ultraviolet photoelectron spectroscopy of ultra-fast surface processes. *J. Phys. D. Appl. Phys.* **38,** (2005).

85. Wallauer, R., Reimann, J., Armbrust, N., Güdde, J. & Höfer, U. Intervalley scattering in MoS2imaged by two-photon photoemission with a high-harmonic probe. *Appl. Phys. Lett.* **109,** (2016).

86. Zhang, Y. *et al.* Direct observation of the transition from indirect to direct bandgap in atomically thin epitaxial MoSe2. *Nat. Nanotechnol.* **9,** 111–115 (2014).

87. Kim, J. *et al.* Observation of tunable band gap and anisotropic Dirac semimetal state in black phosphorus. *Science (80-.).* **349,** 723–726 (2015).

88. Le Nagard, N., Perrin, A., Sergent, M. & Levy-Clement, C. PHOTOELECTROCHEMICAL PROPERTIES OF Re6Se8CI 2 A LAMELLAR TRANSITION METAL CLUSTER COMPOUND. *Mat. Res. Bull* **20,** 835–843 (1985).

89. Blanc, E., Schwarzenbach, D., Flack, H. D. & IUCr. The evaluation of transmission factors and their first derivatives with respect to crystal shape parameters. *J. Appl. Crystallogr.* **24,** 1035–1041 (1991).

90. Clark, R. C., Reid, J. S. & IUCr. The analytical calculation of absorption in multifaceted crystals. *Acta Crystallogr. Sect. A Found. Crystallogr.* **51,** 887–897 (1995).

91. Sheldrick, G. M. & IUCr. Crystal structure refinement with *SHELXL*. *Acta Crystallogr. Sect. C Struct. Chem.* **71,** 3–8 (2015).

92. Sheldrick, G. M. & IUCr. A short history of *SHELX*. *Acta Crystallogr. Sect. A Found. Crystallogr.* **64,** 112–122 (2008).

93. Dolomanov, O. V. *et al. OLEX2* : a complete structure solution, refinement and analysis program. *J. Appl. Crystallogr.* **42,** 339–341 (2009).

94. Fischer, C., Colell, H. & Tributsch, H. Surface structure of the semiconducting Re6Se8Cl2 cluster compound investigated by scanning tunneling microscopy. *Surf. Sci.* **280,** 2–7 (1993).

95. McLean, T. P. & Loudon, R. Exciton energy levels in germanium and silicon. *J. Phys. Chem. Solids* **13,** 1–9 (1960).

96. W.C. Dash, R. N. Intrinsic Optical Absorption in single-Crystal Ge and Si at 77 K and 300 K. *Phys. Rev.* **99,** (1955).

97. Tomlin, S. G. Optical reflection and transmission formulae for thin films. *J. Phys. D. Appl. Phys.* **1,** 312 (1968).

98. Smets, A., Jäger, K., Isabella, O., Van Swaaij, R. & Zeman, M. *Basic semiconductor physics*. *Solar Energy: The physics and engineering of photovoltaic conversion, technologies and systems* (2016).

99. Varshni, Y. P. Temperature Dependence of the Energy Gap in Semiconductors. *Physica* **34,** 149–154 (1967).

100. O'Donnell, K. P. & Chen, X. Temperature dependence of semiconductor band gaps. *Appl. Phys. Lett.* **58,** 2924–2926 (1991).

101. Hamby, D. W., Lucca, D. A., Klopfstein, M. J. & Cantwell, G. Temperature dependent exciton photoluminescence of bulk ZnO. *J. Appl. Phys.* **93,** 3214–3217 (2003).

102. Le Nagard, N., Perrin, A., Sergent, M. & Levy-Clement, C. Photoelectrochemical properties of Re6Se8Cl2 a lamellar transition metal cluster compound. *Mater. Res. Bull.* **20,** 835–843 (1985).

103. Perdew, J. P., Burke, K. & Ernzerhof, M. Generalized Gradient Approximation Made Simple. *Phys. Rev. Lett.* **77,** 3865–3868 (1996).

104. Heyd, J., Scuseria, G. E. & Ernzerhof, M. Hybrid functionals based on a screened Coulomb potential. *J. Chem. Phys.* **118,** 8207–8215 (2003).

105. Zeiger, H. J. *et al.* Theory for displacive excitation of coherent phonons. *Phys. Rev. B* **45,** 768–778 (1992).

106. Kuznetsov, A. V. & Stanton, C. J. Theory of coherent phonon oscillations in semiconductors. *Phys. Rev. Lett.* **73,** 3243–3246 (1994).

107. Zhu, D. *et al.* Coherent Phonon Rabi Oscillations with a High-Frequency Carbon Nanotube Phonon Cavity. *Nano Lett.* **17,** 915–921 (2017).

108. Gambetta, A. *et al.* Real-time observation of nonlinear coherent phonon dynamics in single-walled carbon nanotubes. *Nat. Phys.* **2,** 515–520 (2006).

109. Kazimierczuk, T., Fröhlich, D., Scheel, S., Stolz, H. & Bayer, M. Giant Rydberg excitons in the copper oxide Cu2O. *Nature* **514,** 343–347 (2014).

110. Greene, R. L., Bajaj, K. K. & Phelps, D. E. Energy levels of Wannier excitons in GaAs-Ga1-xAlxAs quantum-well structures. *Phys. Rev. B* **29,** 1807–1812 (1984).

111. Macfarlane, G. G., McLean, T. P., Quarrington, J. E. & Roberts, V. Exciton and phonon effects in the absorption spectra of germanium and silicon. *J. Phys. Chem. Solids* **8,** 388–392 (1959).

112. Qiu, H. *et al.* Hopping transport through defect-induced localized states in molybdenum disulphide. *Nat. Commun.* **4,** 1–6 (2013).

113. Wei, Y. *et al.* The nature of strength enhancement and weakening by pentagong-heptagon defects in graphene. *Nat. Mater.* **11,** 759–763 (2012).

114. Červenka, J., Katsnelson, M. I. & Flipse, C. F. J. Room-temperature ferromagnetism in graphite driven by two-dimensional networks of pointdefects. *Nat. Phys.* **5,** 840–844 (2009).

115. KC, S., Longo, R. C., Addou, R., Wallace, R. M. & Cho, K. Impact of intrinsic atomic defects on the electronic structure of MoS_2 monolayers. *Nanotechnology* **25,** 375703 (2014).

116. Zhou, W. *et al.* Intrinsic structural defects in monolayer molybdenum disulfide. *Nano Lett.* **13,** 2615–2622 (2013).

117. Vancsó, P. *et al.* The intrinsic defect structure of exfoliated MoS2single layers revealed by Scanning Tunneling Microscopy. *Sci. Rep.* **6,** 29726 (2016).

118. Heyd, J., Scuseria, G. E. & Ernzerhof, M. Hybrid functionals based on a screened Coulomb potential. *J. Chem. Phys.* **118,** 8207–8215 (2003).

119. Zhang, C. *et al.* Visualizing band offsets and edge states in bilayer–monolayer transition metal dichalcogenides lateral heterojunction. *Nat. Commun.* **7,** 10349 (2016).

120. Kerelsky, A. *et al.* Absence of a Band Gap at the Interface of a Metal and Highly Doped Monolayer MoS 2. *Nano Lett.* **17,** 5962–5968 (2017).

121. Zhang, C., Johnson, A., Hsu, C.-L., Li, L.-J. & Shih, C.-K. Direct Imaging of Band Profile in Single Layer MoS 2 on Graphite: Quasiparticle Energy Gap, Metallic Edge States, and Edge Band Bending. *Nano Lett.* **14,** 2443–2447 (2014).

122. Liang, L. *et al.* Electronic bandgap and edge reconstruction in phosphorene materials. *Nano Lett.* **14,** 6400–6406 (2014).

123. Hafeez, M., Gan, L., Bhatti, A. S. & Zhai, T. Rhenium dichalcogenides (ReX 2, X= S or Se): an emerging class of TMDs family. *Mater. Chem. Front.* **1,** 1917–1932 (2017).

124. Wildervanck, J. C. & Jellinek, F. The dichalcogenides of technetium and rhenium. *J. Less Common Met.* **24,** 73–81 (1971).

125. Wolverson, D., Crampin, S., Kazemi, A. S., Ilie, A. & Bending, S. J. Raman spectra of monolayer, few-layer, and bulk ReSe2: An anisotropic layered semiconductor. *ACS Nano* **8,** 11154–11164 (2014).

126. Perrin, A. & Perrin, C. Low-dimensional frameworks in solid state chemistry of Mo6 and Re6 cluster chalcohalides. *Eur. J. Inorg. Chem.* 3848–3856 (2011). doi:10.1002/ejic.201100400

127. Chevrel, R. & Sergent, M. From three-dimensional to one-dimensional cluster Mo6 chalcogenides. *Cryst. Chem. Prop. Mater. with Quasi-One-Dimensional Struct.* 315–373 (1986).

128. Fedorov, V., Mishchenko, A. & Fedin, V. Cluster Transition Metal Chalcogenide Halides. *Russ. Chem. Rev.* **54,** 408–423 (1985).

129. Koknat, F. W., Adaway, T. J., Erzerum, S. I. & Syed, S. Convenient synthesis of the hexanuclear molybdenum(II) halides Mo6Cl12 and Mo6Br12·2H2O. *inorg. nucl. chem. lett.* **16,** 307–310 (1980).

130. Perrin, C. & Sergent, M. Condensation des motifs (Mo6L14) dans la chimie des clusters octaédriques Mo6. *J. Less-Common Met.* **123,** 117–133 (1986).

131. Hong, M. *et al.* Identifying the Non-Identical Outermost Selenium Atoms and Invariable Band Gaps across the Grain Boundary of Anisotropic Rhenium Diselenide. *ACS Nano* **12,** 10095–10103 (2018).

132. Kiraly, B., Hauptmann, N., Rudenko, A. N., Katsnelson, M. I. & Khajetoorians, A. A. Probing Single Vacancies in Black Phosphorus at the Atomic Level. *Nano Lett.* **17,** 3607–3612 (2017).

133. Zhang, S. *et al.* Spotting the differences in two-dimensional materials – the Raman scattering perspective. *Chem. Soc. Rev.* **47,** 3217–3240 (2018).

134. Ferrari, A. C. Raman spectroscopy of graphene and graphite: Disorder, electron-phonon coupling, doping and nonadiabatic effects. *Solid State Commun.* **143,** 47–57 (2007).

135. Ferrari, A. C. *et al.* Raman spectrum of graphene and graphene layers. *Phys. Rev. Lett.* **97,** 1–4 (2006).

136. Li, H. *et al.* From Bulk to Monolayer MoS2 : Evolution of Raman Scattering. *Adv. Funct. Mater.* **22,** 1385–1390 (2012).

137. Wang, T. *et al.* Identifying the Crystalline Orientation of Black Phosphorus by Using Optothermal Raman Spectroscopy. *ChemPhysChem* **18,** 2828–2834 (2017).

138. You, Y. *et al.* Edge chirality determination of graphene by Raman spectroscopy Edge chirality determination of graphene by Raman spectroscopy. *Appl. Phys. Lett.* **93,** 163112 (2008).

139. Wang, Y., Cong, C., Qiu, C. & Yu, T. Raman Spectroscopy Study of Lattice Vibration and Crystallographic Orientation of Monolayer MoS2 under Uniaxial Strain. *Small* **9,** 2857–2861 (2013).

140. Kroumova, E. *et al.* Bilbao Crystallographic Server : Useful Databases and Tools for Phase-Transition Studies. *Phase Transitions* **76,** 155–170 (2003).

141. Ribeiro, H. B. *et al.* Unusual angular dependence of the Raman response in black phosphorus. *ACS Nano* **9,** 4270–4276 (2015).

142. Li, L. *et al.* Strong In-Plane Anisotropies of Optical and Electrical Response in Layered Dimetal Chalcogenide. *ACS Nano* **11,** 10264–10272 (2017).

143. Li, M. *et al.* Revealing anisotropy and thickness dependence of Raman spectra for SnS flakes. *RSC Adv.* **7,** 48759–48765 (2017).

144. Barone, V., Hod, O. & Scuseria, G. E. Electronic structure and stability of semiconducting graphene nanoribbons. *Nano Lett.* **6,** 2748–2754 (2006).

145. Son, Y. W., Cohen, M. L. & Louie, S. G. Half-metallic graphene nanoribbons. *Nature* **444,** 347–349 (2006).

146. Son, Y. W., Cohen, M. L. & Louie, S. G. Energy gaps in graphene nanoribbons. *Phys. Rev. Lett.* **97,** 1–4 (2006).

147. Zhang, L., Dai, H., Lee, S., Wang, X. & Li, X. Chemically Derived, Ultrasmooth Graphene Nanoribbon Semiconductors. *Science (80-.).* **319,** 1229–1232 (2008).

148. Jiao, L., Zhang, L., Wang, X., Diankov, G. & Dai, H. Narrow graphene nanoribbons from carbon nanotubes. *Nature* **458,** 877–880 (2009).

149. Narita, A., Feng, X., Hernandez, Y., Jensen, S. & Bonn, M. Synthesis of structurally well-defined and liquid-phase-processable graphene nanoribbons. *Nat. Chem.* **6,** 126–132 (2014).

150. Cai, J. *et al.* Atomically precise bottom-up fabrication of graphene nanoribbons. *Nature* **466,** 470–473 (2010).

151. Li, G., Yoon, K. Y., Zhong, X., Zhu, X. & Dong, G. Efficient Bottom-Up Preparation of Graphene Nanoribbons by Mild Suzuki-Miyaura Polymerization of Simple Triaryl Monomers. *Chem. - A Eur. J.* **22,** 9116–9120 (2016).

152. Li, G. *et al.* A modular synthetic approach for band-gap engineering of armchair graphene nanoribbons. *Nat. Commun.* **9,** 1–9 (2018).

Appendix

A. Self-assembly of two-dimensional islands of graphene nanoribbons

The discovery of graphene [3] has ignited intense studies on low-dimensional materials which exhibit novel physical phenomena and potential applications in electronics and optoelectronics, as mentioned in Chapter 1. Particularly, graphene nanoribbons (GNRs) — narrow stripes of graphene with functional edges, are considered as promising building blocks of new electronic devices since they possess non-zero bandgaps due to quantum confinement and edge effects [144–146]. Bandgaps are highly tunable by varying the width of GNRs and edge structures (e.g. armchair and zigzag). Moreover, the edges of GNRs can be chemically modified by linking to functional groups, which offers great benefits to the design of devices with desired properties.

Two main approaches have been used to produce GNRs: "top-down" exfoliation [147,148] and "bottom-up" synthesis [149,150]. The latter has great advantages of fabricating GNRs with atomically precise structures and widths that are smaller than 10 nm. Here, we present several types of armchair graphene nanoribbons (aGNRs) synthesized via solution-mediated cyclodehydrogenation. The initial N=9 armchair graphene nanoribbon (**G1**) was synthesized via a mild Suzuki–Miyaura polymerization of simple triaryl monomers (2,3-bisarylated 4-bromophenylboric acid ester **M1**), followed by cyclodehydrogenation, as demonstrated in Figure A1. The produced aGNR **G1** has a center symmetric structure with the same alkyl chains R^1 = -

$C_{10}H_{21}$ on both sides of the core chain. This method can be expanded to fabricate width-modulated armchair graphene nanoribbon heterostructures by fusing monomers consisted of two different molecular building blocks. Three kinds of N = 6 graphene nanoribbons (**G2**-**G4**) with unsymmetrical edges have been synthesized by using benzothiadiazole, benzotriazole and benzene as building blocks, respectively. The molecular structures are displayed in Figure A3c, A4b and A5b, respectively. Such structures lead to unsymmetrical electronic distributions on GNRs, which offers great potential for the fabrication of donor–acceptor conjugate GNRs and band gap

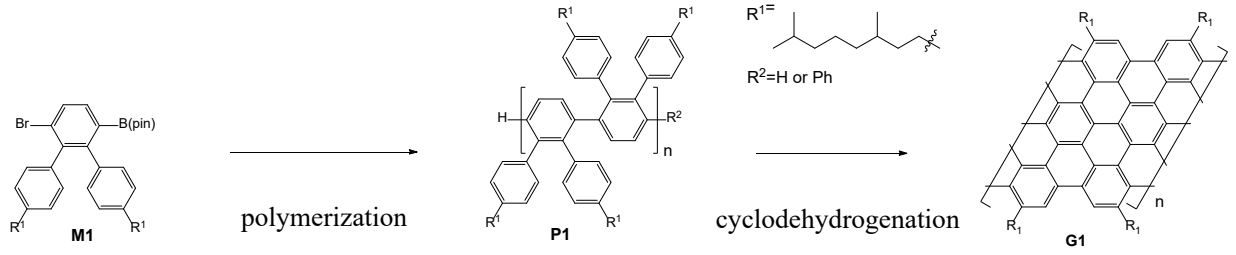

Figure A.1 Schematic of synthesizing G1 from monomer **M1** via polymerization and cyclodehydrogenation.

engineering. To better characterize those GNRs and fabricate them into devices, it is essentially important to improve the patterning methods and understand the arrangements of GNRs on a substrate. Details of the work were published in reference [151,152]

A.1 Thin film preparations

There are three key factors that affect the quality of the patterned films: dispersion of GNRs in the solvent, patterning methods and the substrate. Solubility of GNRs depends on the solvent (polar or nonpolar) and the side chains of GNRs (organic groups and length). To increase the solubility of the GNR powder and avoid the aggregations in the solution, we dissolved approximately 0.6 mg of GNR in 10 ml of toluene, followed by heat and sonication cycles. The suspension was then

diluted and filtered by a 0.45 μm filter. It looks transparent due to the low concentration. Various deposition methods including drop-casting, spin-coating and atomization have been used to prepare thin films of GNRs. Atomization provides the best results since it distributes a small amount of solution uniformly on large areas of the substrate, which reduces the aggregations of GNRs. By heating the substrate at 50 ℃ while spraying, solvent evaporates rapidly after deposition. In addition to the reduction of interactions between GNRs, increasing the coupling between the sample and the substrate is an effective way to improve the film quality. Compared to SiO_2/Si and mica substrates, the honeycomb structure of highly oriented pyrolytic graphite (HOPG) gives strong π-stacking interactions with the main chain of GNRs. Thus, we chose HOPG as the substrate and sprayed GNRs suspension on a freshly cleaved surface of HOPG using an atomizer.

A.2 AFM characterization of N = 9 aGNR

Detailed information on the nanostructure of GNRs was characterized by AFM in the ambient conditions. Figure A2a shows a AFM image of GNR **G1** deposited on HOPG. The GNR molecules self-assemble into 2D islands consisting of highly ordered stripes along all three possible orientations, indicated by the six-fold symmetry in the Fourier transform (FFT) of the image. Each 2D island is characterized by a height of 0.40 ± 0.05 nm and an inter-stripe separation of 4.8 ± 0.2 nm, as demonstrated by a typical line profile across the boundary (Figure A2b) and FFT of the image (Figure2a, inset). The height of each island agrees well with the interlayer distance in graphite (0.34 nm) and the stripe separation is close to the expected intermolecular spacing between parallel GNR molecules adopting a flat-lying geometry, as depicted by the molecular model in Figure A2c. Similar self-assembled 2D-striped structures have also been observed in other types of GNRs. Tapping mode AFM was used to confirm that these 2D islands are not the

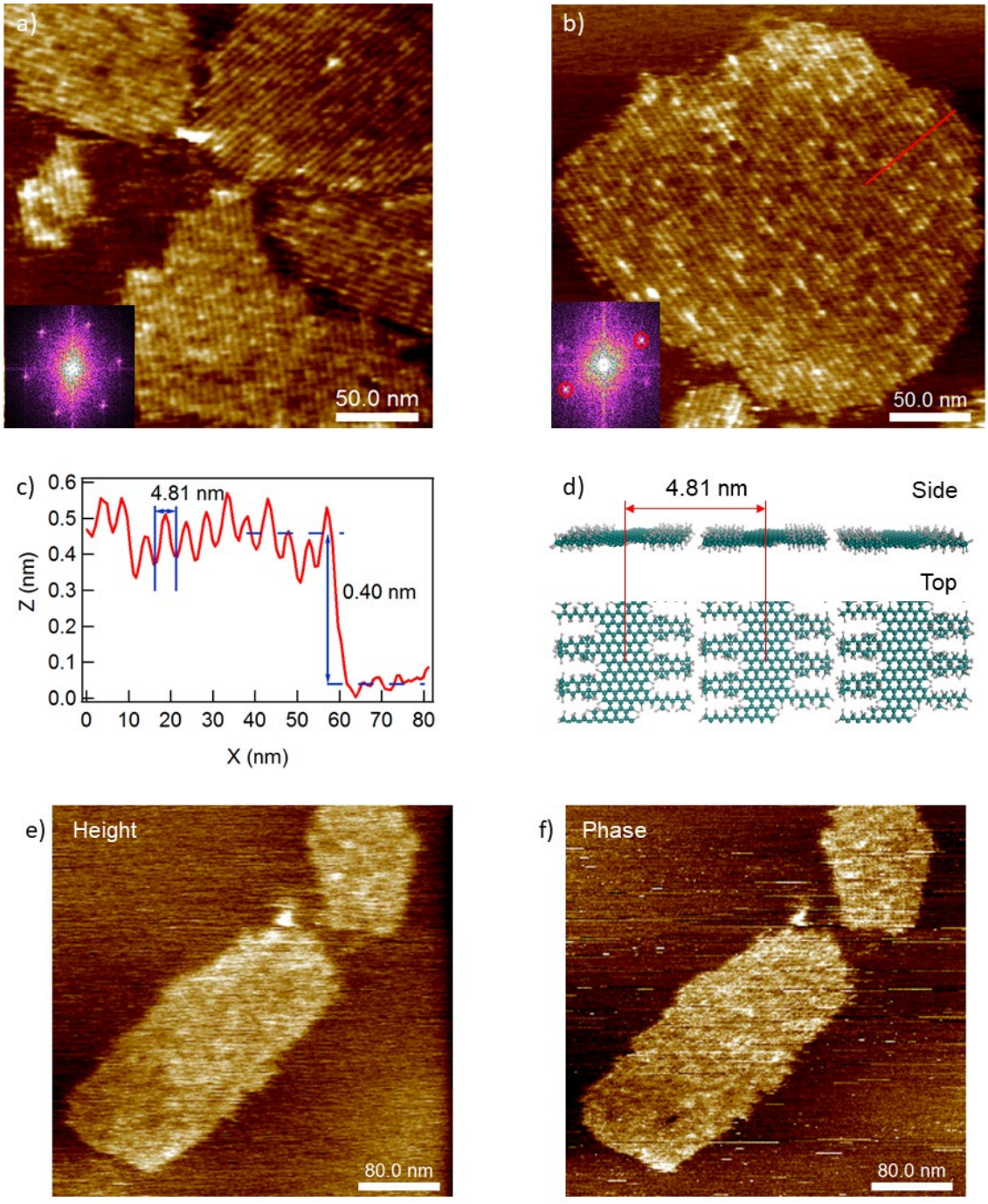

Figure A.2 AFM characterization of G1 on HOPG a) AFM image including all three possible orientations on the substrate with the same periodicity. Inset is the FFT image of a). b) AFM image of **G1** on HOPG, image size: 270 X 270 nm. c) Height profile along the red line in b). d) Molecular model of **G1**. Green, carbon; grey, hydrogen. e) AFM height image of aGNR **G1** on HOPG, image size: 400 × 400 nm. f) AFM phase image on the same area as e), showing the contrast between GNR terraces and the substrate.

features of HOPG itself, as shown in Figure A2e and f. The phase image clearly displays the contrast between terraces and the substrate.

A.3 AFM characterization of N = 6 aGNRs

The structures of these N = 6 aGNRs were obtained by AFM in the ambient condition. Figure A3a shows an AFM image of aGNR **G2** deposited on HOPG. Graphene nanoribbons self-assembled into small 2D domains consisting of highly ordered stripes. The average periodicity of these stripes is 4.8 ± 0.4 nm, as shown by a line profile (Figure A3d) across the domain in the zoom-in AFM image (Figure A3b). The inter-stripe distance is approximately twice the width of **G2**, indicating the formation of a head-to-head, tail-to-tail sub-structure as depicted in Figure A3e. Formation of

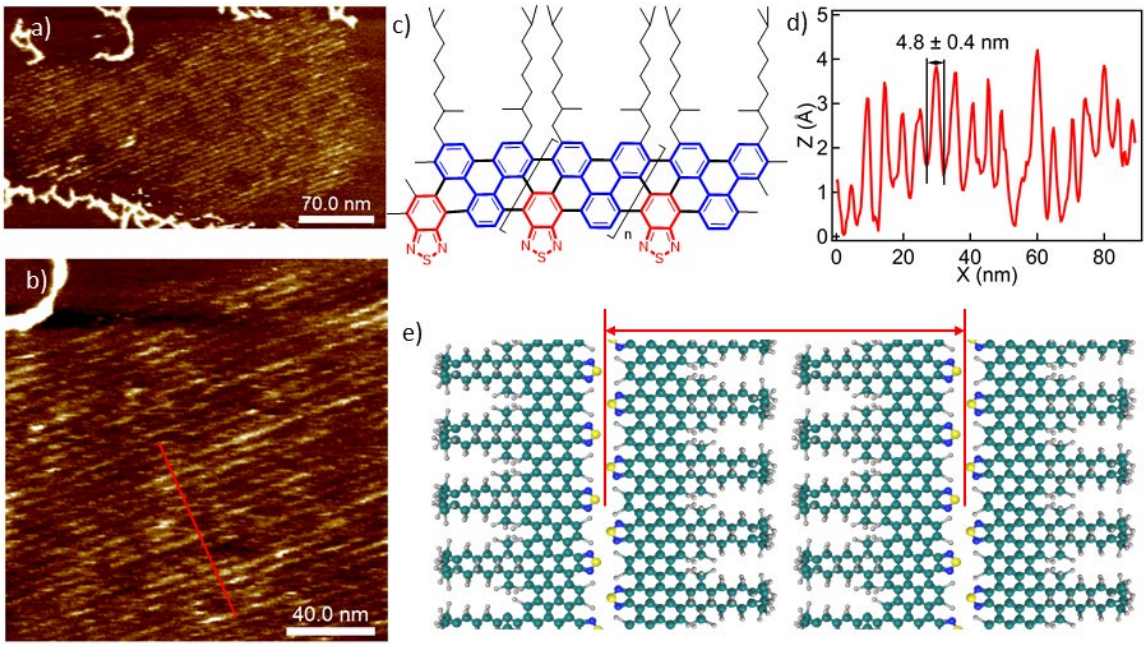

Figure A.3 AFM characterization of G2 on HOPG. a) AFM image of **G2** on HOPG, image size :361 x 210 nm. b) Zoom-in image of a), image size :175 x 175 nm. c) Molecular structure of N = 6 aGNR **G2** with highlighted **M1** (blue) and benzothiadiazole (red) molecular building blocks. d) A representative line profile of the image (red line in panel b) with periodicity of 4.8 ± 0.4 nm. e) Molecular model of **G2**. Green, Carbon; blue, Nitrogen; yellow, Sulfur; grey, Hydrogen.

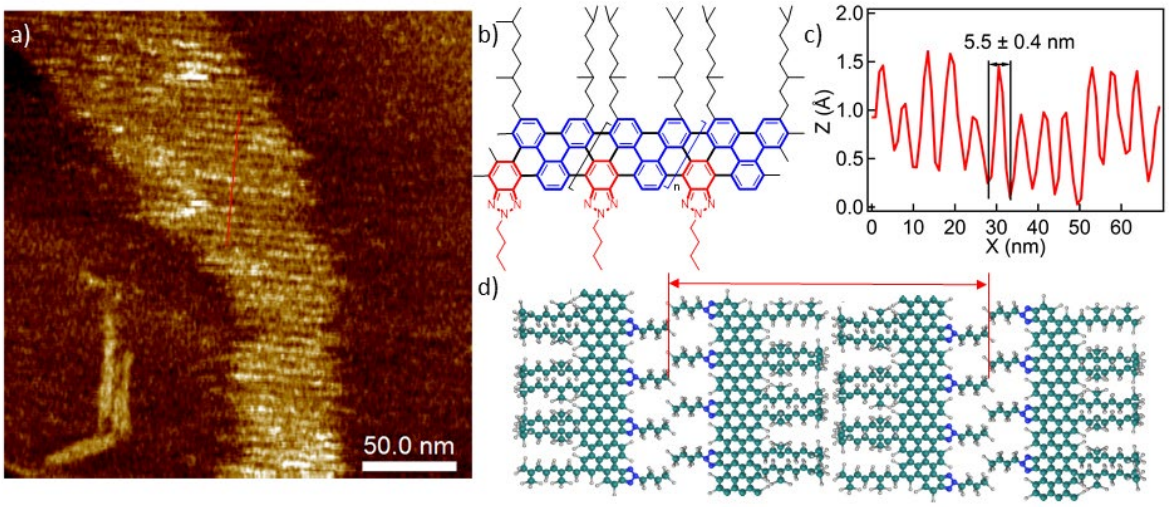

Figure A.4 AFM characterization of G3 on HOPG a) AFM image of **G3** on HOPG, image size: 270 X 270 nm. b) Molecular structure of N = 6 aGNR **G3** with highlighted **M1** (blue) and benzotriazole (red) molecular building blocks. c) Height profile along the red line in a). d) Molecular model of **G3** in a flat-lying geometry. Carbon, green; nitrogen, yellow; hydrogen, grey.

such a dimeric sub-structure is reasonable, as the aliphatic chains are only located on one side of the ribbon. Moreover, AFM images show that aGNRs line up along the same stripe, therefore the apparent length of each stripe can extend to a few hundred nanometers. To estimate the lengths of these aGNRs, we measured the lengths of individual GNRs with distinct ends. The statistical results obtained from AFM images are 34 ± 14 nm (averaged over 111 replicates) for **G2**.

Similarly, aGNR **G3** forms highly ordered stripes with the average periodicity of 5.5 ± 0.4 nm on HOPG as shown in Fig. A4a and c. The slightly larger average periodicity of **G3** is presumably due to the butyl side-chains on the benzotriazole moieties. **G3** arranges in the same head-to-head, tail-to-tail sub-structure on HOPG, as shown in Figure A4d. The statistical result of the lengths of **G3** obtained from AFM images is 48 ± 11 nm (averaged over 69 replicates).

Contrast to **G2** and **G3**, aGNR **G4** forms islands with random shapes with a height of ~ 0.9 nm, suggesting strong aggregations of the ribbons on HOPG (Figure A5). Such aggregation on the

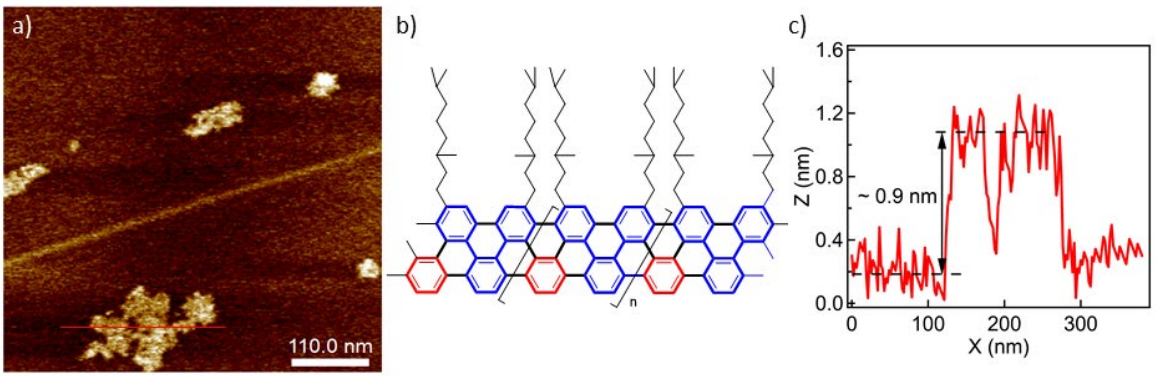

Figure A.5 AFM characterization of G4 on HOPG a) An AFM height image of G4 aggregating on HOPG. b) Molecular structural of N = 6 aGNR G4 with M1 (blue) and benzene (red) molecular building blocks. c) Height profile along the red line in a).

substrate makes it difficult to obtain detailed structural information of **G4**. In order to reduce undesired aggregations and increase solubility of **G4**, a short polymer precursor with much bulkier side chains (nonyltetradecyl groups) was employed to prepare a new aGNR **G4'** in the same configuration as G4, shown in Figure A6b. An AFM image of aGNR G4' on HOPG shown in

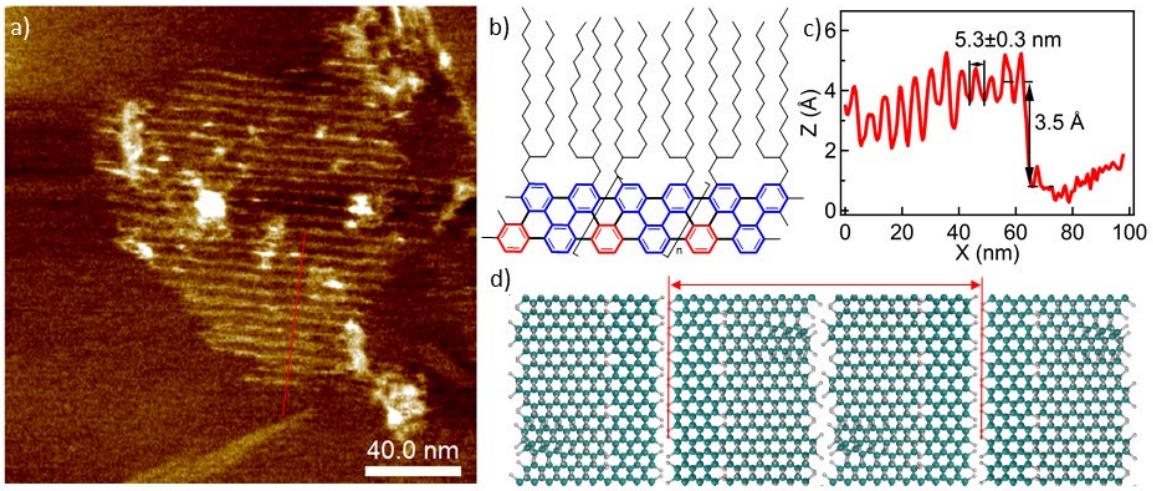

Figure A.6 AFM characterization of G4' on HOPG. a) AFM image of **G4'** on HOPG, image size: 200 X 200 nm. b) Molecular structure of N = 6 aGNR **G4'** with highlighted **M1** (blue) and benzotriazole (red) molecular building blocks. c) Height profile along the red line in a). d) Molecular model of **G4'** in a flat-lying geometry. Carbon, green; hydrogen, grey.

Figure A6a displays a similar structure with striped domains. A line profile across the boundary shows a height of 0.35 nm and an inter-stripe separation of 5.3 $\pm$ 0.3 nm, suggesting a similar head-to-head, tail-to-tail pattern as **G2** and **G3**.

B. Lists of publications

[1] **Zhong, X**., Lee, K., Choi, B., Meggiolaro, D., Liu, F., Nuckolls, C., ... & Zhu, X. (2018). Superatomic Two-Dimensional Semiconductor. *Nano letters*, *18*(2), 1483-1488.

[2] **Zhong, X.**, Lee, K., Meggiolaro, D., Dismukes, A., Choi, B., Wang, F., Nuckolls, C., ... & Zhu, X. (2018) $Mo_6S_3Br_6$: An Anisotropic Two-Dimensional Superatomic Semiconductors. *Advanced Materials*, submitted.

[3] Li, G., Yoon, K. Y., **Zhong, X.**, Wang, J., Zhang, R., Guest, J. R., ... & Dong, G. (2018). A modular synthetic approach for band-gap engineering of armchair graphene nanoribbons. *Nature communications*, *9*.

[4] Li, G., Yoon, K. Y., **Zhong, X.**, Zhu, X., & Dong, G. (2016). Efficient Bottom-Up Preparation of Graphene Nanoribbons by Mild Suzuki–Miyaura Polymerization of Simple Triaryl Monomers. *Chemistry–A European Journal*, *22*(27), 9116-9120.

[5] Evans, T. J., Schlaus, A., Fu, Y., **Zhong, X.**, Atallah, T. L., Spencer, M. S., ... & Zhu, X. Y. (2018). Continuous-Wave Lasing in Cesium Lead Bromide Perovskite Nanowires. *Advanced Optical Materials*, *6*(2), 1700982.

[6] Lee, K., Choi, B., Plante, I. J. L., Paley, M. V., **Zhong, X.**, Crowther, A. C., ... & Roy, X. (2018). Two-Dimensional Fullerene Assembly from an Exfoliated van der Waals Template. *Angewandte Chemie International Edition*, *57*(21), 6125-6129.

[7] Sisto, T. J., Zhong, Y., Zhang, B., Trinh, M. T., Miyata, K., **Zhong, X.**, ... & Nuckolls, C. (2017). Long, atomically precise donor–acceptor cove-edge nanoribbons as electron acceptors. *Journal of the American Chemical Society*, *139*(16), 5648-5651.